QUANTUM COMPUTATION AND QUANTUM SIMULATION WITH ATOMIC AND SOLID STATE SYSTEM

by

Zhexuan Gong

A dissertation submitted in partial fulfillment
of the requirements for the degree of
Doctor of Philosophy
(Physics)
in the University of Michigan
2013

Doctoral Committee:

Professor Luming Duan, Chair
Professor Duncan G. Steel
Professor Georg A. Raithel
Assistant Professor Hui Deng
Assistant Professor Kai Sun

© Zhexuan Gong 2013

Dedicated to my parents

Cuihua Yang and Xiantao Gong

ACKNOWLEDGMENT

First of all, I'd like to deeply thank my advisor, Professor Luming Duan, for mentoring me through my last five years for graduate research. While I already heard about Luming's great talent and groundbreaking contributions to the field of quantum information as an undergraduate in China, I was still amazed by his broad knowledge and sharp insight in physics after I attended his classes in the first year I came to University of Michigan. Joining his group is one of the best choices I made in my life, as I later found that Luming also has a fantastic personality to work with. He is always super kind and patient in discussion, and almost every time I go to him with some difficulties in research, he has the "magic" to help me out in one way or another. To me, Luming is a unique theorist in physics, as he's also a "half an experimentalist". His ideas and ways of thinking, is filled with beauty of theory, but at the same time, fully meaningful to latest experimental world. And that is, as his *Tao* of theoretical research, what I appreciated and learned from him most during all these years.

I also want to say thanks to my undergraduate advisor in Huazhong University of Science and Technology, Professor Ying Wu, for luring me to the miraculous world of quantum physics from start . He also conveyed to me, in his own ways, the perception of excitement in research, which has continued to inspire me over time.

It is also a great pleasure for me to work with other members in my group. I still

remember the interesting weekly discussions with Zhang-qi Yin on attempting to unravel the “mystery” of nuclear spin fluctuation in quantum dot system. And last year, Zhangqi helped me joining the fantastic project on time crystal, which I’m truly grateful for. Guindar Lin helped me a lot in getting into trapped-ion research and generously shared with me his nice code on gate optimization. Yanghao Chan has always been very helpful for answering all my “stupid” questions on numerical simulation and cold atoms, and I enjoyed many times figuring out weird “discrepancy” with Chao Shen in random research projects. In the last two years, I had much fun sharing office with Dong-ling Deng, who has taught me a plethora of things about foundations of quantum mechanics, topological quantum computing and various “intimidating” mathematics. I’m also thankful to my other former and current group members: Jason Kestner, Wei Zhang, Bin Wang, Yongjian Han, Zhaohui Wei, Jiangmin Zhang, Yue Wu, Zhen Zhang, and Shengtao Wang.

Besides, I’m grateful to all my collaborators in my past research. Prof. Duncan Steel and his graduate students here have provided me precious knowledge on quantum dot experiment. Prof. Chris Monroe at University of Maryland has shared with me his great expertise on trapped ion, and I always find exhilarating to chat with him. I’ve learned so much on trapped ion experiments from his students and his outstanding former postdoc, Kihwan Kim, now a professor at Tsinghua University. I’d also like to express my gratitude to my collaborators in Prof. Misha Lukin’s group at Harvard University, especially Norman Yao, who also became my good friend, for vastly expanding my knowledge on NV centers.

Finally, I’m thoroughly indebted to my parents, especially my mom, for her persistent encouragement and support all these years. I cannot express my thanks in words. This thesis is dedicated to you.

TABLE OF CONTENTS

List of Figures

LIST OF APPENDICES

ABSTRACT

The ability to manipulate individual quantum systems in a precise way has led to a new era of quantum technologies, including quantum computation and quantum simulation. In this thesis we present several new implementations of these quantum technologies.

We first aim at addressing current experimental challenges for quantum dot based quantum computing. We propose a systematic way to study the dynamics of nuclear spin, which is responsible for the short electron spin coherence time. Our calculation is based on diffusion model and is consistent with experiments. We also invent a novel protocol to realize high-fidelity ultrafast universal quantum gate in recently-developed quantum dot molecule system. Experimental realization of our protocol requires only a simple time engineering of optical pulses.

We then propose a new quantum state transfer scheme for Nitrogen-Vacancy center based quantum computer, which is applicable at room temperature. Our method accomplishes high fidelity robust quantum state transfer through uncontrolled thermal nitrogen spin chain between two remote NV registers.

Our next study helps building a hybrid quantum computer by entangling disparate systems using photonic links. The photons emitted from two types of system need to be matched in both frequency and pulse shape. We propose a simple method to match the emitted pulse shape from two qubit systems with different transition linewidths.

We then focus on quantum simulation with trapped ions. We show the possibility of observing a novel type of temperature driven structural phase transition in trapped ion chain, which originates from anharmonic interaction between different vibrational modes. Afterward, an experimental protocol to simulate a conceptually new state of matter, called time crystal, is proposed based on ions trapped in a ring trap.

Finally, we propose two new applications based on the recently developed trapped ion quantum simulator of spin models: (1) simulation of Haldane-Shastry model, which opens the way of experimental study to a remarkable theoretical model involving spin liquid ground state and fractional excitations (2) observation of prethermalization and dynamical phase transition, which are poorly understood non-equilibrium phenomena in closed quantum many-body system.

Chapter 1

Introduction

1.1 Background and Motivation

Developed at the beginning of the twentieth century, the theory of quantum mechanics has been one of the most successful theories for its precise predictions of the microscopic world. The world quantum mechanics portrays is fundamentally probabilistic, drastically different from classical mechanics that deterministically describes the motion of macroscopic objects in everyday life. The quantum nature renders the possibility of a single object in two states at the same time (superposition), and even of two objects far apart being instantaneously connected (entanglement). In the past twenty years, physicists have made tremendous progress at harnessing these unusual quantum effects to achieve a variety of new quantum technologies, such as quantum computers with extraordinary computing power, quantum communication with unbreakable security, quantum metrology aiming for obtaining the highest measurement precision allowed by nature, and quantum simulators that can assist us in understanding some very complicated quantum many-body system.

The realization of these fascinating new quantum technologies, however, can be very challenging. A large-scale controllable quantum system that can be used to build a quantum computer or quantum simulator is still far from reality. One key reason is that the quantum properties of a large system will quickly die off when the system interacts with its surrounding environment. Such a phenomenon is called decoherence, a bane that plagues almost every form of quantum technology. Another difficulty is that technologies like quantum computation and quantum simulation require different parts of the quantum system to interact strongly with each other. This schizophrenic requirement of having a quantum system that is both strongly coupled within itself and well isolated from the environment is the fundamental challenge in quantum technology. Motivated by this challenge, researchers have been actively investigating a variety of physical systems, ranging from cold atoms and ions, to artificial atoms in solid state materials, in hopes of finding an "ideal" system. However, up to now, each of these systems has their own advantages as well as disadvantages, lacking a clear "winner".

While a perfect candidate is still missing, we are far from exhausting the power of our existing quantum systems. The main motivation of this thesis is hence to maximize the benefit of our quantum technology with available experimental technique. Dedicated to this goal, we have looked into three important and complementary approaches: (1) Finding novel ways to ameliorate disadvantages within one quantum system. (2) Combining the power of different types of systems to make a more powerful "hybrid system". (3) Discovering certain problems of physical importance that employ the unique strength of a specific quantum system but circumvent its shortcomings.

Before we outline how far we've gone into these three approaches in Section 1.4, we'd like to give some brief introduction to the background and history of two most important

quantum technologies: quantum computation and quantum simulation, in the following Section 1.2 and 1.3.

1.2 Quantum Computation

Here we present a brief review on quantum computation, and readers can find more detailed reviews in Ref. [1–6]:

The idea of quantum computation was originated in the late 1980s. Pioneers such as R. Feynman and D. Deutsch first realized the fundamental connection between the laws of physics and computation [7, 8], as the storing, transmitting and processing of information always require physical means. It was then natural to find that at microscopic level, where quantum effects become important, the classical theory of computation will be inadequate. Particularly, phenomena such as quantum superposition and quantum entanglement may be utilized for computations. If the quantum version of the computer is allowed to accept an input state that is comprised of a coherent superposition of many individual classical input states, the unitary evolution of such an input state, according to quantum mechanics, will yield a coherent superposition of all corresponding output states, thus creating a massive parallelism of computation. This quantum parallelism is the salient feature of any quantum computer, as it may provide a significant speed up over its classical counterpart.

However, finding a quantum algorithm that fully exploits the power of quantum parallelism is a quite difficult task, as the measurement of the output quantum state, if it's in a coherent superposition, will only give the observer one possible outcome among the huge number of parallel components. Although some rather artificial problems can be solved with a quantum computer in an extremely efficient manner [9], the real-world application

of a quantum computer remains obscured, until in 1994, Peter Shor invented the groundbreaking quantum algorithm for factorizing large numbers [10]. The importance of Shor's factoring algorithm lies in two aspects: (1) Most of the popular public key ciphers are based on the difficulty of factoring larger integers, including the ubiqitous RSA protocol and its variants. (2) Shor's algorithm provides a way to factor large integers in polynomial scale of time on a quantum computer, which is an exponential speed up over any known classical algorithm. Consequently, the power of Shor's algorithm would allow a very modestly sized quantum computer (with, for example, a hundred quantum bits) to outperform even the largest classical supercomputer in the world, hence becoming one of the foremost motivations for developing a quantum computer.

While there is still an ongoing effort to discover new quantum algorithms with impressive speed-ups [11–13], a large portion of the quantum computation community is devoted to the physical implementation, *i.e.*, to build a real-world quantum computer. The requirements for building a quantum computer have also been formally characterized by D. DiVincenzo, which are known as "DiVincenzo criteria" [14]. In short, there are five basic criteria: (1) Well-defined qubits (2) Initialization to a pure state (3) Universal set of quantum gates (4) Qubit-specific measurement (5) Long coherence times.

Over the years, researchers are finding different physical systems that meet the above five criteria well. Outstanding candidates include trapped ions [15–17], neutral atoms [18, 19], superconducting circuits [20, 21], quantum dots [22], photons [23], and NV centers in diamond [24]. This thesis only involves research related to three of these systems, quantum dots, NV centers, and trapped ions. We'll discuss how they perform in the task of quantum computation case by case in the following chapters.

1.3 Quantum Simulation

The idea of quantum simulation was also first proposed by Richard Feynman [7]. Feynman was interested in simulating one quantum system with another because he became aware of the complexity of simulating quantum systems using classical computers. For a large quantum many-body system, even if one has the correct model with an explicitly defined Hamiltonian, calculating its equilibrium or dynamical properties would involve tackling a Hilbert space that scales exponentially with the number of particles. Even for the simplest spin-1/2 system, the most powerful classical computer nowadays will fail at predicting more than roughly 50 spins. Feynman's proposal circumvents such computational problems by resorting to another quantum system that is effectively described by the same model. In addition, this "simulator" system is assumed to be well controlled at our disposal. For example, we have the ability of tuning the interactions between particles within the system, and can perform measurements on physical quantities at different positions and time. As a result, we will have a much better knowledge of the original quantum system we'd like to learn indirectly, without the need of simulation on classical computer.

Feynman also conjectured that a quantum computer would most likely be an efficient quantum simulator at the same time, and indeed, as later proven by Seth Lloyd [25], any quantum Hamiltonian with few-body interactions can be simulated by a quantum computer with a polynomial cost of time, through breaking the evolution of Hamiltonian into a series of quantum gates.

While we still have to wait for a fully fledged quantum computer, the main motivation of quantum simulation, at the current stage, is to construct devices based on available experimental techniques, that can perform helpful simulation of some poorly-understood quantum many-body systems, including frustrated magnetic materials, high-Tc supercon-

ductors, matter with topological orders etc. The reason why this goal is likely to be achievable is because a lot of times, we do not need the knowledge of the complete many-body wavefunction provided by a powerful quantum computer. Instead, certain physical observables, such as particle densities, magnetization, or spin correlations, suffice to tell us key properties of a quantum system (e.g. its phase diagram). In addition, quantum simulation is generally expected to be more robust to errors than quantum computation [26], as macroscopic physical quantities are likely to be insensitive to local noise or perturbations.

These characteristics of quantum simulation lead researchers to build quantum simulators with specific purposes for different systems. For example, the trapped ion system is especially useful at simulating small sized quantum spin models [27, 28]; cold neutral atoms trapped in an optical lattice have proven to be powerful simulators of the Bose-Hubbard model [29, 30], and photonic system has the potential of simulating certain quantum chemistry problems [31, 32]. But the wealth of problems amenable for quantum simulation, even within the reach of current experimental technology, is still far from exhausted. We'll discuss about several new applications of existing quantum simulators in this thesis as well.

1.4 Outline of the thesis

The first half of the thesis is dedicated to quantum computation. As we stated before, the first approach to enhance our quantum technology is to counter existing problems in specific quantum systems. In Chapter 2, we present our work closely related to the fight against decoherence in quantum dot (QD) system [33]. The work is based on the recently-developed way of enhancing qubit coherence time in QD via dynamical preparation of

nuclear spin state [34–38]. We provide a detailed analysis of the dynamics of prepared nuclear spin state, which is found to be consistent with experiments.

Chapter 3 continues the discussion in QD system, but now centered on the control of qubits rather than the environment. We propose an experimentally feasible protocol to achieve complete two-qubit control in vertically stacked double quantum dot system [39, 40], where universal quantum control has yet to be demonstrated due to limited control in experiment. To maximize gate fidelity, we introduce the optimal pulse engineering protocol, which can also be a very useful technique for other systems, such as trapped ions [41, 42].

In Chapter 4, we present a novel protocol for implementing high fidelity quantum state transfer in Nitrogen-Vacancy center based quantum registers [43, 44]. Such a protocol is robust to many error sources, and most importantly, allows for a room temperature experimental setup, which is a huge advantage in reality.

Chapter 5 is related to the second approach we discussed in Section 1.1, the creation of a hybrid quantum system. Specifically, we are aware that to transfer quantum information within a hybrid quantum system, an efficient photonic channel used for heralding entanglement is usually mandatory [17, 45]. However, different types of matter qubit not only have different transition frequencies, but may also have distinct transition linewidths. Our work here solves the latter problem by using an engineered pulse to match the pulse shape of photons emitted from two subsystems in a hybrid quantum structure.

The second half of the thesis aims for quantum simulation, where we have followed the third approach that employs the unique strength of a specific system, here the trapped ions, for investigating and simulating physically important problems. In Chapter 6, we present a practical scheme to study a new type of temperature-driven structural phase

transition using the motional degrees of freedom in trapped ions [46]. In Chapter 7, we propose the first possible realization of a conceptually brand-new state of matter, called time crystal [47–50], that allows spontaneous time translational symmetry breaking in the ground state.

The last two chapters are new applications of the trapped ion simulator on spin models, which has been a research focus in recent years [27, 51–53]. In Chapter 8, we use a generalized version of an existing simulator to simulate the Haldane-Shastry model, a fascinating exactly solvable theoretical model in condensed matter physics that unfortunately, does not exist in any real-world materials. This model has the paradigmatic spin liquid state as its ground state, which can be readily tested by our proposed trapped-ion simulator. In Chapter 9, we show how one can observe and study some remarkable but poorly-understood non-equilibrium phenomena in closed quantum many-body problem, such as prethermalization and dynamical phase transitions, based on the currently available version of the trapped-ion spin model quantum simulator.

Chapter 2

Dynamics of nuclear spins in a quantum dot

2.1 Introduction

Electron spins in quantum dot consist of one of the most promising systems for realization of quantum computation [54]. The spin state of a single electron in a quantum dot can be coherently controlled either optically through fast laser pulses or electronically through tuning of gate voltages [54–57]. In experiments, the coherence time of the electron spin is largely limited by its hyperfine coupling to the nuclear spin environment in the host semiconductor material. The coupling causes spectral diffusion and gives a typical spin decoherence time $T_2^* \sim 15ns$ for the electron spin qubit [22, 58]. This coherence time could be significantly prolonged with application of spin echo [59] or other dynamic decoupling techniques [60–63]. However, implementation of these techniques requires repeated applications of many laser pulses. Each pulse inevitably induces some noise by itself, which limits the practical performance of suppressing spin noise under real environments.

Another technique to increase the coherence time for the electron spin is through the

dynamic nuclear-spin polarization (DNP) [34, 36–38, 64–70], which prepares the nuclear spin environment into certain configurations. The nuclear spins in such configurations collectively generate an effective magnetic field (the Overhauser field) on the electron spin with small fluctuation, hence reducing the spectral diffusion of the electron spin. Although nuclear spins can be polarized through many methods such as optical pumping [64], substantial reduction in the fluctuation of the Overhauser field requires almost complete polarization of the nuclear spins [71], which is hard to achieve experimentally. The recent experiments, including both optically and electronically controlled quantum dot systems [34,36–38], however, demonstrate surprising feedback mechanisms which can lock the Overhauser field to certain values without significant polarization of the nuclear spins. The Overhauser field generated from such locking mechanism has much smaller fluctuation, which effectively increases the coherence time T_2^* of the electron spin qubit by up to two orders of magnitudes.

The DNP process prepares a fixed Overhauser field with small fluctuation that enables us to do gate experiments on the electron spins over a longer coherence time. Important questions under this background are how long this fixed Overhauser field can survive after the DNP process and what factors determine/influence the relaxation time of the Overhauser field. Recent experiments have observed that the Overhauser field has a typical relaxation time ranging from a few seconds to a few minutes, and even up to an hour in certain system [72]. The variation of this relaxation time is believed to be a result of diverse experimental configurations, such as different applied magnetic field [36, 69], electron spin state in double quantum dots [36], and DNP pump time [70].

In this chapter, we develop a quantitative theory to calculate the relaxation time of the Overhauser field in the environment of quantum dots, and provide a qualitative ex-

planation to the dependence of Overhauser field relaxation time on various experimental configurations mentioned above. The relaxation of the Overhauser field is widely believed to be caused by nuclear spin diffusion. In bulk material, nuclear spin diffusion has been well studied [73] and it is caused simply by the nuclear dipole-dipole interaction. In a quantum dot, however, the presence of the electron spin generates two new effects in the diffusion process. First, the electron spin can mediate the diffusion of nuclear spins through a virtual hyperfine process. Second, the effective magnetic field generated by the polarized electron spin produces an inhomogeneous Knight shift on the surrounding nuclear spins, and this Knight shift can suppress the nuclear spin diffusion. The influence of the nuclear spin diffusion coefficient by the Knight shift has been taken into account in Ref. [74], but electron mediated nuclear spin diffusion was ignored there. Without considering electron mediated diffusion, one cannot explain the dependence of Overhauser field relaxation time on various experimental parameters such as magnetic field. A more recent work [75] considers relaxation of the Overhauser field due to the electron mediated nuclear spin diffusion, but not including the direct nuclear dipole-dipole interaction. Such treatment ends up with a conclusion that the Overhauser field can only decay by less than 1%, contradictory to experimental facts of complete decay of Overhauser field over long time. A quantitative theory that includes a complete description of both effects is, to our knowledge, still missing. In this work, we take into account both electron mediated nuclear spin diffusion and direct nuclear dipole-dipole diffusion, and the results are consistent with recent experimental observations in Refs. [36, 69, 70].

This chapter is arranged as follows: in Section 2.2 we give a formalism to describe relaxation of the Overhauser field that includes contributions from the nuclear dipole-dipole interaction, the electron mediated nuclear spin diffusion, and the Knight shift. Then we

derive the effective nuclear spin diffusion equation and solve it numerically to determine the relaxation time of the Overhauser field. In Section 2.3 we compare our calculation results with the recent experiments and show that they are in qualitative or semi-quantitative agreement. We summarize our results in Section 2.4 with brief discussions.

2.2 Formalism

We assume that an external magnetic field B_0 much larger than the mean value and variance of the local Overhauser field generated by nuclei is applied along the z-direction (perpendicular to the quantum dot layer). In this case, we can drop the nonsecular terms in the interaction Hamiltonian. For simplification, we consider only one species of nuclei around the quantum dot electron. The total Hamiltonian for the electron and nuclear spin system, including both the Fermi contact hyperfine interaction and nuclear dipole-dipole interaction, can be written as:

$$
\begin{aligned}
H &= H_e + H_n + H_{en} + H_{nn}, && (2.2.1)\\
H_e &= -g_e \mu_B B_0 S^z, && (2.2.2)\\
H_n &= -g_n \mu_N B_0 \sum_i I_i^z, && (2.2.3)\\
H_{en} &= \sum_i A_i S^z I_i^z + \sum_i \frac{A_i}{2}(S^+ I_i^- + S^- I_i^+), && (2.2.4)\\
H_{nn} &= \sum_{i \neq j} 2B_{ij} I_i^z I_j^z - \sum_{i \neq j} B_{ij} I_i^+ I_j^-, && (2.2.5)\\
B_{ij} &= \frac{\mu_0}{4\pi}(g_n \mu_N)^2 R_{ij}^{-3}(1 - 3\cos^2\theta_{ij}), && (2.2.6)
\end{aligned}
$$

where A_i denotes the hyperfine coupling between the electron and nuclear spin at site i with spatial coordinates (x_i, y_i, z_i). R_{ij} is the distance between two nuclei at site i, j. θ_{ij} is the angle between the line connecting sites i, j and the z direction.

We note that for B_0 ranging from a few mT to a few T, the electron's Zeeman splitting is on the order of $10^{-1} - 10^2$GHz, while the average hyperfine coupling in most quantum dot systems is on the order of MHz. Thus we can adiabatically eliminate the spin-flip terms in the hyperfine interaction Hamiltonian and correspondingly modify the other terms in the Hamiltonian as [75]:

$$
\begin{aligned}
H_e &= -(g_e\mu_B B_0 + \frac{\sum_i A_i^2}{4g_e\mu_B B_0})S^z, && (2.2.7)\\
H_n &= \sum_i [-g_n\mu_N B_0 + A_i(1 - \frac{A_i}{4g_e\mu_B B_0})S^z]I_i^z, && (2.2.8)\\
H_{nn} &= \sum_{i\neq j} 2B_{ij} I_i^z I_j^z - \sum_{i\neq j}(B_{ij} + \frac{A_i A_j S^z}{2g_e\mu_B B_0})I_i^+ I_j^-, && (2.2.9)
\end{aligned}
$$

where we have introduced an electron-mediated nuclear flip-flop term in H_{nn}. Since we are interested in the long time dynamics of nuclear spins, we can completely eliminate the electron from the Hamiltonian by replacing the constant operator S^z with its expectation value. We find that using $S^z = 1/2$ or $S^z = -1/2$ will yield almost the same result in the following calculations. Therefore we can set $S^z = 1/2$ for simplicity and arrive at the following effective Hamiltonian (neglecting constant terms):

$$
\begin{aligned}
H &= H_0 + H_1, && (2.2.10)\\
H_0 &\approx \sum_i (-g_n\mu_N B_0 + A_i/2)I_i^z + \sum_{i\neq j} 2B_{ij} I_i^z I_j^z, && (2.2.11)\\
H_1 &= -\sum_{i\neq j}(B_{ij} + \frac{A_i A_j}{4g_e\mu_B B_0})I_i^+ I_j^-. && (2.2.12)
\end{aligned}
$$

Here, the term proportional to A_i in H_0 is the Knight shift term. For this Knight shift, we have neglected the small term proportional to A_i^2 in Eq. (2.2.8) as it is dominated by the A_i term in most experimental systems.

The expectation value for the z component of nuclear spin at site k will evolve according to the Schrodinger equation:

$$\frac{\partial \langle I_k^z \rangle}{\partial t} = \frac{i}{\hbar} Tr\{\rho(t)[H_1, I_k^z]\}, \tag{2.2.13}$$

where $\rho(t)$ is the nuclear spin density matrix at time t, which can be calculated by switching to the interaction picture:

$$\tilde{\rho}(t) = \rho(0) + \frac{i}{\hbar} \int_0^t [\tilde{\rho}(t'), \tilde{H}_1(t')] dt', \tag{2.2.14}$$

with $\tilde{H}_1(t) = exp(iH_0 t/\hbar) H_1 exp(-iH_0 t/\hbar)$. Further calculation yields [73]:

$$\frac{\partial \langle I_k^z \rangle}{\partial t} = \frac{i}{\hbar} Tr\{\rho(0)[\tilde{H}_1(t), I_k^z]\} \tag{2.2.15}$$

$$+ \quad \left(\frac{i}{\hbar}\right)^2 \int_0^t Tr\{\rho(t-t')[H_1, [\tilde{H}_1(t'), I_k^z]]\} dt' \tag{2.2.16}$$

We assume the nuclear spin (with spin-I) density matrix as a product state of the following form:

$$\rho(t) = \bigotimes_k \rho_k(t) \quad \rho_k(t) = \frac{1}{2I+1} + \frac{\langle I_k^z(t) \rangle}{Tr\{(I_k^z)^2\}} I_k^z. \tag{2.2.17}$$

Such an approximation is valid when off-diagonal terms of the density matrix are negligible. This is justified by the fact that fluctuations in B_0 and inhomogeneous Knight shift will quickly destroy correlation and transverse coherence between the nuclear spins [75, 76].

Besides, calculating without this approximation will not change the physical nature of the result, as the authors of Ref. [73] have shown that off-diagonal terms only have a minor contribution to the diffusion coefficients.

By using the explicit form of the Hamiltonian [Eq. (2.2.10-2.2.12)] and density matrix [Eq. (2.2.17)], we can reduce Eq. (2.2.15) to:

$$\begin{aligned} \frac{\partial \langle I_k^z \rangle}{\partial t} &= \sum_{i \neq k} W_{ik} (\langle I_i^z(t) \rangle - \langle I_k^z(t) \rangle) \qquad (2.2.18) \\ W_{ki} &= \frac{1}{Tr\{(I_k^z)^2\}} \int_0^t Tr\{[\tilde{H}_1(t), I_k^z][\tilde{H}_1(t-t'), I_i^z]\} dt' \end{aligned}$$

where W_{ki} has a clear physical meaning as the flip-flop rate between nuclear spins at site i and k.

For a 2D InAs/GaAs quantum dot, we take As nuclei ($I = 3/2$) as an example for further calculation. The parameter W_{ki} can be analytically calculated when approximating the integration upper limit in the above expression for W_{ki} from t to infinity [74].

$$\begin{aligned} W_{ik} &= \frac{17\sqrt{2\pi}}{5} C_{ik}^2 (A_{ik}^2 + g_{ik})^{-1/2} \\ &+ \frac{12\sqrt{2\pi}}{5} C_{ik}^2 (A_{ik}^2 + 64 C_{ik}^2 + g_{ik})^{-1/2} \\ &+ \frac{9\sqrt{2\pi}}{10} C_{ik}^2 (A_{ik}^2 + 256 C_{ik}^2 + g_{ik})^{-1/2}, \qquad (2.2.19) \\ A_{ik} &= A_i - A_k, \qquad (2.2.20) \\ C_{ik} &= B_{ik} + \frac{A_i A_k}{4 g_e \mu_B B_0}, \qquad (2.2.21) \\ g_{ik} &= 80 \sum_{j \neq i,k} (C_{ij} - C_{kj})^2. \qquad (2.2.22) \end{aligned}$$

The hyperfine coupling rate A_i is proportional to the square of the electron wave func-

tion in a quantum dot. And in the following calculation we assume the dot potential is like a square well in the z-direction and the electron wave function takes a Gaussian shape in the x, y-plane. The hyperfine coupling rate A_i can then be written as $A_i = A_0 \cos^2(\pi z_i/z_0) \exp[-(x_i^2 + y_i^2)/l_0^2]$, where (x_i, y_i, z_i) are spatial coordinate of the site i. l_0 and z_0 are, respectively, the Fock-Darwin radius and thickness of the quantum dot, and A_0 is the hyperfine coupling for the nuclear spin at the origin (electron's location).

The assumption that the nuclear spins follow a diffusion process requires the flip-flop rate for two distant sites to be negligible. This requirement is satisfied by the fact that the coefficient C_{ik} decays to zero fast as R_{ik} increases ($B_{ik} \propto R_{ik}^{-3}$ and $A_i A_k \leq A_0 \exp[-(R_i^2 + R_k^2)/l_0^2) \leq A_0 \exp(-R_{ik}^2/l_0^2)$ where we ignore the diffusion in z direction as discussed below). If we treat $\langle I_k^z(t)\rangle$ as a continuous function of spatial variable x^α ($\alpha = x, y, z$). We can then carry out a Taylor expansion of $\langle I^z(t)\rangle$ for site i around site k:

$$\begin{aligned} \langle I_i^z(t)\rangle &\approx \langle I_k^z(t)\rangle + \frac{\partial \langle I_k^z(t)\rangle}{\partial x^\alpha}(x_k^\alpha - x_i^\alpha) \\ &+ \frac{1}{2}\frac{\partial^2 \langle I_k^z(t)\rangle}{\partial x^\alpha \partial x^\beta}(x_k^\alpha - x_i^\alpha)(x_k^\beta - x_i^\beta) + \cdots \end{aligned} \tag{2.2.23}$$

where Einstein's summation convention is implied for spatial index α, β. Substituting this into Eq. (2.2.18) and noting that the summation of the first order derivative term over all sites vanishes due to the lattice symmetry [1], we have:

$$\frac{\partial \langle I_k^z\rangle}{\partial t} \approx \sum_{i \approx k} [\frac{1}{2} W_{ik}(x_k^\alpha - x_i^\alpha)(x_k^\beta - x_i^\beta)] \frac{\partial^2 \langle I_k^z(t)\rangle}{\partial x^\alpha \partial x^\beta} \tag{2.2.24}$$

The $\sum_{i \approx k}$ notation above means summation over the sites near k. Define coefficient $D^{\alpha\beta} =$

[1] The hyperfine coupling rate A_i, although inhomogeneous over a larger scale, only changes slightly from one nuclear spin to its nearby spins, so in summation over the nearby lattice sites, we still have an approximate lattice symmetry for the jump rate W_{ik}.

$\sum_{i\approx k} W_{ik}(x_k^\alpha - x_i^\alpha)(x_k^\beta - x_i^\beta)/2$ and similarly note that for $\alpha \neq \beta$ the summation over all sites vanishes, we have:

$$\frac{\partial \langle I_k^z \rangle}{\partial t} = (D^{xx}\frac{\partial^2}{\partial x^2} + D^{yy}\frac{\partial^2}{\partial y^2} + D^{zz}\frac{\partial^2}{\partial z^2})\langle I_k^z(t)\rangle \tag{2.2.25}$$

Eq. (2.2.25) is a 3D anisotropic diffusion equation with spatially varying diffusion coefficients (as A_{ik}, B_{ik}, W_{ik} all depend on the spatial coordinates), which is not easy to solve. To further simplify it, we note that to obtain the major feature for the full time dynamics of the Overhauser field $\langle h_z(t)\rangle = \sum_k A_k \langle I_k^z(t)\rangle$, it is reasonable to first ignore the diffusion in the z direction, because the quantum dot layer is usually a few nm thick and chemical or structural mismatch in adjacent layers can strongly suppress diffusion in the z direction [69]. In addition, from symmetry in the 2D $x-y$ plane, we expect to have $D^{xx} \approx D^{yy}$ and can thus define an average 2D diffusion coefficient $D(x,y) = \sum_{i\approx k} W_{ik}[(x_k - x_i)^2 + (y_k - y_i)^2]/4$. Now we have a simplified 2D diffusion equation:

$$\frac{\partial \langle I_k^z \rangle}{\partial t} = D(x,y)(\frac{\partial^2}{\partial x^2} + \frac{\partial^2}{\partial y^2})\langle I_k^z(t)\rangle. \tag{2.2.26}$$

The above partial differential equation can be effective solved using finite element method by coarse graining a large number of nuclear spin sites to a small number of mesh nodes. But before solving Eq. (2.2.26), we would like to have some discussion about the diffusion coefficient $D(x,y)$. For $x, y \gg l_0$, the role of electron can be neglected and a numerical calculation of the above diffusion coefficient gives a uniform background value $D \approx 7\ nm^2/s$, consistent with the previous theoretical and experimental reports of diffusion coefficient in bulk material [73, 74]. In our calculation, we set the quantum dot parameters $l_0 = 30\ nm$, $z_0 = 10\ nm$, $A_0 = 1\ \mu eV \approx 1.5\ MHz$, $\sum_k A_k \approx 80\ \mu eV$, the

lattice constant $a_0 = 0.563\ nm$, and the number of nuclei $N \approx 9 \times 10^5$, according to typical experimental values [36, 68, 69].

Within the range of Fock-Darwin radius l_0, the presence of the quantum dot electron will change the diffusion coefficient through two competing mechanisms: on the one hand, the confined electron generates an inhomogeneous Knight shift [58], which lifts the degeneracy of the nuclear Zeeman energy for different nuclei and prevents the spin flip-flop; on the other hand, electron mediated nuclear spin flip-flop enhances the nuclear spin diffusion, and the enhancement decreases from the center to the edge of the dot.

Our numerical simulation shows that whether one mechanism dominates the other is largely determined by the external magnetic field B_0. Fig. 2.2.1-2.2.2 show the diffusion coefficient $D(x, y)$ under $B_0 = 0.2T$ and $B_0 = 2T$. We can see that under a small magnetic field, the electron mediated flip-flop greatly enhances the nuclear spin diffusion near the center of the dot, causing a sharp peak in $D(x, y)$). In a large magnetic field, however, such enhancement is negligible compared to the Knight shift, which suppresses the nuclear spin diffusion, yielding a wide dip in $D(x, y)$). The dependence on the strength of magnetic field can be easily explained from the effective Hamiltonian [Eq. (2.2.10-2.2.12)]: the electron mediated flip-flop term is inversely proportional to B_0 while the Knight shift term is independent of B_0. We note that the reason why we have a narrower peak than the dip is due to the fact that the Knight shift term is proportional to the hyperfine coupling rate (Gaussian distribution in x-y plane) while the electron mediated flip-flop term is proportional to the product of two nucleus's hyperfine coupling rates. We also note that the 2D diffusion coefficient $D(x, y)$ in Fig. 2.2.1-2.2.2 does not have azimuthal symmetry since in our calculation we assume the nuclear spins are in a square lattice with no azimuthal symmetry.

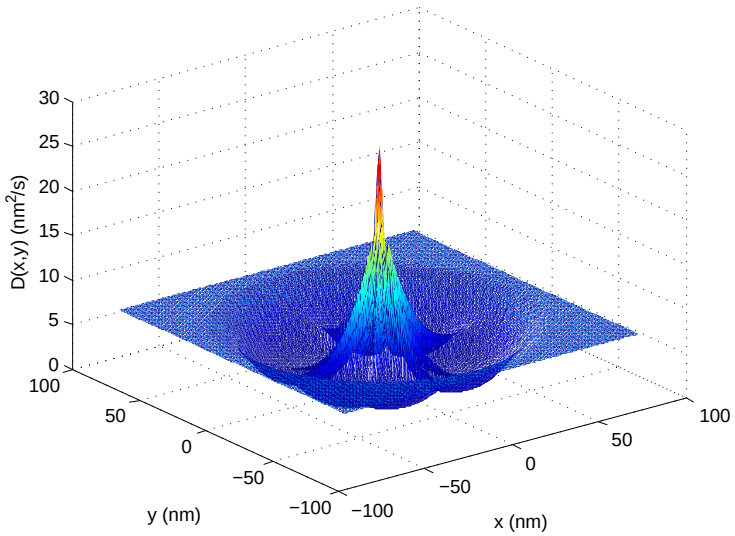

Figure 2.2.1: Diffusion coefficient D(x,y) under $B_0 = 0.2T$. The narrow high peak at the center of the dot is due to electron-mediated nuclear spin flip-flop, and the wide dip is due to inhomogeneous Knight shift.

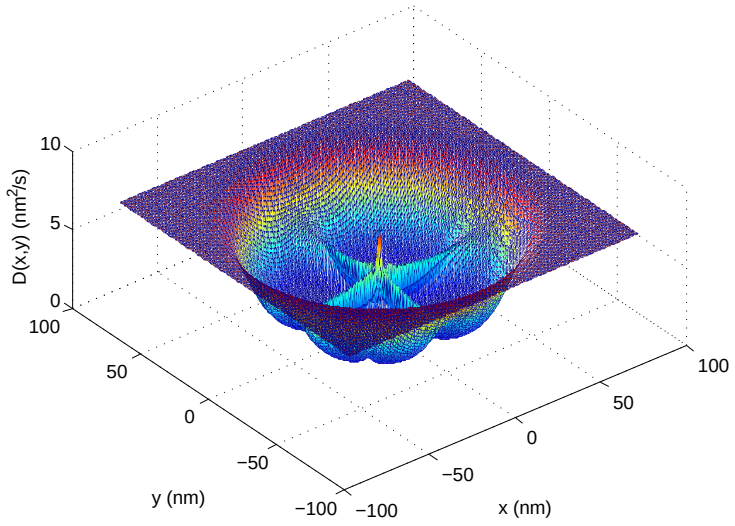

Figure 2.2.2: Diffusion coefficient D(x,y) under $B_0 = 2T$. The inhomogeneous Knight shift dominates in this case, so diffusion is generally suppressed within the Fock-Darwin radius.

2.3 Comparison with experiments

To compare with experiments, we numerically solve the diffusion equation [Eq. (2.2.26)] under certain initial and boundary conditions. For the initial condition, since the nuclear spins are partially polarized through the DNP process from the hyperfine interaction with the electron spin [34, 36–38], it is reasonable to expect that right after the DNP process, the polarization distribution $\langle I_k^z \rangle$ is proportional to the hyperfine interaction rate. So in the following calculation, we assume $\langle I_k^z \rangle \propto A_k \propto \exp[-(x_i^2 + y_i^2)/l_0^2]$ at $t = 0$ for solving the diffusion equation [Eq. (2.2.26)]. For the boundary condition, we can assume naturally that $\langle I_k^z \rangle$ approaches zero when the radius goes to infinity. However, in numerical calculation, we have to take a finite radius. To make the spin diffusion possible, this finite radius has to be significantly larger than the radius of the size l_0 of the initial electron wave packet. In the calculation, we take a radius of about $300\ nm$ (10 times of l_0) so that the number of total nuclear spins inside is about 100 times the number of initially partially polarized nuclear spins within the electron's wave packet. With such choice, we expect the cutoff error to be at a percent level.

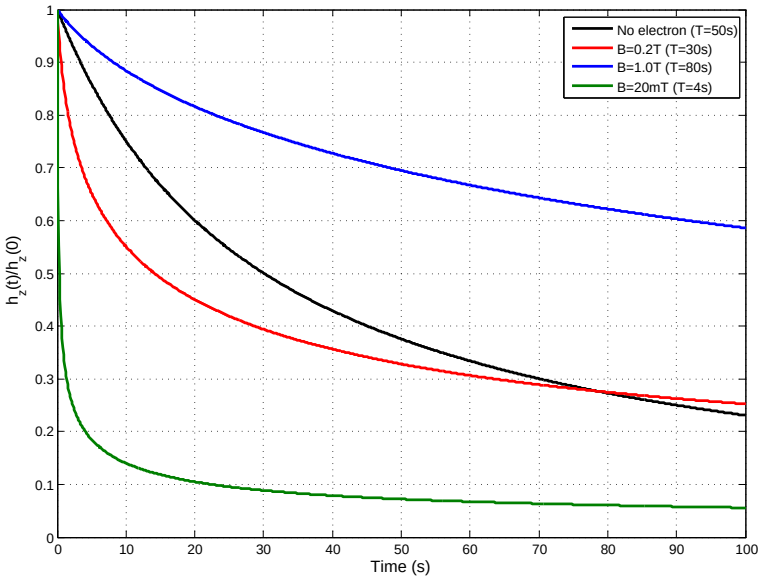

Figure 2.3.1: Decay of the Overhauser field under various small magnetic fields. The solid line refers to the case with electron staying in the (2,0) singlet state where electron plays no role in nuclear spin diffusion.

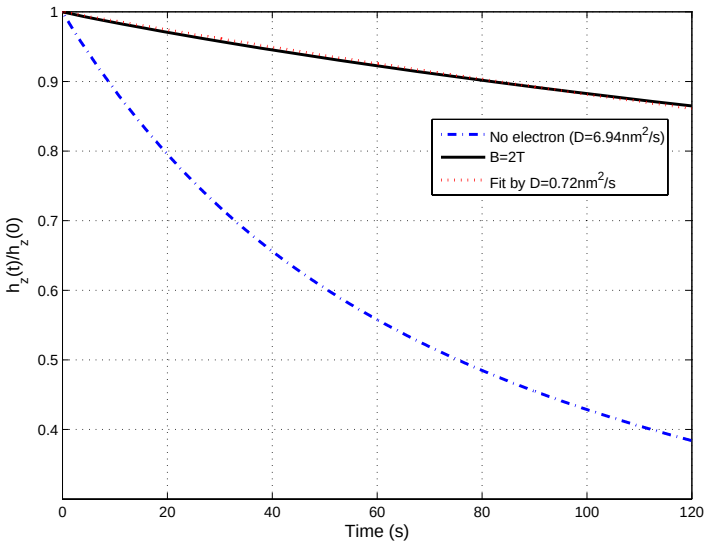

Figure 2.3.2: Decay of the Overhauser field under a strong magnetic field. The solid line shows the dynamics of the Overhauser field under $B = 2T$ and the dotted line is a fit by using a constant diffusion coefficient.

First, to compare with the experiments in Ref. [36], we calculate the relaxation of the Overhauser field $h^z(t) = \sum_k A_k \langle I_k^z(t) \rangle$ under different electron states and different values of the external magnetic field B_0, and show the results in Fig. 2.3.1. We note that for the double quantum dot system in Ref. [36], if the electron stays in the (2,0) singlet state, the electron spin has $S_z \equiv 0$, therefore it basically has no influence on the nuclear spin diffusion. In this case, the nuclear spin diffusion is merely governed by intrinsic nuclear dipole-dipole interaction. However, for the electron in the (1,1) state, with the magnetic field in the range of tens of mT as in this experiment, the electron mediated spin diffusion dominates the Knight shift and it accelerates the nuclear spin relaxation. This is why one can see two effects from Fig. 2.3.1: (1) electrons in the (1,1) state will speed up the decay of the Overhauser field compared to electrons in the (2,0) state; (2) a smaller magnetic field gives a faster decay of the Overhauser field. Both of these effects agree well with the experimental observations in Ref. [36]. The decay time is also consistent in terms of the order of magnitude.

With a much larger magnetic field (say, $B_0 = 2T$, as in experiments in Ref. [69]), the electron mediated nuclear spin diffusion is suppressed, and the Knight shift plays a more important role. The Knight shift suppresses the nuclear spin diffusion, yielding a relaxation time of Overhauser field significantly larger than that in bulk material. Fig. 2.3.2 shows the decay of Overhauser field in this case, and we can fit the curve with an effective constant diffusion coefficient at about $D_{eff} \approx 0.7 nm^2/s$. Compared with the diffusion coefficient in the bulk material ($D \approx 7 nm^2/s$), a suppression factor of 10 is obtained through applying a strong magnetic field. Experiments done in Ref. [69] measured an effective diffusion coefficient 50 times smaller than the value in the bulk system. Other suppression effect of nuclear spin diffusion involved in Ref. [69] comes from inhomogeneous quadru-

ple shift of nuclear spin energy [72, 77]. Similar to the inhomogeneous Knight shift, the inhomogeneous quadruple shift can also make nuclear spin flip-flop process off-resonant and therefore suppressed. And the quadruple shift in those InGaAs quantum dot systems can have much stronger influence to the energy spectrum of the nuclear Hamiltonian than the Knight shift. Therefore intense suppression of nuclear spin diffusion can be induced by quadruple shift, and Overhauser field relaxation time up to 1 hour was seen in Ref. [72].

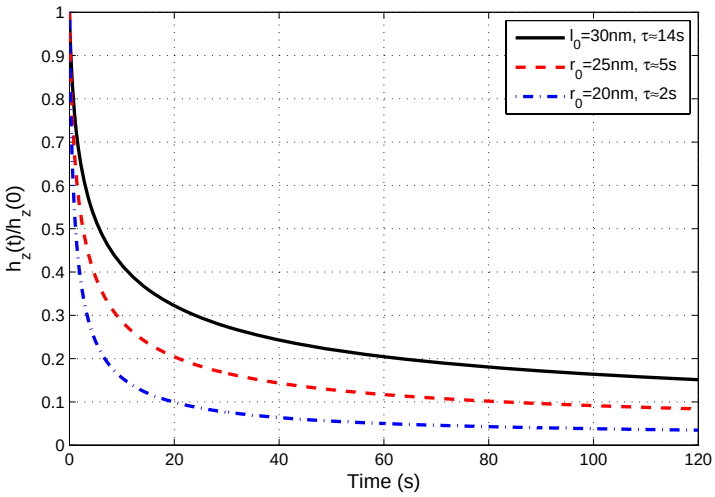

Figure 2.3.3: Decay of the Overhauser field under various initial distributions of the nuclear polarization. The solid line refers to the case with a long DNP pump time that gives a Gaussian distribution with the size characterized by the Fock-Darwin radius l_0. Other lines correspond to narrower polarization distribution characterized by a Gaussian with its size $r_0 < l_0$.

The experiment in Ref. [70] studies relaxation of the Overhauser field under different pumping time for the DNP process. With a shorter DNP pumping time, the nuclear spin polarization may have a narrower distribution in space [68]. Although we do not know the exact distribution profile of the nuclear spin polarization from a short DNP pump process, we can assume that the distribution of $\langle I_k^z \rangle$ is still simply a Gaussian but with its radius

$r_0 < l_0$, to model the experiment qualitatively. Taking this $\langle I_k^z \rangle$ as the initial condition, we can calculate relaxation of the corresponding Overhauser field from the same diffusion equation [Eq. (2.2.26)], and the result is shown in Fig. 2.3.3. The result indicates that a narrower distribution of initial nuclear spin polarization leads to a faster decay of the Overhauser field, which is consistent with the experimental result in Ref. [68]. This effect can be explained by noting that diffusion is much stronger near the center of the dot due to the electron mediated diffusion peak (see Fig. 2.2.1), so a shorter relaxation time is obtained if the initial polarization is more concentrated near the dot center.

2.4 Discussion

In our calculation, we ignored the quadruple shifts of nuclear spins, which is non-existent in certain systems such as ^{13}C-nanotube quantum dots [78], negligible in strain-free semiconductor nanostructures such as epitaxially grown droplet quantum dots [79], and dominated by Zeeman energy under magnetic field B_0 much larger than equivalent quadruple magnetic field B_Q (on the order of 0.1T for InAs quantum dot as in Ref. [72]). For quantum dot with strong inhomogeneous strain-induced quadruple shifts, we believe that nuclear spin diffusion will be further suppressed by them in a similar way as by the inhomogeneous Knight shift (detailed influence of quadruple shifts on nuclear spin dynamics can be found in Ref. [80]). We also note that considering more than one species of nuclei in the diffusion process, as in real experiments, should give a moderate increase of diffusion coefficient because more nuclear spin flip-flop channels (including those between two different species of nuclei) will be involved, but is unlikely to alter the electron's role in nuclear spin diffusion we discussed above.

Our results can provide researchers the techniques of maintaining DNP generated Overhauser field sufficiently long for the practice of quantum computation. First, we can apply a large magnetic field to effectively suppress the electron mediated nuclear spin diffusion. Second, we can choose quantum dot system with large inhomogeneous Knight shift or quadruple shift to suppress the intrinsic nuclear dipole-dipole spin diffusion. These methods together, can give us a rather long relaxation time of the Overhauser field.

The work here focused on the time dynamics of the **expectation value** of Overhauser field, since this is the quantity that has been measured in several recent experiments. Similar methods could apply to calculate the dynamics of the **variance** of Overhauser field, and in terms of time scale, they should be more or less the same. We also want to point out here that during the DNP process, nuclear spin diffusion also takes place. The final distribution of the nuclear spin polarization and its variance may depend on a balance between the DNP pump rate and the nuclear spin diffusion rate [34, 36–38, 67]. To understand this balance, a detailed knowledge of the specific DNP process will be required. The calculation method presented in this chapter fully incorporates electron's role in nuclear spin diffusion, which will facilitate further understanding of DNP process, in hope of maximizing its power in enhancing electron spin coherence time in quantum dot based device.

Chapter 3

Universal quantum gate protocol with quantum dot molecule

3.1 Introduction

In the previous chapter, we have focused on the environment of the electron spin confined in quantum dot, which has great influence on the decoherence time of the qubit. Now we turn to the question of how we can control the qubit to perform tasks of quantum computation. It was proven that any quantum algorithm can be implemented with a specific set of single and two qubit quantum logic gates, known as universal quantum gates [1, 3]. For electrically gated double quantum dot system, universal quantum gates have been experimental demonstrated [81], but the gate speed is slow ($\sim \mu s$) due to weak inter-dot spin exchange coupling. To successfully perform a quantum algorithm that may consist of hundreds of elementary single or two qubit gates, the gate speed need to be significantly higher than the decoherence rate of spin qubit. The optically controlled single quantum dot system instead, has accomplished ultrafast single qubit universal quantum control on time scale of picosecond [82], while achieving ultrafast two qubit gate in such

system remains an experimental challenge.

Recently, another competitive platform for quantum dot based quantum computation has emerged, which is comprised of optically controlled, vertically stacked double layer self-assembled InAs QDs [39, 40] (See Fig.3.1.1). The electrons can tunnel between the thin barrier across the layers, allowing for a kinetic spin exchange interaction on the order of 30GHz, significantly larger than horizontally placed double quantum dot samples (which is typically on the order of 100MHz [22]). As a result, ultrafast two qubit gates (~ 150ps) have been successfully demonstrated based on this system [39]. However, universal quantum computation is still a step away due to insufficient control on two-qubit Hilbert space. The individual single-spin rotation requires the access to exciton levels (Raman transition), which can be performed in only one of the dot by laser, since creating exciton in the other dot will cause unwanted decay channels and cross-dot transitions, leading to uncontrolled error in quantum gate operations.

The target of our work described in this chapter is to achieve complete two qubit control with such limited control. Our proposed method only requires a simple time domain engineering of gate pulses, which is within the reach of current experimental technology.

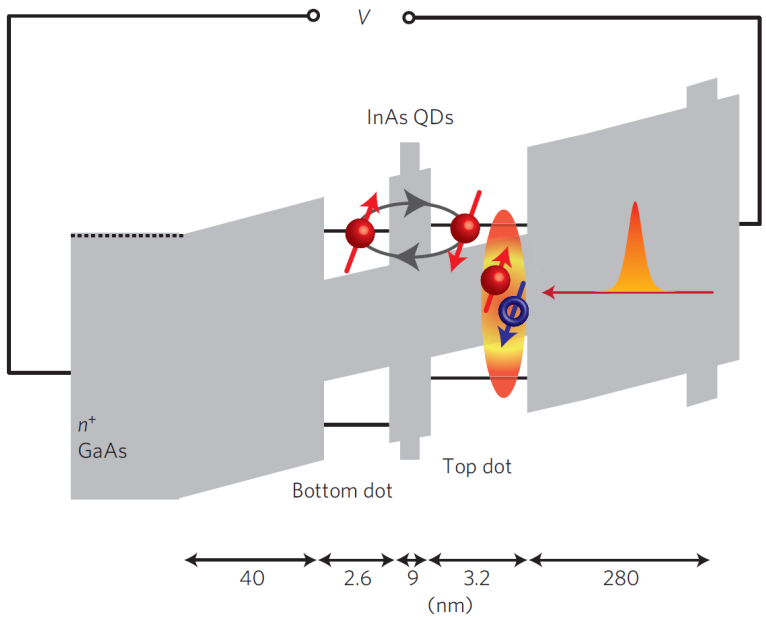

Figure 3.1.1: Diode structure of vertically stacked quantum dot molecule (QDM). The spins in the two QDs are coupled by coherent tunneling through a thin barrier. Laser fields are used to initialize, measure or rotate the spins through a real or virtual electron–hole pair (exciton) resonantly excited in the top dot (figure and caption from Ref. [39]).

3.2 Formalism

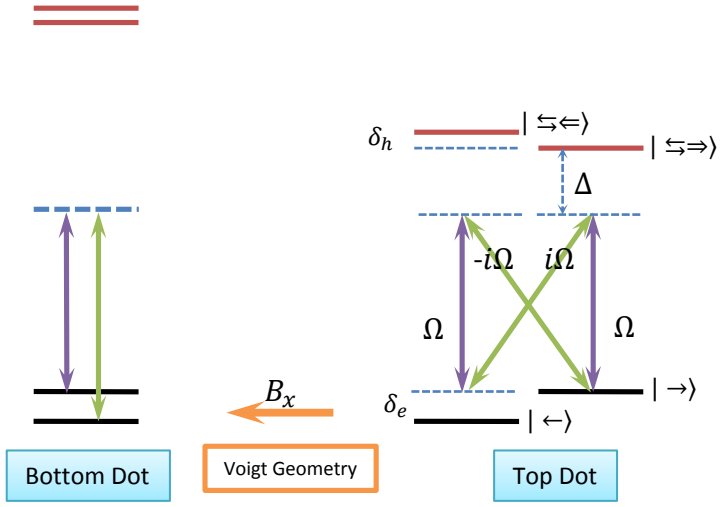

Figure 3.2.1: Level structure of QDM. A circularly polarized laser couples both H and V transitions for the top dot (shown in arrow) and is off-resonant from the bottom dot.

The relevant level structure of QDM system is shown in Fig. 3.2.1 [39, 40]. The Hamiltonian without applying any laser is given by ($\hbar = 1$) :

$$H_0 = J\mathbf{S}_1 \cdot \mathbf{S}_2 + \delta_e(S_1^z + S_2^z) \tag{3.2.1}$$

where S_1/S_2 correspond to bottom/top dot electron spin, J is the constantly-on kinetic exchange interaction, and δ_e is the Zeeman splitting from external static magnetic field applied on both dots in Voigt geometry (z direction in the Hamiltonian). In typical experiment (and also assumed in following numerical calculations), $J \approx 30$GHz and $\delta_e \approx 10$GHz per Tesla [40].

We then apply a circularly polarized pulse laser with electric field $E(t) = E_0(t)[\frac{\hat{\epsilon}_V + i\hat{\epsilon}_H}{\sqrt{2}} e^{i(\omega t+\phi)} + c.c]$ with $E_0(t)$ being the slowly varying pulse envelope function [82]. Define the Rabi fre-

quency $\Omega(t) = \mu E_0(t)e^{-i\phi}/\hbar$. Assume the laser frequency is detuned Δ from the top dot exciton transition (see Fig. 3.2.1). The bottom dot exciton transition is fabricated to be very different from the top dot, so it's far off-resonant and simply appears dark to the pulse. The atom-field Hamiltonian for top dot in rotating wave approximation & field interaction picture reads (up to a constant):

$$H_{top} = \begin{array}{c|cccc} & \Leftarrow & \Rightarrow & \rightarrow & \leftarrow \\ \Leftarrow & \Delta+\delta_h & 0 & -\frac{i}{\sqrt{2}}\Omega & \frac{1}{\sqrt{2}}\Omega \\ \Rightarrow & 0 & \Delta & \frac{1}{\sqrt{2}}\Omega & \frac{i}{\sqrt{2}}\Omega \\ \rightarrow & \frac{i}{\sqrt{2}}\Omega^* & \frac{1}{\sqrt{2}}\Omega^* & 0 & 0 \\ \leftarrow & \frac{1}{\sqrt{2}}\Omega & -\frac{i}{\sqrt{2}}\Omega^* & 0 & -\delta_e \end{array}$$

By choosing $\Delta \gg \Omega, \frac{d\Omega}{dt}, \delta_e, \delta_h$, the trion states population is negligible (spontaneously emission can also be ignored then) and one can adiabatically eliminate the trion states to obtain the Hamiltonian in ground state manifold:

$$H_{top} \approx \begin{array}{c|cc} & \rightarrow & \leftarrow \\ \rightarrow & \frac{|\Omega|^2}{\Delta} & \frac{i|\Omega|^2}{\Delta} \\ \leftarrow & \frac{-i|\Omega|^2}{\Delta} & \frac{|\Omega|^2}{\Delta}-\delta_e \end{array} = -\Omega_{eff}S_2^y + \delta_e S_2^z + \text{constant}$$

where $\Omega_{eff} = |\Omega|^2/\Delta$. By changing the axis label $-y \to x \quad x \to y$ (no physics affected), one can write down the effective QDM Hamiltonian under laser pulse:

$$
\begin{aligned}
H &= H_0 + H_1(t) \qquad (3.2.2)\\
H_0 &= J\mathbf{S}_1 \cdot \mathbf{S}_2 + \delta_e(S_1^z + S_2^z)\\
H_1 &= \Omega_{eff}(t) S_2^x
\end{aligned}
$$

Although we only have laser control on one of the spin by naively looking at Eq. 3.2.2, due to the constantly-on exchange interaction, it is nevertheless possible to obtain universal two-qubit quantum control (as long as one does not have accidental symmetry caused by the case $\delta_e = J$) through proper engineering of $\Omega_{eff}(t)$. To prove this possibility, let's first look at the evolution operator $U(t) = \mathcal{T} e^{-i\int_0^t H(t')dt'}$. This time-ordered integral can be treated with the so-called Magnus expansion [83]:

$$
U(t) = e^{-i\int_0^t H(t')dt' - \frac{1}{2!}\int_0^t dt' \int_0^{t'} dt''[H(t''),H(t')] - \frac{i}{3!}\int_0^t dt' \int_0^{t'} dt'' \int_0^{t''} dt'''\{[H(t'''),[H(t''),H(t')]]+[H(t'''),H(t'')],H(t')]\}+\cdots}
$$

The first order unequal time commutator is:

$$
\begin{aligned}
[H(t_1), H(t_2)] &= [H_0, H_1(t_2)] + [H_1(t_1), H_0]\\
&= [H_0, H_1(t_2) - H_1(t_1)]\\
&= (\Omega_2 - \Omega_1)[J\mathbf{S}_1 \cdot \mathbf{S}_2 + \delta_e(S_1^z + S_2^z),\ S_2^x]\\
&= i(\Omega_2 - \Omega_1)(JS_1^z S_2^y - JS_1^y S_2^z + \delta_e S_2^y)
\end{aligned}
$$

where $\Omega_i \equiv \Omega_{eff}(t_i)$. The next order is:

$$
\begin{aligned}
[H(t_3),[H(t_1),H(t_2)]] &= i(\Omega_2-\Omega_1)[J\mathbf{S}_1\cdot\mathbf{S}_2+\delta_e(S_1^z+S_2^z)+\Omega_3 S_2^x,\ JS_1^zS_2^y-JS_1^yS_2^z+\delta_e S_2^y] \\
&= -(\Omega_2-\Omega_1)[2J^2(S_1^x-S_2^x) \\
&\quad +2J\delta_e(S_1^xS_2^z-S_1^zS_2^x)-\delta_e^2S_2^x+\Omega_3J(S_1^zS_2^z+S_1^yS_2^y)+\Omega_3\delta_eS_2^z]
\end{aligned}
$$

If one further calculates the next next order term $[H(t_4),[H(t_3),[H(t_1),H(t_2)]]]$, all 15 generators of $SU(4)$ group $\{S_1^i,\ S_2^i,\ S_1^iS_2^j\}$ $(i,j=x,y,z)$ will show up. As $\Omega_{eff}(t)$ can have arbitrary value at different time t_i. One can generate any linear combinations of these 15 generators to give arbitrary $SU(4)$ operation, which is equivalent of implementing universal two-qubit gate (up to a global $U(1)$ phase).

3.3 Experimental Protocol

An experimentally realistic way of engineering $\Omega_{eff}(t)$ is to use M equally spaced segments with variable intensity. When the segment duration is on the order of $\tau=100ps$, this type of engineering can be done in practice through modulating a continuous-wave laser. The segmented pulse setting allows the evolution operator

$$U(t)=\mathcal{T}e^{-i\int_0^t(H_0+H_1(t')dt'}$$

to be easily calculated numerically one segment by one segment:

$$U(t)\approx e^{-iH(t+(M-1)\tau)\tau}\cdots e^{-iH(\tau)\tau}e^{-iH(0)\tau} \tag{3.3.1}$$

with

$$H(t) = J\mathbf{S}_1 \cdot \mathbf{S}_2 + \delta_e(S_1^z + S_2^z) + \Omega_{eff}^m S_2^x \quad (m-1)\tau \leq t < m\tau \quad (m = 1, 2, \ldots M)$$

If U_G is the desired quantum gate operation in the two-qubit Hilbert space, we calculate the gate fidelity for a given initial state $|\psi_i\rangle$:

$$F = |\langle\psi_i|U_G^\dagger U|\psi_i\rangle|^2$$

One can then invoke numerical optimization over M variables $\{\Omega_{eff}^m\}$ to maximize the gate fidelity F.

In Fig. 3.3.1, we show by numerical simulation that for a small number of segments ($M = 8$), by optimizing the segments' Rabi frequencies, one can achieve any two qubit gate almost perfectly. The required (Raman) Rabi frequency for each segment is approximately on the order of $J \sim 30$GHz, which is within current experimental limit [39].

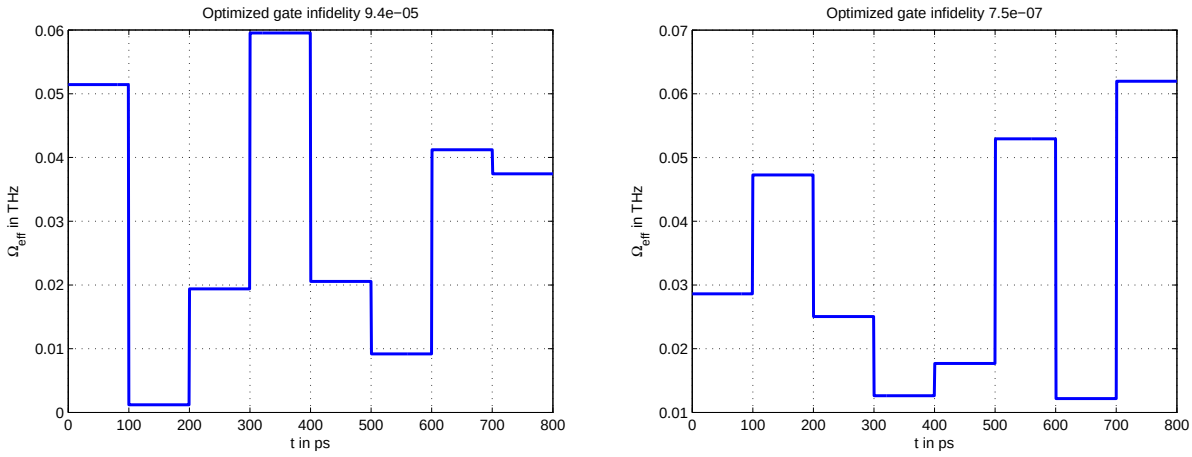

Figure 3.3.1: Optimized segmented pulse shape for near perfect universal two-qubit gate. (Left) CNOT with bottom dot spin as control qubit and top dot spin as target qubit. (Right) $\pi/8$ gate on the top dot spin. The initial state is set to the spin singlet state and QDM parameters are chosen in accordance with Ref. [39]

To show that we have coherent control over the two-qubit Hilbert space, we can tune the global pulse amplitude (by using an attenuator for example) and measure the state population in the stationary singlet-triplet basis of free Hamiltonian Eq. 3.2.1:

$$\begin{aligned} |S\rangle &= (|\uparrow\downarrow\rangle - |\downarrow\uparrow\rangle)/\sqrt{2} \\ |T_0\rangle &= (|\uparrow\downarrow\rangle + |\downarrow\uparrow\rangle)/\sqrt{2} \\ |T_-\rangle &= |\downarrow\downarrow\rangle \\ |T_+\rangle &= |\uparrow\uparrow\rangle \end{aligned}$$

The anticipated results are shown in Fig. 3.3.2, which can be readily verified experimentally.

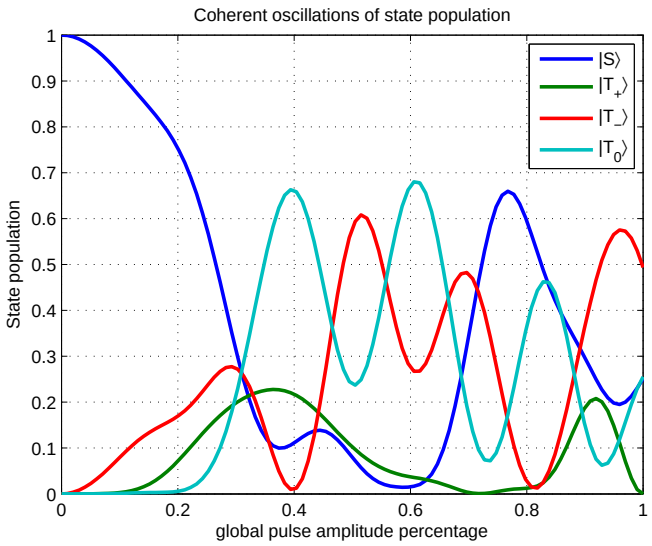

Figure 3.3.2: Coherent oscillations of stationary state population by tuning global pulse amplitude from 0% to 100%. The pulse shape is the same as the CNOT gate case in Fig. 3.3.1. At 100% amplitude, it gives a perfect CNOT gate with initial state in singlet.

3.4 Discussion

We give a brief discussion on the errors that may occur in the above protocol. First, for each pulse to perform non-negligible rotation in two-qubit Hilbert space, we need $\Omega^m_{eff}\tau \gtrsim \pi$. There the faster gate time, the stronger lase power is required. However, because in deriving the effective Hamiltonian (Eq. 3.2.2) we have assumed $\Delta \gg \Omega^m_{eff}, \tau^{-1}$, the gate speed is limited by the Δ, which is further limited by the optical transition frequency difference between the top and bottom dots. In reality, Δ is on the order of 100GHz [39] so by having $\Omega^m_{eff} \sim 30$GHz, we already have about 10% trion state population, which will cause quantum gate error due to leakage out of computational subspace.

The gate time with $M = 8$ segments is roughly 800ps in the above examples, but the spin coherence time reported in [39] is only $400 - 700$ps, so errors caused by decoherence

may also be non-negligible. However, this coherence time is expected to get substantially improved by suppressing electric field fluctuation [39] . We believe that a combined effort of enhancing electron-spin coherence time and employing optimal pulse control will offer us the power brought by ultrafast and high-fidelity quantum gate in quantum dot systems.

Chapter 4

Robust quantum state transfer between remote NV registers

4.1 Introduction

Reliable quantum state transfer between distant qubits forms an essential ingredient of any scalable quantum information processor [25]. However, most direct qubit interactions are short-range and the corresponding interaction strength decays rapidly with physical separation. For this reason, most of the feasible approaches that have been proposed for quantum computation rely upon the use of quantum channels which serve to connect remote qubits; such channels include: electrons in semiconductors [84], optical photons [85–87], and the physical transport of trapped ions [88]. Coupled quantum spin chains have also been extensively studied [89–101]. A key advantage of such spin chain quantum channels is the ability to manipulate, transfer, and process quantum information utilizing the same fundamental hardware [102]; indeed, both quantum memory and quantum state transfer can be achieved in coupled spin chain arrays [103], eliminating the requirement for an external interface between the quantum channel and the quantum register. Prior

work on spin chain quantum channels has focused on three distinct regimes, in which the spin chain is either initialized [89, 96, 97, 101], engineered [91] or dynamically controlled [93, 104–106].

An important application of spin-chain mediated coherent coupling is in the context of realizing a room temperature quantum information processor based upon localized spins in the solid-state [107]. In this case, it is difficult to envision mechanical qubit transport, while other coupling mechanisms are often not available or impose additional prohibitive requirements such as cryogenic cooling [87]. At the same time, long spin chains are generally difficult to polarize, impossible to control with single-spin resolution, and suffer from imperfect spin-positioning [98, 99]; such imperfections can cause both on-site and coupling disorder, resulting in localization. For these reasons, a detailed understanding of quantum coherence and state transfer in random spin chains with a limited degree of external control is of both fundamental and practical importance.

In this chapter, we propose and analyze a novel method for quantum state transfer (QST) in an unpolarized, infinite temperature spin chain. In contrast to prior work, the method requires neither external modulation of the Hamiltonian evolution nor spin chain engineering and initialization. Furthermore, it is robust to specific, practically important types of disorder. The structure of this chapter is as follows: in section 4.2 we introduce the main idea of our QST protocol, based on free fermion state transfer (FFST). In section 4.3, we extend the protocol to cases with strong chain-register coupling and cases with long range spin-spin interaction. We end this chapter by discussing experimental realization of our protocol using defect centers in diamond.

4.2 Formalism

The key idea of our approach is illustrated in Fig. 4.2.1(a). The two spin qubits at the ends of the spin chain are assumed to be initialized and fully controlled, while the coupling between these remote qubits is mediated by a set of intermediate spins, which can not be initialized, individually controlled, or optically detected. We further assume that the qubit-chain coupling g, which can be variably adjusted, and the intrachain coupling κ, which is fixed, are characterized by short-range XX interactions. The essence of our quantum state transfer protocol is the long-range coherent interaction between the spin qubits, mediated by a specific collective eigenmode of the intermediate spin chain. This mode is best understood via Jordan-Wigner (JW) fermionization, which allows for the states of an XX spin chain to be mapped into the states of a set of non-interacting spinless fermions. In this representation, the state transfer is achieved by free fermion tunneling, as shown in Fig. 4.2.1(b). In what follows, we show that the initial state of the intermediate chain does not affect the tunneling rate associated with free fermion state transfer (FFST), allowing for the implementation of a SWAP operation between the end qubits after a period of unitary evolution.

To be specific, we consider an XX Hamiltonian governing two distant qubits connected by a quantum channel consisting of a spin-$1/2$ chain

$$H = H_0 + H' \tag{4.2.1}$$

with $H_0 = \sum_{i=1}^{N-1} \kappa(S_i^+ S_{i+1}^- + S_i^- S_{i+1}^+)$ and $H' = g(S_0^+ S_1^- + S_{N+1}^+ S_N^- +$ h.c.), as shown in Fig. 4.2.1(a). Here, $S^{\pm} = S^x \pm iS^y$, where $\vec{S} = \vec{\sigma}/2$ and $\vec{\sigma}$ are Pauli spin operators ($\hbar = 1$). We consider the limit $g \ll \kappa$, and work perturbatively in H'. Upon introducing Fermi op-

erators $c_i = e^{i\pi \sum_0^{i-1} S_j^+ S_j^-} S_i^-$, H_0 is transformed to $H_0 = \sum_{i=1}^{N-1} \kappa(c_i^\dagger c_{i+1} + c_i c_{i+1}^\dagger)$, wherein conservation of total spin z-projection becomes conservation of fermion number [108]. The subsequent diagonalization of this tight-binding Hamiltonian occurs through an orthogonal transformation $f_k^\dagger = \frac{1}{A} \sum_{j=1}^{N} \sin \frac{jk\pi}{N+1} c_j^\dagger$ with $k = 1, \cdots, N$ and $A = (\frac{N+1}{2})^{1/2}$, yielding $H_0 = \sum_{k=1}^{N} E_k f_k^\dagger f_k$, where $E_k = 2\kappa \cos \frac{k\pi}{N+1}$ [108]. The perturbation Hamiltonian is likewise transformed to

$$H' = \sum_{k=1}^{N} t_k (c_0^\dagger f_k + (-1)^{k-1} c_{N+1}^\dagger f_k + \text{ h.c.}), \tag{4.2.2}$$

where $t_k = \frac{g}{A} \sin \frac{k\pi}{N+1}$. We begin by restricting our discussion to odd N, where there exists a single zero energy fermionic mode in the intermediate chain corresponding to $k = z \equiv (N+1)/2$. Thus, the two end spins are resonantly coupled to the zero energy fermion by H', and under the assumption that the tunneling rate $t_z \sim g/A$ is much smaller than the fermion detuning, $|E_z - E_{z\pm1}| \sim \kappa/N$, off-resonant coupling to other fermionic modes can be neglected. Upon absorbing a phase factor of $(-1)^{z-1}$ into $c_{N+1}^\dagger$, evolution is governed by the effective Hamiltonian, $H_{eff} = t_z(c_0^\dagger f_z + c_{N+1}^\dagger f_z + \text{ h.c.})$, which describes resonant fermionic tunneling, as shown in Fig. 4.2.1(b).

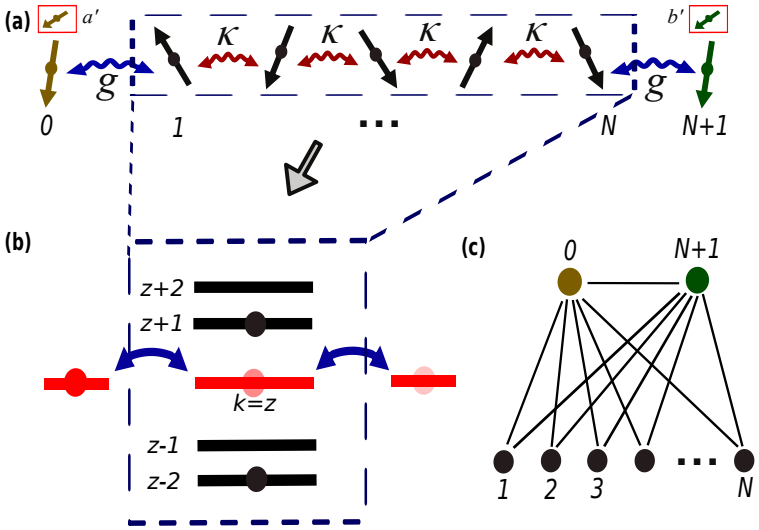

Figure 4.2.1: Schematic of FFST protocol. (a) Distant spin qubits coupled by an unpolarized spin-chain quantum channel with g, the coupling between qubits (yellow, green) and the spin chain and κ, the coupling between intra-chain elements. The spin chain can be re-expressed in terms of free fermions via the Jordan-Wigner transformation, wherein the hopping strength is characterized by κ. Boxed spins, labeled a' and b', represent additional spin qubits that can correspond to the memory of a quantum register or ancillary qubits associated with quantum information encoding. (b) By ensuring that the end spins are resonant with a single fermion mode ($k = z$), unpolarized spin-chain state transfer becomes analogous to fermionic tunneling. Maintaining $g \ll \kappa/\sqrt{N}$ ensures that off-resonant coupling to other fermionic modes can be neglected and enables state transfer independent of the intermediate spin-chain state. (c) Graph-like state generated by FFST, between the qubits and the intermediate spin chain [95]. Each line represents a controlled-phase gate.

Unitary evolution under H_{eff} for a time $\tau = \frac{\pi}{\sqrt{2}t_z}$ results in $U_{eff} = e^{-i\tau H_{eff}} = (-1)^{f_z^\dagger f_z}(1-(c_0^\dagger+c_{N+1}^\dagger)(c_0+c_{N+1}))$. Upon projection to the subspace spanned by $\{(1, c_0^\dagger, c_{N+1}^\dagger, c_0^\dagger c_{N+1}^\dagger)|00\rangle_{0,N+1}\}$, the effective evolution can be expressed as

$$U_{eff}^{fermi} = (-1)^{n_0+n_{N+1}+n_z}(-1)^{n_0 n_{N+1}}\text{SWAP}_{0,N+1}, \tag{4.2.3}$$

where $n_\theta = f_\theta^\dagger f_\theta$ is the fermion number operator. Hence, as desired, time evolution under H_{eff} swaps the quantum state of the two end fermions. However, in addition to the

SWAP gate and single fermion rotations, the end fermions are entangled through a controlled phase gate $\mathrm{CP}_{0,N+1} = (-1)^{n_0 n_{N+1}}$, which arises from fermionic anticommutation relations [93, 95, 109]. Before discussing this entanglement, let us first consider the analogous prescription in the spin basis.

We consider a generic initial state $\Phi_i = (\alpha|\downarrow\rangle + \beta|\uparrow\rangle)_0 \otimes (\alpha'|\downarrow\rangle + \beta'|\uparrow\rangle)_{N+1} \otimes \Psi_{M,n_z}$ where Ψ represents the intermediate spin chain state, characterized as the co-eigenstate of commuting operators $M = \sum_{j=1}^{N} S_j^+ S_j^-$ and n_z. After fermionization, evolution and inversion back to the spin basis, the final spin chain state becomes

$$\Phi_f = (\prod_{j=1}^{N} \mathrm{CP}_{0,j}\mathrm{CP}_{N+1,j})\mathrm{CP}_{0,N+1}\mathrm{SWAP}_{0,N+1}\Phi_i \tag{4.2.4}$$

up to single qubit rotations. In this basis, the Wigner-strings become controlled-phase gates and generate a graph-like entangled state between the two end spins and the intermediate spins, as shown in Fig. 4.2.1(c) [95].

Despite this entanglement, the use of a simple two-qubit encoding can achieve coherent quantum state transfer [110]. The quantum information is encoded in two spins, a and a', with logical basis $|\downarrow\rangle = |\downarrow\rangle_a|\downarrow\rangle_{a'}$, $|\uparrow\rangle = |\uparrow\rangle_a|\uparrow\rangle_{a'}$. After encoding, one first performs FFST between spins a and b via the unpolarized spin chain, and then, repeats the operation between spins a' and b', as shown in Fig. 4.2.1(a). Finally, the quantum information is decoded by applying a CNOT gate between spins b and b', after which, the information has been coherently mapped to spin b. Thus, we have demonstrated the ability to perform QST between spatially separated spin qubits. Furthermore, as detailed in the subsequent section on experimental realizations utilizing Nitrogen-Vacancy registers, we offer an alternative solution which achieves remote coupling of spatially separated quantum registers through

a dual-transfer protocol.

To confirm perfect quantum state transfer, we perform numerics, as shown in Fig. 4.2.2. Specifically, we calculate the average fidelity, $F = \frac{1}{2} + \frac{1}{12}\sum_{i=1,2,3} \mathrm{Tr}\left[\sigma^i \mathcal{E}(\sigma^i)\right]$, of two-qubit encoded state transfer, where $\mathcal{E}$ represents the quantum channel consisting of encoding, state transfer and decoding [111]. This average fidelity can be expressed in terms of elements of the matrix $e^{-iK\tau}$, where K is the $N \times N$ coupling matrix of the full Hamiltonian found in $H = \sum_{i,j} K_{i,j} S_i^+ S_j^-$ (see Appendix A for details); crucially, this allows for simulations of channel fidelity in extremely long spin chains, since diagonalization of the full Hilbert space is no longer necessary. In finite chains of fixed length, the infidelity, $\epsilon = 1 - F$, varies as a function of g/κ, as shown in Fig. 4.2.2(a). This infidelity results from the leakage of quantum information into the off-resonant modes of the intermediate spin chain, and can be analytically expressed, in the limit $g \ll \kappa$, as $\epsilon \approx \sum_{k \neq z} \frac{5}{3} \left(\frac{t_k}{E_k}\right)^2 \left[1 + (-1)^{k+z} \cos(E_k \tau)\right]$, where $z = \frac{N+1}{2}$ [44]. In this limit, the analytic expression is in exact agreement with the numerics, and is upper-bounded by the theoretical estimate, $\sum_{k \neq z} \frac{10}{3} \left(\frac{t_k}{E_k}\right)^2$, as shown in Fig. 4.2.2(a).

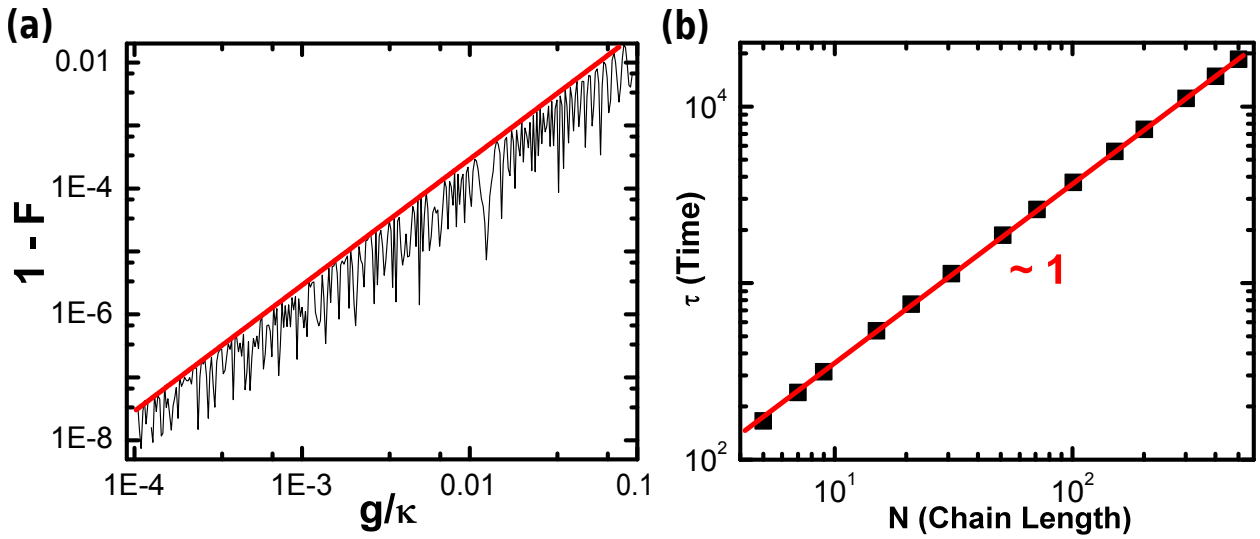

Figure 4.2.2: (a) Numerical simulation of the infidelity of QST for $N = 7$ as a function of g/κ depicting fluctuations in the infidelity. The numerical infidelity is bounded by the theoretical estimate (bold line). (b) For a chosen tolerable infidelity $\epsilon_0 = 10^{-3}$, the minimum time τ (in units of $1/\kappa$), required for state transfer scales linearly with chain length.

Utilizing the analytic upper bound for a given chain length N, a given intra-chain coupling κ, and a given tolerable infidelity ϵ_0, we can compute the maximum allowed g and hence the minimum state transfer time τ. By contrast to direct dipole-dipole interactions, which would depict a cubic scaling of τ with N, the time required for FFST scales linearly with chain length, as shown in Fig. 4.2.2(b) [112]. Intuitively, this results from the fact that the condition on t_z allowing for off-resonant coupling to be neglected is $t_z \ll \kappa/N$, implying that $\tau \sim 1/t_z \sim N/\kappa$.

While we have chosen to focus on the case of odd N length intermediate chains, the extension to even N is directly analogous. In even N chains, since the fermion eigenspectrum is symmetric about $E = 0$, no fermionic eigenmode is initially resonant with the end spin qubits. However, by introducing a controllable detuning to the end spins, $H_\Delta = \Delta(S_0^z + S_{N+1}^z)$, it is possible to choose an N-dependent Δ such that the end spins are

resonant with any single fermion eigenmode in both even *and* odd N cases. In particular, for $\Delta = E_k$, resonant tunneling will occur at the rate t_k, allowing for control over the speed of FFST.

4.3 Extension

4.3.1 Strong Coupling Regime

The eigenmode-mediated QST discussed above operates in the weak coupling regime, $g \ll \kappa/N$. Numerical simulations reveal that by optimally tuning $g = g_M(N) \sim \kappa$, high-fidelity QST can also be achieved (see Fig. 4.3.2). This "strong-coupling" regime enables faster state transfer and has been discussed in several recent studies [101,113–115], which focus on the case of an initially polarized intermediate chain. Here, we show that chains with infinite spin-temperature can still support QST in the strong-coupling regime.

To provide intuition for this strong-coupling regime, we will begin by considering the engineered spin-chain described in [91], where we have $N+2$ spin-1/2 atoms with nearest-neighbor XX-interactions. The intra-chain coupling is non-uniform and is given by, $J_i = \frac{1}{2}\sqrt{(i+1)(N+1-i)}$, yielding a Hamiltonian

$$H = \sum_{i=0}^{N} J_i(\sigma_i^+\sigma_{i+1}^- + h.c.) + \sum_{i=0}^{N+1} \frac{h}{2}\sigma_i^z, \tag{4.3.1}$$

where h is a uniform background magnetic field. Upon employing the Jordan Wigner transformation, we once again return to a simple tight-binding form, with $H = \sum_{ij} K_{ij} c_i^\dagger c_j$ where $K_{ij} = J_i\delta_{j,i+1} + J_j\delta_{i,j+1} + h\delta_{i,j}$ up to a constant. Diagonalizing reveals $H = \sum_{k=0}^{N+1} \omega_k f_k^\dagger f_k$ with a linear spectrum given by $\omega_k = k + h - \frac{N+1}{2}$.

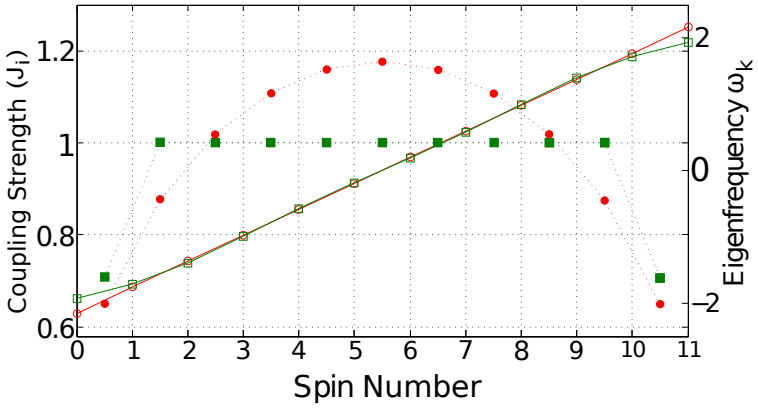

Figure 4.3.1: Coupling pattern $\{J_i\}$ between spins for two differing cases: 1) engineered couplings (circles) as in [91] and 2) strong coupling regime (squares). The left y-axis characterizes the coupling strength for each case and is associated with solid symbols; the couplings are plotted between spin numbers (e.g. J_0 is plotted between spin number 0 and 1). The right y-axis characterizes the fermionic spectrum (in this case, the x-axis is simply an index) and is associated with the open symbols. The open red circles depict the exactly linear spectrum of engineered chain, while the open green squares depict the quasi-linear spectrum of the strong coupling case with uniform interchain couplings $\kappa = 1$ and optimized $g \approx 0.7$.

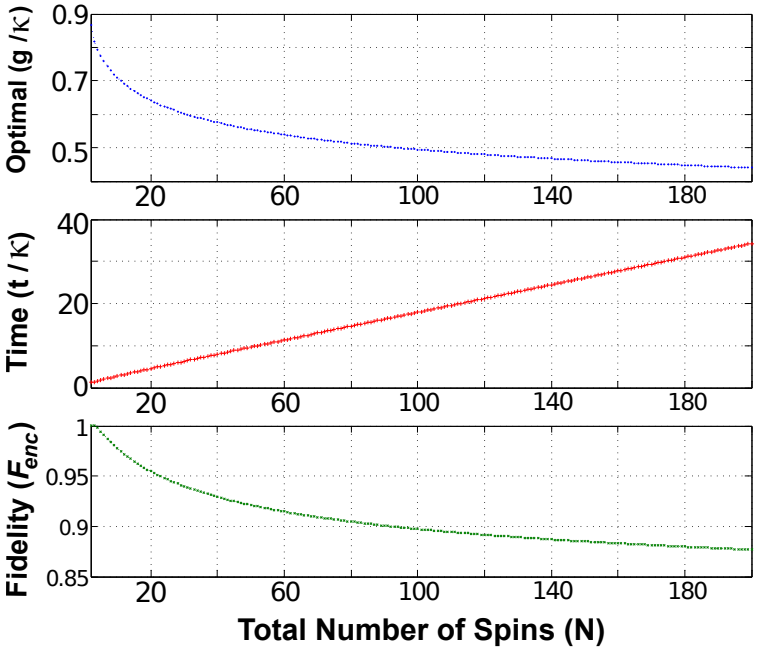

Figure 4.3.2: Strong coupling regime: By tuning $g/\kappa \sim N^{-1/6}$, we obtain high-fidelity QST utilizing an unpolarized chain with two-qubit encoding (paired-protocol). The transfer time scales linearly with N (Lieb-Robinson bound) and high fidelity $> 90\%$ can be maintained for chain lengths up to $N = 100$.

As described in Appendix A, the system's evolution is governed by $c_i(t) = \sum_j M_{ij}(t)c_i(0)$. Upon setting $h = \frac{N+1}{2}$, one finds that at time $t = 2\pi$, $M(2\pi) = \mathbb{I}$ and therefore $c_i(2\pi) = c_i(0)$, returning the system to its initial state. As the coupling pattern $\{J_i\}$ harbors mirror symmetry with $J_i = J_{N-i}$, the orthogonal transformation, ψ, which diagonalizes H can also be chosen mirror symmetric, $\psi_{ik} = (-1)^{N+1+k}\psi_{N+1-i,k}$. Setting $h = \frac{3}{2}(N+1)$ and $t = \pi$ yields,

$$M_{ij} = \sum_k \psi_{N+1-i,k}\psi_{jk} = \delta_{N+1-i,j}. \tag{4.3.2}$$

To demonstrate state transfer, let us employ the analytic single-swap fidelity given in Appendix A. For the moment, we assume that the spins $\{0, 1, \ldots N\}$ are all polarized, so that $\mathrm{Tr}[\rho_{ch}^{SS}P] = 1$. Combined with Eq. (4.3.2), which ensures $M_{0,N+1} = 1$, we find $F_{SS} = 1$, en-

abling perfect QST. We note that in lieu of applying a uniform magnetic field $h = \frac{3}{2}(N+1)$, one can also just apply a simple phase gate $U_P = \begin{pmatrix} 1 & 0 \\ 0 & (-i)^{N+1} \end{pmatrix}$ on spin 0 following transfer.

Turning now to the case of an unpolarized spin chain, we again employ the two-qubit encoding previously described. In this case, one will need to apply the phase gate, $U_P^2 = \begin{pmatrix} 1 & 0 \\ 0 & (-1)^{N+1} \end{pmatrix}$ to the logical qubit after state transfer.

The state transfer fidelities for these two strong coupling methods are given analogously by,

$$F_{SS} = \frac{1}{2} + \frac{1}{6}[2|M_{0,N+1}| + |M_{0,N+1}|^2), \tag{4.3.3}$$

$$F_{enc} = \frac{1}{2} + \frac{1}{6}[2|M_{0,N+1}|^2|M_{0,N+1}^2 - M_{0,0}M_{N+1,N+1}| + |M_{0,N+1}|^2 + |\sum_{i=1}^{N} M_{N+1,i}M_{i,0}|^2]. \tag{4.3.4}$$

While these expressions are valid for an arbitrary coupling pattern (so long as the resultant fermionic Hamiltonian is quadratic), to ensure high-fidelity QST, we require $|M_{0,N+1}| \approx 1$. As depicted in Eq. (4.3.2), satisfying this constraint is intimately related to the linear spectrum resulting from the choice of $J_i = \frac{1}{2}\sqrt{(i+1)(N+1-i)}$.

Let us now consider the strong coupling regime ($g \sim \kappa$) where $J_0 = J_N = g$ and $J_1 = J_2 = ... = J_{N-1} = \kappa$. Surprisingly, tuning only g/κ enables one to obtain a quasi-linear spectrum [114]; such a spectrum will then ensure that $|M_{0,N+1}| \approx 1$, as desired. Of course, for $N = 2, 3$, $J_i = \frac{1}{2}\sqrt{(i+1)(N+1-i)}$ can be satisfied exactly. Although for $N > 3$, an exactly linear spectrum cannot be obtained, it is possible to optimally tune

$g = g_M(N)$, so that ω_k looks nearly identical to the previous linear spectrum, $k - \frac{N+1}{2}$ ($h = 0$), as shown in Fig. 4.3.1. In particular, by optimizing F_{enc}, we obtain $g_M \sim N^{-1/6}$, with a transfer time $\tau \sim N$ (Fig. 4.3.2), consistent with [113]

4.3.2 Long-range Interactions

We now consider the effect of longer range interactions. The majority of proposals for spin-chain state transfer, as well as what we introduced in last section, focus on approximate nearest-neighbor models; however, the microscopic magnetic dipolar interaction is naturally long-range and decays as $1/r^3$, inducing an important infidelity in quantum state transfer. The origin of this infidelity becomes especially evident as we examine the Jordan-Wigner fermionization of the spin chain. Each Wigner fermion carries a string of the form $e^{-i\pi \sum_{j=1}^{i-1} \sigma_j^+ \sigma_j^-}$. In the nearest-neighbor case, all such strings cancel pairwise leaving a simple quadratic model. However, with longer-range interactions, uncanceled strings remain and generically introduce perturbative quartic terms into the Hamiltonian. These quartic terms imply that the model, unlike the transverse field Ising model, is no longer diagonalizable in terms of free fermions. In the previous free fermion case, the energy of each eigenmode is independent of the occupation of all other eigenmodes; this enables state transfer even when the spin-temperature of the chain is effectively infinite. By contrast, the quartic terms associated with the long-range dipolar coupling introduce interactions between fermionic eigenmodes; the energy fluctuations of each eigenmode, caused by changing occupations of other modes, naturally dephases quantum information, limiting the operational spin temperature of the chain.

Certain proposals have suggested the possibility of using dynamical decoupling to effectively cancel next-to-neareast neighbor (NNN) interactions [103], but the complete can-

celing of all long-range interactions requires a level of quantum control that is currently beyond the realm of experimental accessibility. Since any long-range XX coupling destroys the quadratic nature of the fermionic Hamiltonian, an analytic solution for state transfer fidelities in the presence of full dipolar interactions is not available. Thus, we perform exact diagonalization for chains of length up to $N = 12$ (total number of spins), as shown in Fig. 4.3.3. We obtain the encoded state transfer fidelities for dipolar, NNN-canceled-dipolar and NN interaction models. Remarkably, even with full dipolar interactions, fidelities $\sim 90\%$ can be obtained for a total of $N = 10$ spins; in the case where NNN interactions are dynamically decoupled, the fidelities can be further improved to $\sim 98\%$ at similar lengths.

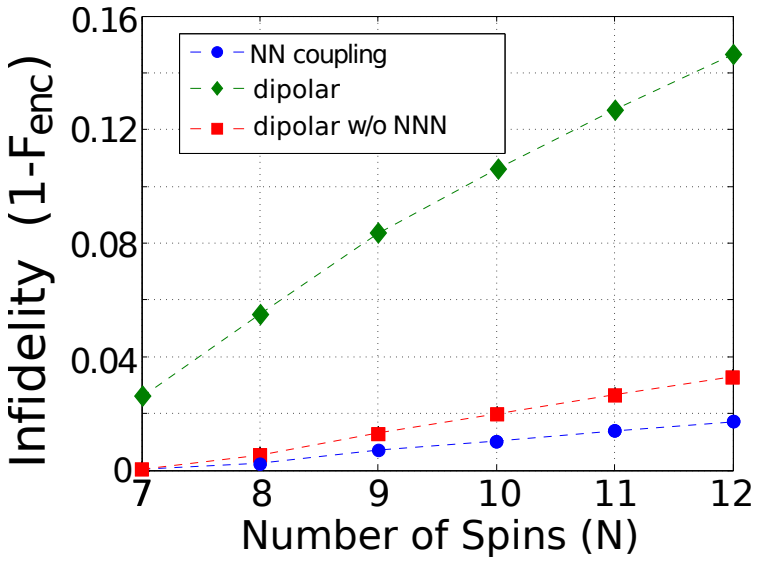

Figure 4.3.3: Infidelity of QST for a strongly coupled chain with long range interactions. Encoded state transfer (paired protocol) fidelities are shown for dipolar (diamonds), NNN-canceled-dipolar (squares) and NN interaction (circles) models.

4.4 Experimental Realization

The proposed FFST protocol can be possibly realized by Nitrogen-Vacancy (NV) registers in diamond, which have extremely long room-temperature coherence times [103]. In particular, the imperfect conversion of NV centers from single Nitrogen impurities results in substantial spatial separation between individual registers. However, the unconverted spin-1/2 Nitrogen impurities form a natural spin chain connecting remote registers. At ambient temperatures, the Nitrogen impurity spin chain, which is optically unaddressable, would be unpolarized and hence, the proposed scheme would be essential to enable distant NV register coupling.

Thus, we envision an array of two-qubit NV registers connected by a quantum channel consisting of spin-1/2 implanted Nitrogen impurities [103]. Recent experiments have demonstrated the ability to fully manipulate the two-qubit NV register corresponding to the NV nuclear spin, which serves as the memory qubit, and the NV electronic spin, which is used to initialize, readout, and mediate coupling to the intermediate spin chain [116–118]. The effective Hamiltonian described in Eq. 4.3.1 can be achieved in such a mixed spin system via dynamic decoupling, with only a small error caused by NNN interactions as shown in section 4.3, and the qubit-chain coupling g can be fully tuned by utilizing the structure of the NV center ground-state manifold [103].

Based on the FFST protocol, one can also apply arbitrary two qubit gates between the nuclear memory of distant NV registers by going through the following steps:

1. SWAP the state of the nuclear and electronic spin of the first register
2. Apply FFST between the electronic spins of the two registers
3. Apply a CP-gate between the electronic and nuclear spin of the second register

4. Repeat (2) and (1) to return the nuclear memory of the first register and disentangle from the intermediary chain.

Together with single qubit rotations, such an implementation of FFST achieves a universal set of gates and hence computation in an array of NV registers connected by Nitrogen impurity spin chains.

Finally, we discuss the effect of realistic imperfections including disorder and decoherence on our protocol. On-site and coupling disorder cause localization, asymmetry of the eigenmodes, and changes in the statistics of the eigenenergies [98, 99]. In the thermodynamic limit in 1D, localization occurs for any amount of disorder; thus, it will be necessary to utilize eigenmodes whose localization length is sufficiently large relative to the chain length, thereby rendering such modes effectively extended and viable for QST. Crucially, in the case of particle-hole (PH) symmetric disorder (e.g. coupling-strength disorder), there exists an extended critical state at $E = 0$ with a diverging localization length; this ensures the existence of an extended eigenmode with a known eigenenergy, suggesting that FFST is intrinsically robust against coupling-strength disorder [119]. In the case of on-site disorder, random modulation of the on-site potential may be able to restore PH symmetry [120]; in cases where this is insufficient, it is possible to characterize the energy spectrum and coupling strengths of the intermediate spin chain solely through tomography of a single end spin [121]. This characterization will help allow for the identification of a suitable, extended eigenmode.

However, the existence of an extended mode is not sufficient to ensure state transfer as disorder also enhances off-resonant tunneling rates and causes the eigenmode wavefunction amplitude to become asymmetric at the two ends of the chain. Despite such imperfections, by individually tuning the qubit-chain couplings, g_L (left) and g_R (right), it

is possible to compensate for eigenmode asymmetry; furthermore, sufficiently decreasing the magnitude of the qubit-chain coupling ensures that off-resonant tunneling can safely be neglected, even in the presence of disorder.

In addition to disorder, decoherence of the spin qubits and the intermediate spin chain places a stringent lower bound on the values of g_L and g_R, since $\tau \sim \sqrt{N}/g$. Thus, an interplay of disorder and decoherence will ultimately limit the experimental realization of FFST [44].

Chapter 5

Photon heralded entanglement between hybrid qubit systems

5.1 Introduction

There has been a rapidly growing research interest in hybrid quantum systems, which combine two or more physically different systems to harness the advantages and strengths of each systems [122], with the goal of enhancing current quantum technologies and potentially bring new applications

Generally speaking [123], macroscopic systems, such as superconducting qubits, offer great scalability and have strong coupling to external fields, but suffer from relatively fast decoherence rate. More importantly, they are usually not identical in properties like transition frequency and linewidth. On the other hand, microscopic systems, such as atoms and ions, are naturally identical and have quite long coherence time, sometimes exceeding a few seconds. The drawback of them mainly lies in slow operational speed due to weak coupling to external fields, as well as poor scalability compared to solid state devices. Several approaches of combining these two complimentary type of systems for building

hybrid quantum structure have been proposed and experimentally investigated [124–126], with main focus on superconducting qubits and circuit QED.

The key ingredient in constructing a hybrid quantum device is the generation of entanglement between two sub systems. While entanglement between identical quantum systems has been experimentally achieved in recent years, in both atomic [127] and solid state system [128–130]. Extending entanglement to disparate quantum systems, however, is much challenging, and usually requires the assistance of some forms of cavity [45, 124, 131]. For many systems, such as trapped ions and quantum dot, the integration of an optical cavity brings significant technological difficulty, and protocols that generate hybrid entanglement without the need of cavity is highly desired at this moment.

In most cases, entanglement over two well-separated identical quantum systems are mediated by photons [127–130]. But for different type of quantum systems, the photons from spontaneous emission process can have significant mismatch in spectral and temporal properties. In order to have high fidelity and high efficiency entanglement generation, the photons from different systems must have (1) nearly identical central frequency, and (2) significant overlap of pulse shape in time. The big mismatch in radiation frequency can usually be alleviated by nonlinear frequency conversion process [132], and small mismatch in frequency can be possibly tuned out through DC Stark Shift in natural or artificial atomic system [133]. This chapter intends to fulfill the requirement on pulse shape overlap. We find that by engineering input driving laser pulse shape in proper manner, the output photon pulse can be well matched for certain types of qubit system.

5.2 Waks-Monroe protocol

Before we introduce our work, we'd like to review an existing similar protocol [45] also aimed at eliminating mismatch in radiation from two different quantum systems, specifically, trapped ion and quantum dot. The protocol (named as "Waks-Monroe" protocol below) is based on remote entanglement generation method proposed in Ref. [134], which is sketched in Fig. 5.2.1. Whenever the photon detector that is placed far from both quantum systems registers a click, due to the indistinguishably of the two paths, the photon can be either from effective two-level system A or B. If the initial states of A and B are both in excited states $|1_A\rangle$ and $|1_B\rangle$, we will end up with an entangled state

$$|\psi_{AB}\rangle = \frac{1}{\sqrt{2}}(e^{i\phi_A}|0_A 1_B\rangle + e^{i\phi_B}|1_A 0_B\rangle) \tag{5.2.1}$$

However, in order for this entangled state to be the actual state we are getting, we need to make sure the two photon emission case is very rare (as the photon collection efficiency without a cavity can be very low [135], two photon emission events can often be registered as single photon click, causing errors in result). This means initially, the excited state population for both A and B

$$p = Tr(\rho_0|1_A\rangle\langle 1_A|) = Tr(\rho_0|1_B\rangle\langle 1_B|)$$

must be much smaller than 1. Therefore, the entanglement generation is **probabilistic**, with probability $p \ll 1$, which is low in efficiency.

Another drawback of this protocol is that it requires phase locking of the two optical paths between system A/B and the detector. This is because whenever ϕ_A or ϕ_B randomly

fluctuates (due to optical setup instability or motions of atoms inside the trap), the entangled state 5.2.1 decoheres and becomes non-entangled. The phase-locking technique can constitute a big challenge for many experimental setups.

Nevertheless, provided the low efficiency and hassle of phase locking, it is easy to counter the pulse shape mismatch problem, as shown by the Waks and Monroe. As we require $p \ll 1$, we can weakly excite two systems with off-resonant (Raman) lasers, this results in elastic (Rayleigh) scattering regime where the output pulse shape will simply follow the input pulse shape. Specifically, if the driving laser has a time-dependent Rabi frequency $\Omega(t) = \Omega_0 f(t)$ and detuned from the qubit transition by $\Delta \gg \Gamma_A, \Gamma_B, \Omega_0$ for both system A and B, then the emitted photon pulse shape will both follow $I(t) \propto f(t)^2$, independent of the linewidth Γ_A and Γ_B.

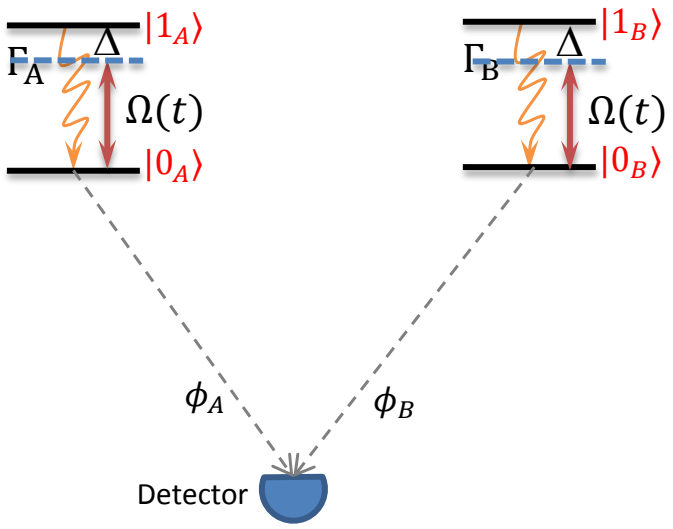

Figure 5.2.1: Schematic of a remote entanglement protocol. Two effective two-level systems with spontaneous emission rate Γ_A and Γ_B are placed far away from a photon detector. The emitted photon from system A or B that gets detected will carry an optical phase ϕ_A or ϕ_B proportional to the distance.

5.3 Our protocol

There is an improved entanglement generation protocol, based on Ref. [136], which was first implemented experimentally in Ref. [127]. This improved protocol is sketched in Fig. 5.3.1

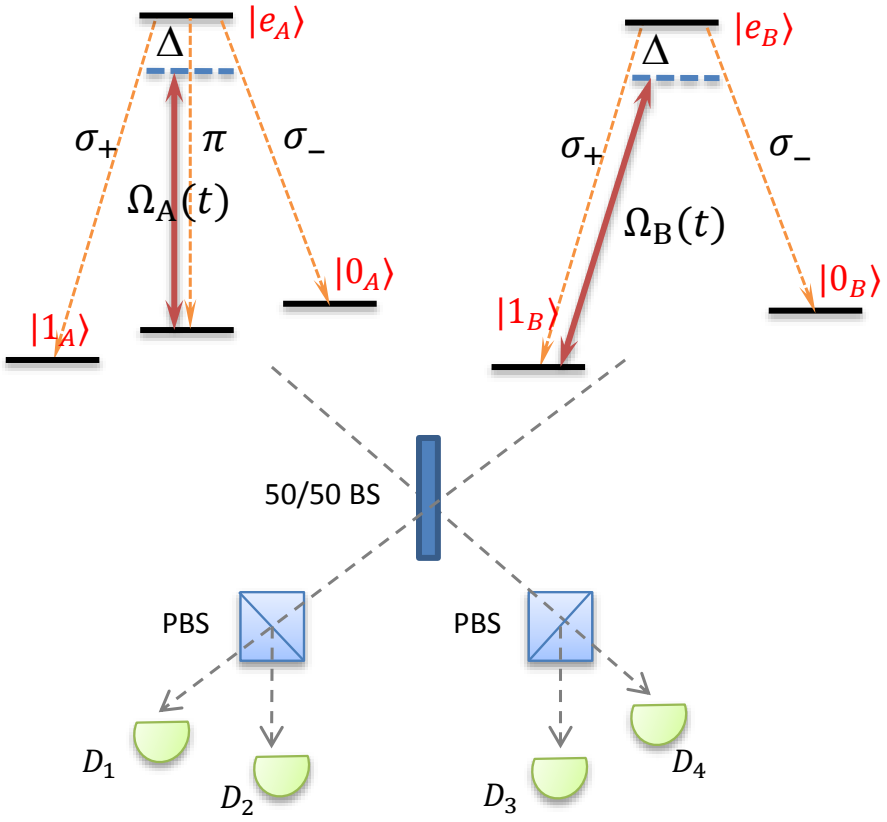

Figure 5.3.1: Schematic of an improved remote entanglement protocol. Each quantum system consists of three (Λ type, upper right) or four (tripod type, upper left) relevant energy levels, and the optical transitions give rise to different polarizations of photons, including an orthogonal pair σ_+ and σ_-. The photons emitted from both systems then pass through a Bell-type measurement setup, made of a beam splitter (BS), two polarized beam splitters (PBS), and four detectors ($D_1 - D_4$)

The key in this protocol is the existence of different polarization channels in each quan-

tum system. Such quantum system usually has either the Λ-type level structure, as found in physical systems with spin-1/2 ground state (e.g. single InAs quantum dot [137]), or a tripod-type level structure, as found in systems with spin-1 ground state (e.g. Yb^+ ions [127] and NV center in diamond [87]) If the emitted photon has different polarization, then the state for the atom or spin is also different. Based on this property, if each of the two systems emits a photon and the two photons get detected in two specific detectors in Fig. 5.3.1, one can acquire an entangled state of two qubits:

$$|\psi_{AB}\rangle = \frac{1}{\sqrt{2}}(|1_A 0_B\rangle + |0_A 1_B\rangle) \tag{5.3.1}$$

up to a global phase. The advantages of this protocol are

1. The probability of successful generation does not need to be much smaller than one. If p_A (p_B) is the probability of photon emission in each individual polarization channel, the total success probability is then $p = p_A p_B$. Assume each channel has roughly the same spontaneous emission rate (equal branching ratio), the maximum theoretical probability p is 25% for two Λ type system (Fig.5.3.1)

2. Robustness to phase fluctuation. No more phase locking is required in this protocol as the phase difference between two paths does not enter the expression of entangled state (Eq. 5.3.1). Therefore vibrations of trapped atoms/ions is also unimportant for entanglement generation.

However, if the transition linewidths of system A and B are different, it is now much harder to match them using the simple elastic scattering picture in Waks-Monroe scheme. This is because the condition $p \ll 1$ is no longer valid and the classical Rayleigh scattering approximation fails. Therefore, we need a quantum mechanical treatment for the pump-

emission process, which can be started by using the following master equation: (note that for simplicity, we focus on the Λ type level structure below, but the results can be trivially extended to tripod type system)

$$\frac{\partial \rho_{00}}{\partial t} = \Gamma \rho_{ee} \tag{5.3.2}$$

$$\frac{\partial \rho_{11}}{\partial t} = \Gamma \rho_{ee} + i(\Omega^* \rho_{e1} - \Omega \rho_{1e}) \tag{5.3.3}$$

$$\frac{\partial \rho_{e1}}{\partial t} = (i\Delta - \Gamma)\rho_{e1} + i\Omega(\rho_{11} - \rho_{ee}) \tag{5.3.4}$$

$$\rho_{ij} = \rho^*_{ji} \tag{5.3.5}$$

$$\rho_{ee} = 1 - \rho_{11} - \rho_{00} \tag{5.3.6}$$

where Γ is the spontaneous emission rate for both the σ_+ and the σ_- channel in Fig. 5.3.1, and $\Omega = \Omega_0 f(t)$ is the pumping pulse with time dependency (we've neglected any non-radiative decay here).

The emitted photon pulse intensity will follow the excited state population $\rho_{ee}(t)$. To get an analytical solution of $\rho_{ee}(t)$, we need to invoke the "adiabatic " condition, which again assumes the detuning Δ is much larger than Ω and Γ. Under adiabatic approximation, after some mathematical manipulations, we end up with the following differential equation for ρ_{ee}

$$\frac{d\rho_{ee}}{dt} = (2\frac{\dot{\Omega}}{\Omega} - \Gamma\frac{\Omega^2}{\Delta^2})\rho_{ee} \tag{5.3.7}$$

Assuming our driving pulse has a shape function $f(t/\tau)$ with characteristic width τ,

then the solution to above differential equation is

$$\rho_{ee}(t) = \frac{\Omega(t)^2}{\Delta^2} \exp[-\frac{\Gamma\Omega_0^2}{\Delta^2} \int_{-\infty}^{t} f(\frac{t'}{\tau})^2 dt'] \tag{5.3.8}$$

To give two explicit examples: an input pulse in hyperbolic secant shape $f(t) = \text{sech}(t)$ will give $\rho_{ee} \propto \text{sech}^2(t) \exp[-\frac{\tau\Gamma\Omega_0^2}{\Delta^2}(1 + \tanh\frac{t}{\tau})]$, and input pulse in Gaussian shape $f(t) = \exp(-t^2/2)$ will yield $\rho_{ee} \propto \exp[-t^2 + \frac{\tau\Gamma\Omega_0^2}{\Delta^2}\sqrt{\pi}(1 + \text{Erf}\frac{t}{\tau})]$. Thus the output pulse shape no longer follows input pulse shape, which is a striking difference from the Waks-Monroe protocol.

Fortunately, the analytical solution Eq. 5.3.8 allows us to easily match the emitted photon pulse shape $I(t) \propto \Gamma\rho_{ee}(t)$. While $\Gamma_A \neq \Gamma_B$, one can drive the two system with same input pulse shape, but with matched Rabi frequencies obeying

$$\Omega_0^A/\Omega_0^B = \Delta_A/\Delta_B\sqrt{\Gamma_B/\Gamma_A} \tag{5.3.9}$$

to make $I_A(t) = I_B(t)$. Note that we allow the detuning $\Delta_A \neq \Delta_B$ for the driving pulse, enabling a fine tune of pulse frequency in two different systems.

The probability of the emission per channel for both system A and B is given by

$$P = \frac{1}{2}\int_{-\infty}^{\infty} \Gamma\rho_{ee}dt = \begin{cases} \frac{1}{2}(1 - e^{-2\kappa}) & \text{Sech pulse} \\ \frac{1}{2}(1 - e^{-\kappa\sqrt{\pi}}) & \text{Gaussian pulse} \end{cases} \tag{5.3.10}$$

with $\kappa = \tau\Gamma_A(\Omega_0^A)^2/\Delta_A^2 = \tau\Gamma_B(\Omega_0^B)^2/\Delta_A^2$ characterizing amount of excitation. When $\kappa \gg 1$, the emission probability quickly goes to its maximum value, rendering high efficiency in entanglement generation.

The protocol we introduced here can effectively eliminate the pulse shape mismatch problem for two hybrid systems both in tripod level structure. But if one or two of the systems has the Λ-type level structure with only two optical transition channels, there is a potential problem causing imperfect entanglement: as the driving transition is now at the same one of the emission channel, there's possibility that multiple photons are emitted during the driving pulse duration (although on average still only $P < 1$ photon is emitted per channel, according to Eq. 5.3.10). If multiple photon emission happens in one system, the coincidence click on detectors does not guarantee the generation of entangled state, similar to the Waks-Monroe protocol. To make sure such event is unlikely, we have to make $P \ll 1$ again, therefore invalidating one key advantage of our protocol. Further work is still undergoing on how to maximize successful probability while perfectly matching photon pulse shape in this scenario.

Chapter 6

Temperature driven structural phase transition with trapped ions

6.1 Introduction

Ions trapped in a linear Paul trap or a planar Penning trap have become a very useful platform for quantum technologies [138], with exciting applications including quantum information science [15, 139–141] and precision measurements [142]. Trapped ions also provide a controllable system to simulate and study many-body phase transitions [27, 143, 144]. A well-known phase transition that can be observed in a small ion crystal is the structural phase transition of the Wigner crystal formed with trapped ions, which has raised significant interest and been extensively studied [145–154]. For instance, a linear crystal in a Paul trap can be squeezed to a zigzag shape with change of the aspect ratio between the transverse and the axial trapping frequencies. The structural phase transition for trapped ions so far is formulated on a classical level, determined by the mechanical equilibrium conditions. In these classical treatments that neglect quantum and thermal fluctuation of the ion positions, the structural phase transition is independent

of the system's temperature.

In this chapter, we develop a theoretical formalism to take into account quantum and thermal fluctuation in the structural phase transition, and show for the first time that a structural phase transition can be driven solely by change of the system temperature. The structural phase transition is induced by condensation of phonons into the soft mode (the lowest frequency collective oscillation mode of the ion crystal). Anharmonic coupling between different phonon modes intrinsic in the Coulomb interaction leads to renormalization of the soft mode frequency which affects the phase transition point. We calculate the system's partition function using the path integral approach, and gradually integrate out the high frequency modes with the renormalization group (RG) method to construct the RG flow for the soft mode frequency. With this formalism, we can calculate the finite-temperature phase diagram for the ion crystal. Using the linear ion crystal in a Paul trap as an example, we propose an experimental scheme to detect the predicted temperature-driven linear-to-zigzag structural phase transition and show that the requirements in observing this transition fits well with the current status of the experimental technology.

6.2 Formalism

We consider N ions of mass m subject to external harmonic potentials in both axial (z) and transverse (x, y) directions. To be concrete, we take a linear Paul trap as an example with the trapping frequencies $\omega_y > \omega_x > \omega_z$ (the method can be extended easily to other type of traps). We consider the system near the linear-to-zigzag transition point, with the ions distributed along the z direction with a tendency towards the zigzag transition in the $x - z$ plane. To describe this phase transition, it suffices to consider the ion interaction

Hamiltonian in the $x-z$ plane, given by

$$H=\sum_{i=1}^{N}\sum_{\alpha=x,z}[\frac{p_{i\alpha}^2}{2m}+\frac{1}{2}m\omega_\alpha^2\alpha_i^2]+\sum_{i>j}\frac{\kappa}{|\mathbf{r}_i-\mathbf{r}_j|}, \tag{6.2.1}$$

where κ is the Coulomb interaction rate. We assume the temperature of the system is significantly below the melting temperature of the ion crystal, which is typically of the order of $0.1-1$K [155]. This condition is satisfied straightforwardly in experiments with laser cooling. The ions have well-defined equilibrium positions $\bar{\mathbf{r}}_i$, and we expand $\mathbf{r}_i$ around the equilibrium positions up to the fourth order of the displacement operators $\delta\mathbf{r}_i\equiv\mathbf{r}_i-\bar{\mathbf{r}}_i$. Up to the second order of $\delta\mathbf{r}_i$, the quadratic part of the Hamiltonian can be diagonalized to get the normal phonon modes. For N ions in the $x-z$ plane, there are in total $2N$ normal modes, and we label them from 1 to $2N$ in the ascending order of the mode eigen-frequencies. Expressed with the coordinates of the normal modes, the Hamiltonian has the form

$$\begin{aligned} H &= \sum_{i=1}^{2N}\frac{p_i^2}{2m}+\frac{1}{2}m\omega_z^2z_0^2\Big(\sum_{i=1}^{2N}\omega_i^2q_i^2 \\ &+ \sum_{ijk}^{2N}B_{ijk}\,q_iq_jq_k+\sum_{ijkl}^{2N}C_{ijkl}\,q_iq_jq_kq_l\Big) \end{aligned} \tag{6.2.2}$$

where p_i and q_i are the canonical momentum and coordinate for the i^{th} phonon modes and ω_i denotes the corresponding eigen-frequency. We have factorized out ω_z (axial trap frequency) and $z_0\equiv(2\kappa/m\omega_z^2)^{1/3}$ (typical distance between the ions) as the frequency and the length units ($\omega_i, q_i, B_{ijk}, C_{ijkl}$ are thus all dimensionless). The terms with B_{ijk} and C_{ijkl} represent the cubic and quartic terms in the expansion of the Coulomb potential, and

we need to keep both of them as they lead to the same order of correction to the phase transition point in the following renormalization calculation. The values for ω_i, B_{ijk}, and C_{ijkl} are determined numerically through expansion of the Hamiltonian in Eq. (6.2.1) and diagonalization of its quadratic components [41]. The nonlinear interaction between phonon modes has been observed in Ref. [156], which leads to interesting collapse and revival behavior of the contrast of a Ramsey-type experiment.

The structural phase transition is caused by phonon condensation in the lowest normal mode (soft mode, or mode 1 in our notation, which corresponds to the zigzag mode for an ion chain). This happens when the effective frequency ω_{1eff} of the soft mode crosses zero. In the classical treatment [153], interaction and fluctuation of the phonon modes are neglected and the effective frequency ω_{1eff} is just given by the bare frequency ω_1 in the Hamiltonian (6.2.2). As ω_1 is determined simply through expansion and diagonalization of the trapping and the Coulomb potentials, it is apparently determined only by the mechanical conditions and has no dependence on the system's temperature. Here, we take into account the phonon interaction and derive the effective frequency ω_{1eff} through a renormalization group treatment of the partition function corresponding to the Hamiltonian (6.2.2) in the path integral formalism. As a qualitatively new result from this treatment, we show that the structural phase transition is not purely mechanical any more and becomes a thermodynamic transition depending on the system temperature.

In the path integral formalism, the partition function of the system $Z = e^{-H/(k_B T)}$ (where T is the system temperature) can be written as [157]

$$Z = \oint \prod_{i=1}^{2N} \mathcal{D}q_i e^{-S}, \tag{6.2.3}$$

where the action

$$S = \int_0^{\hbar\omega_z/(k_BT)} \frac{d\tau}{\hbar\omega_z}\frac{1}{2}m\omega_z^2 z_0^2 \left\{ \sum_{i=1}^{2N} \left[(\partial q_i/\partial\tau)^2 + \omega_i^2 q_i^2\right] + \sum_{ijk} B_{ijk}\, q_i q_j q_k + \sum_{ijkl} C_{ijkl}\, q_i q_j q_k q_l \right\}. \quad (6.2.4)$$

The RG method provides a way to work out this partition function and to find the effective frequency ω_{1eff} of the lowest mode. The basic idea of the RG method is to integrate out the high frequency modes in the path integral step by step to get a renormalized action for the lower frequency modes. We start from the highest mode $2N$, and the integration over this mode can be done in a perturbative manner with Gaussian integration over the variable $q_{2N}(\tau)$, where τ is the imaginary time in the unit of $1/\omega_z$. We define a small parameter $\epsilon = \delta z/z_0$, where the length scale $\delta z = (\hbar/m\omega_z)^{1/2}$ characterizes the ion oscillation amplitude for a single ion in a trap with frequency ω_z. We consider renormalization correction to the effective parameters up to the order of ϵ^2 (which is the order of C_{ijkl} term in the action). Following the standard procedure to calculate the path integral, we find that after integration of the mode $2N$, the action for the modes 1 to $2N-1$ still takes the form of Eq. (4) up to the order ϵ^2, with the effective parameters renormalized to

$$\begin{aligned}
\omega'_{ij} &= \omega_{ij} + \epsilon^2\left[f_1\frac{C_{i,j,2N,2N}}{2\omega_{2N}} - f_2\frac{B_{i,2N,2N}B_{j,2N,2N}}{8\omega_{2N}^3}\right] \quad (6.2.5)\\
C'_{ijkl} &= C_{ijkl} + \frac{B_{i,j,2N}B_{k,l,2N}}{4\omega_{2N}^2} + O(\epsilon^2)\\
B'_{ijk} &= B_{ijk} + O(\epsilon^2)\\
f_1 &= \coth(\frac{\hbar\omega_z\omega_{2N}}{2k_BT})\\
f_2 &= \coth(\frac{\hbar\omega_z\omega_{2N}}{2k_BT}) + \frac{\hbar\omega_z\omega_{2N}}{2k_BT}\left[\sinh(\frac{\hbar\omega_z\omega_{2N}}{2k_BT})\right]^{-2}
\end{aligned}$$

where ω_{ij} and ω'_{ij} denote the coefficients before the quadratic term $q_i q_j$ in the action ($\omega_{ij} = \omega_i^2 \delta_{ij}$ in Eq. (6.2.5)), and for the coefficients written as $C_{i,j,2N,2N}$ or $B_{i,2N,2N}$, summation over all possible permutations of the indices are implicitly assumed. After the renormalization, we re-diagonalize the quadratic term from $\sum_{ij} \omega'_{ij} q_i q_j$ to $\sum_i \omega_i'^2 q_i'^2$ and make the corresponding changes to B'_{ijk} and C'_{ijkl} through change of coordinates from q_i to q'_i. With this step, the action then takes the same form as in Eq. (4), with the mode index summarizing from 1 to $2N-1$ and the coefficients renormalized to ω'_i, B'_{ijk}, and C'_{ijkl}. Then we can continue with integration of the next highest mode until we finally integrate out all the modes except for the soft mode 1. The transformation $(\omega_i, B_{ijk}, C_{ijkl}) \to \left(\omega'_i, B'_{ijk}, C'_{ijkl}\right)$ defines the RG flow equations, and after integration of all the modes from mode N to mode 2, the last ω'_1 gives the effective frequency ω_{1eff}. By numerically solving the RG flow equations, the structural phase transition point can be determined by the criterion $\omega_{1eff} = 0$. Since the RG flow equations (see Eq. (6.2.5)) depend on the system temperature T, and so does ω_{1eff}, structural phase transition can be possibly driven solely by temperature under a fixed aspect ratio of the trap.

The temperature related functions f_1 and f_2 can be well approximated at temperature $T \gg \hbar\omega_z\omega_{2N}/k_B$ (the latter corresponds to a pretty low temperature compared to Doppler cooling limit) by:

$$f_1 \simeq \frac{2k_B}{\hbar\omega_z\omega_{2N}} T, \qquad f_2 \simeq 2f_1, \tag{6.2.6}$$

so the renormalization correction to ω_{1eff} is linear in T for a wide range of temperature. As a result, the critical exponent for temperature induced linear-to-zigzag phase transition should be 1, as long as the critical temperature is above $\hbar\omega_z\omega_{2N}/k_B$. The magnitude of the correction to ω_{ij} at each step is of the order of $k_B T/\left(m\omega_z z_0^2\right)$, which is a small quantity representing the ratio of system temperature to melting temperature. It is also

worth mentioning that even for zero temperature, the renormalization correction to ω_{1eff} is nonzero as $f_1 = f_2 = 1$ when $T = 0$, providing correction from quantum fluctuation to this structural phase transition.

6.3 Numerical calculation

In the following, we carry out some explicit numerical calculation to show that it is realistic to observe the predicted temperature driven structural phase transition in the current experimental system. In our calculation, we take 10 ions as an example with the mass of ions set as same as Yb^+ ions. The axial trap frequency is set to 100 kHz and the aspect ratio ω_x/ω_z is chosen around the classical critical value 4.59 [152]. Temperature is varied on the order from μK to mK. Fig. 6.3.1 shows the change of soft-mode frequency during the process of renormalization (the RG flow for ω_1) at different temperatures. We find that each renormalization step (integration of one normal mode) increases slightly the soft mode frequency, and the change after $2N - 1$ renormalization steps can be quite significant. The change clearly increases with the temperature, as the thermal fluctuation of the ion positions deviate the system from the classical limit where each ion is assumed fixed at its equilibrium position.

To characterize the phase transition, we calculate the order parameter, which is taken as the transverse displacement of the zigzag mode (the mean value of q_1) for the linear-to-zigzag transition. Fig. 6.3.2 shows the value of the order parameter and the corresponding phase diagram as a function of both temperature and aspect ratio. The phase boundary has a slope there, which shows that a structure phase transition can be driven vertically at a fixed aspect ratio solely by change of the system temperature. The order parameter

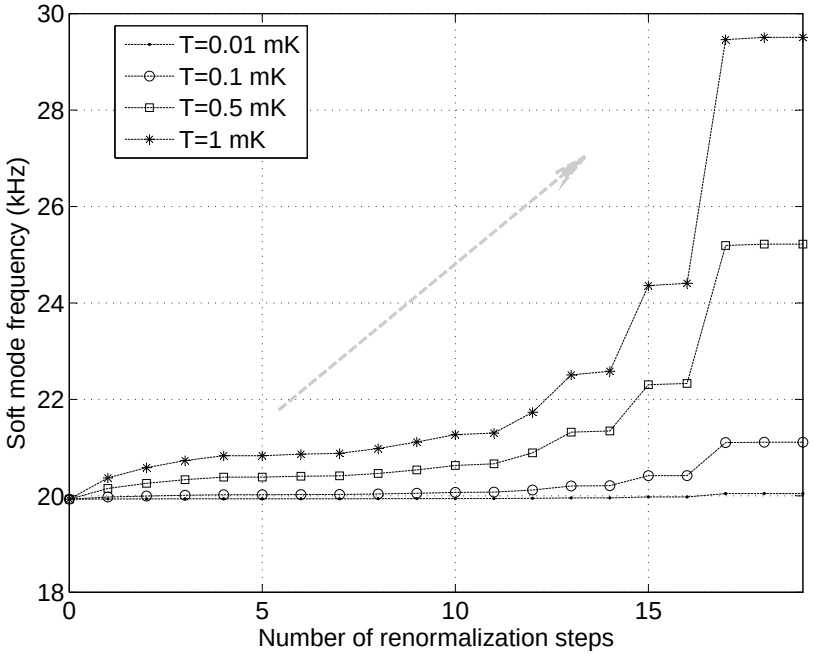

Figure 6.3.1: Change of the soft mode frequency during the renormalization process with the aspect ratio $\alpha \equiv \omega_x/\omega_z = 4.6$. Different curves correspond to different temperature, and the number of the renormalization steps represent the number of high frequency modes that have been integrated out.

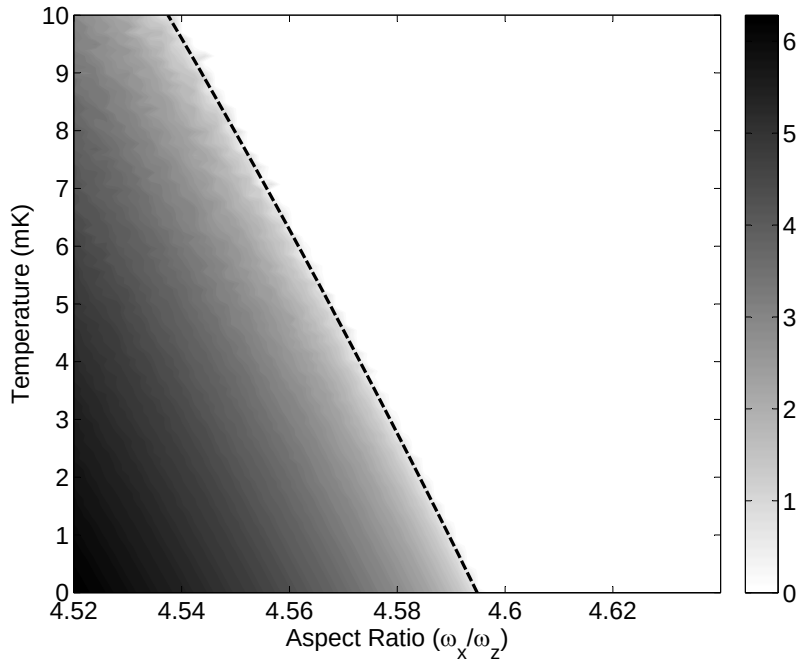

Figure 6.3.2: The map of the order parameter (with value in unit of μm) as a function of temperature and aspect ratio in the linear-to-zigzag phase transition for $N = 10$ ions. The dashed line marks the phase boundary where the order parameter crosses zero.

gradually increases from zero when one crosses the transition point, so the transition is still of the second order [153], as one expects for the symmetry breaking transition. From the figure, we also see that the order parameter is more sensitive to the aspect ratio than to the temperature. Tuning the aspect ratio by about 1% (4.59 to 4.54 for example) at a fixed temperature (around 1 mK) will result in a change of the order parameter by about 5 μm, while the same change with a fixed aspect ratio around 4.54 requires one to cool the temperature from 10 mK to 1 mK.

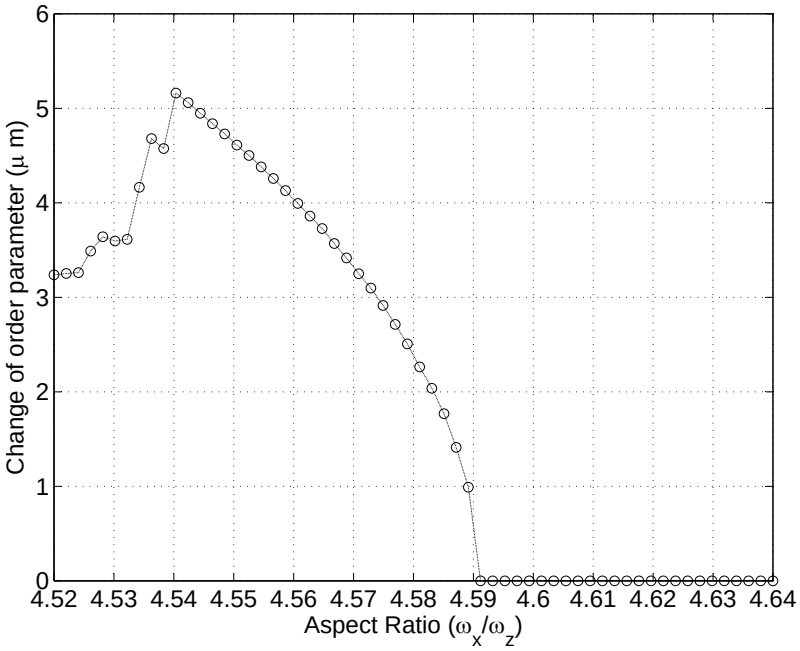

Figure 6.4.1: The change of value of the order parameter as a function of the aspect ratio when temperature is cooled from 10mK to 1mK. By tuning the aspect ratio of the confining trap to an optimum value, cooling the ions can give rise to a change of the order parameter as large as $5\mu m$, resulting in a fairly noticeable transition from linear to zigzag pattern.

6.4 Experimental detection

Experiment done in Ref. [149] has successfully observed the classical linear-to-zigzag phase transition in a trapped ion crystal by changing the radial trap frequency with an accuracy of 2 kHz (0.5% for aspect ratio). With such an accuracy (and probably better nowadays), one can pick an optimum value for aspect ratio to maximize the change of order parameter based on the numerical calculation shown in Fig. 6.4.1. The CCD camera used in Ref. [149] has a resolution of $0.3 - 1\ \mu m$, which is enough to tell the transition point as the change of order parameter is apparently larger than $1\mu m$ for a relatively wide range of aspect ratios (see Fig. 6.4.1).

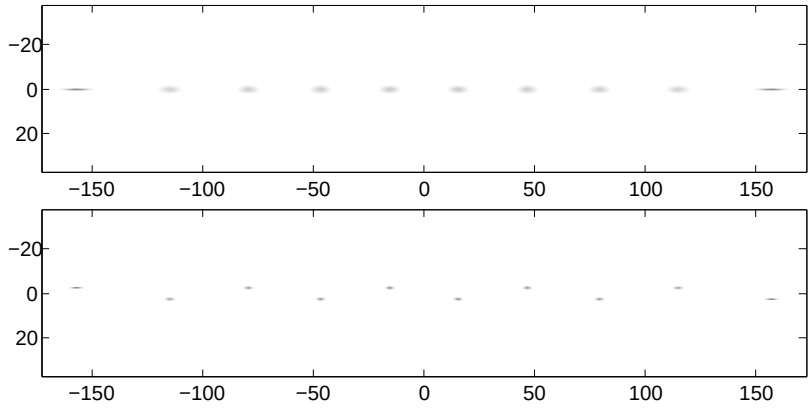

Figure 6.4.2: Plot of ions' probability density in $x - z$ plane (in unit of μm for both axes) due to thermal fluctuation. The upper figure shows the position and the probability density of 10 ions at high temperature (5mK), which characterizes the linear phase. The lower figure is simulating the ion's position after cooling the temperature to 1mK, and the zigzag pattern clearly emerges. The aspect ratio is tuned at about 4.57.

In real experiments carried out at finite temperature, the thermal fluctuation of the ions' positions will blur the image of ions. In this case, we need to calculate whether the image of ions are still sharp enough to show the temperature driven structural phase transition for the ion chain. We calculate the thermal fluctuation of ions' axial and transverse positions, and plot the probability density of the ions' wave-packets above and below the critical temperature (See Fig. 6.4.2), with the aspect ratio tuned near classical critical value. Here we only demonstrate the case with a few ions (N=10) where the transverse displacement of all ions can be roughly treated as the same as the order parameter calculated above, but our calculation method works for larger number of ions as well. Our simulation shows that one can clearly observe the structural phase transition from linear to zigzag pattern in experiment, as the thermal fluctuation of ions' transverse position in the considered temperature range is much smaller than the change of order parameter across the transition point.

Chapter 7

Space-time crystal with trapped ions

7.1 Introduction

Symmetry breaking plays profound roles in many-body physics and particle physics [158]. The spontaneous breaking of continuous spatial translation symmetry to discrete spatial translation symmetry leads to the formation of various crystals in our everyday life. Similarly, the spontaneously breaking of time translational symmetry can lead to the formation of a time crystal [48, 159]. Intuitively, if a spatially ordered system rotates persistently in the lowest energy state, the system will reproduce itself periodically in time, forming a time crystal in analog of an ordinary crystal. Such a system looks like a perpetual motion machine and may seem implausible in the first glance. On the other hand, it has been known that a superconductor [160, 161] or even a normal metal ring [162] can support persistent currents in its quantum ground state under right conditions. However, the rotating Cooper pairs or electrons in a metal are homogenous in space. Thus no spatial order is mapped into temporal order and it is not a time crystal [48]. While it has been proved mathematically that time crystals can exist in principle [48, 159], it was not clear

how to realize and observe time crystals experimentally.

In this chapter, we propose a method to create a space-time crystal (Fig. 7.1.1a), which is also a time crystal, with cold ions in a cylindrically symmetric trapping potential. Different from electrons in conventional materials, ions trapped in vacuum have strong Coulomb repulsion between each other and have internal atomic states. The strong Coulomb repulsion between ions enables the spontaneous breaking of the spatial translation symmetry, resulting in the formation of a spatial order that can be mapped into temporal order. The internal atomic states of ions can be utilized to cool the ions to the ground state as well as observing their persistent rotation directly by state-dependent fluorescence.

7.2 Formalism

We consider N identical ions of mass M and charge q in a ring trap and a uniform magnetic field B (Fig. 7.1.1b). The magnetic field is parallel to the axis of the trap. It is very weak so that it does not affect trapping. The equilibrium diameter of the ion ring is d. Figure 7.1.1c shows examples of the trapping potentials for a $^9Be^+$ ion in the radial plane of a quadrupole ring trap and a linear octupole trap, with details described in the Appendix B.

When the average kinetic energy of ions ($k_BT/2$, where k_B is the Boltzmann constant and T is the temperature) is much smaller than the typical Coulomb potential energy between ions, i.e. $T \ll Nq^2/(2\pi^2\epsilon_0 k_B d)$, the ions form a Wigner ring crystal. For ions in a ring crystal, we can expand the Coulomb potential around equilibrium positions to the second order, so the many-body Hamiltonian becomes quadratic (see the Appendix B for details). We can diagonalize the quadratic Hamiltonian by introducing a set of N

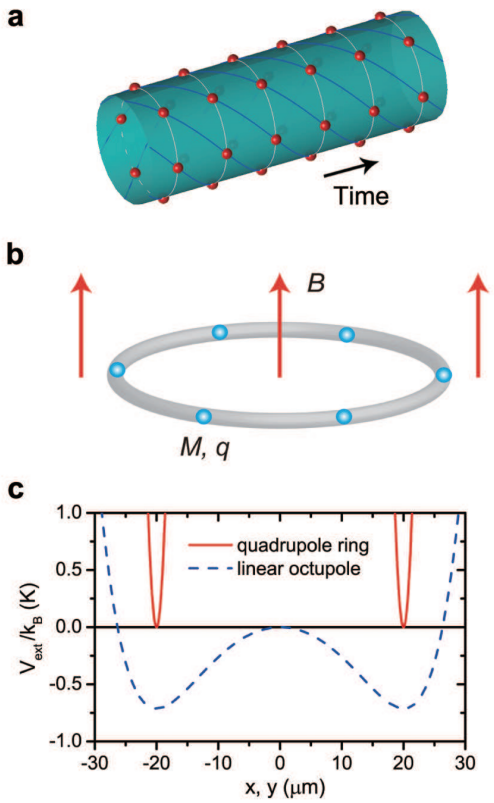

Figure 7.1.1: Schematic of creating a space-time crystal. **a**, A possible structure of a space-time crystal. It has periodic structures in both space and time. The particles rotate in one direction even at the lowest energy state. **b**, Ultracold ions confined in a ring-shaped trapping potential in a weak magnetic field. The mass and charge of each ion are M and q, respectively. The diameter of the ion ring is d, and the magnetic field is B. **c**, The pseudo-potentials (V_{ext}) for a $^9Be^+$ ion in a quadrupole ring trap (solid curve) and a linear octupole trap (dashed curve) along the x or y axis. See Appendix for details.

normal coordinates q_j and normal momenta p'_j. The normal coordinate and momentum of the collective rotation mode are $q_1 = \frac{1}{\sqrt{N}} \sum_j \theta_j$ and $p'_1 = \frac{1}{\sqrt{N}} \sum_j p_j$, respectively. The remaining $N-1$ normal coordinates correspond to relative vibration modes. Choosing the potential energy at equilibrium positions as the origin of energy, the Hamiltonian of the system becomes [163]:

$$H = \frac{2\hbar^2}{Md^2}[(-i\frac{\partial}{\partial q_1} - \sqrt{N}\alpha)^2 + \sum_{j=2}^{N}(-\frac{\partial^2}{\partial q_j^2} + \eta^2\omega_j^2 q_j^2)], \tag{7.2.1}$$

where $\hbar = h/(2\pi)$ is the reduced Planck constant, $\alpha = q\pi d^2 B/(4h)$ is the normalized magnetic flux, $\eta^2 = q^2 Md/(8\pi\hbar^2\epsilon_0)$, and ω_j is the normalized normal mode frequency.

The eigenstate of this Hamiltonian is a product state $\psi(\vec{q}) = e^{ikq_1}\prod_{j=2}^{N}\varphi_j(q_j)$, where $\varphi_j(q_j)$ ($j \geq 2$) are eigenfunctions of harmonic oscillators. Resetting the ground state energy of the relative vibrations to be the origin of energy, the energy of this state is

$$E = \frac{2\hbar^2}{Md^2}[N(\frac{k}{\sqrt{N}} - \alpha)^2 + \sum_{j=2}^{N} 2n_j\eta\omega_j], \tag{7.2.2}$$

where $n_j = 0, 1, 2, \cdots$ ($j \geq 2$) are the occupation numbers of the relative vibration modes. The wavefunction has to be symmetric with respect to the exchange of two identical bosonic ions, and has to be antisymmetric with respect to the exchange of two identical fermionic ions. If $n_j = 0$ for all $j \geq 2$, i.e. the relative vibration modes are in their ground states, the periodic boundary condition and symmetry property of the wavefunction requires $e^{ik(2\pi/\sqrt{N})} = 1$ for identical bosonic ions, and $e^{ik(2\pi/\sqrt{N})} = (-1)^{N-1}$ for identical fermionic ions. Thus for identical bosonic ions (e.g., $^9\mathrm{Be}^+$ ions), we have $k = n_1\sqrt{N}$ for all N, where $n_1 = 0, \pm 1, \pm 2, \cdots$. For identical fermionic ions (e.g., $^{24}\mathrm{Mg}^+$ ions), we have

$k = n_1\sqrt{N}$ if N is an odd number and $k = (n_1 + \frac{1}{2})\sqrt{N}$ if N is an even number. This results a qualitatively different rotation behavior for fermions and bosons that can be observed experimentally.

The lowest normalized relative vibration frequency is $\omega_2 = 2.48$ when $N = 10$ and will increases as N increases [163]. $\omega_2 \approx \sqrt{0.32N\ln(0.77N)}$ for large N. $\eta = 4.0 \times 10^4$ for $^9\mathrm{Be}^+$ ions in a $d = 10\,\mu$m ring trap. So it costs a lot of energy to excite the relative vibration modes. Thus we have $n_j = 0$ for all $j \geq 2$ at lowest energy states. For an ion ring of identical bosonic ions, the energy E_{n_1} and the angular frequency ω_{n_1} of the n_1-th eigenstate of the collective rotation mode are:

$$\begin{aligned} E_{n_1} &= E^*(n_1 - \alpha)^2 = \frac{2N\hbar^2}{Md^2}(n_1 - \alpha)^2, \\ \omega_{n_1} &= \omega^*(n_1 - \alpha) = \frac{4\hbar}{Md^2}(n_1 - \alpha), \end{aligned} \tag{7.2.3}$$

where $E^* = 2N\hbar^2/(Md^2)$ and $\omega^* = 4\hbar/(Md^2)$ are the characteristic energy and the characteristic frequency of the collective rotation, respectively. For identical fermionic ions, the results are the same as Eq. (7.2.3) if N is an odd number, and n_1 should be changed to $n_1 + \frac{1}{2}$ if N is an even number.

In classical mechanics, the angular velocity of the lowest energy state is always $\omega/\omega^* = 0$, which means that the ions do not rotate. In quantum mechanics, however, $\omega/\omega^* = 0$ is not an eigenvalue when the normalized magnetic flux α is not an integer or half of an integer. So the ions can rotate persistently even at the ground state. Since the ions are in the ground state already, there is no radiation loss due to the rotation. The rotation frequency is independent of the number of ions in the ring. The energy gap between the ground state and the first excited state is $\Delta E = N\hbar^2/(Md^2)$ when $\alpha = 1/4$. $\Delta E \to \infty$ when $N \to \infty$. Thus the persistent rotation of identical ions is a macroscopic quantum

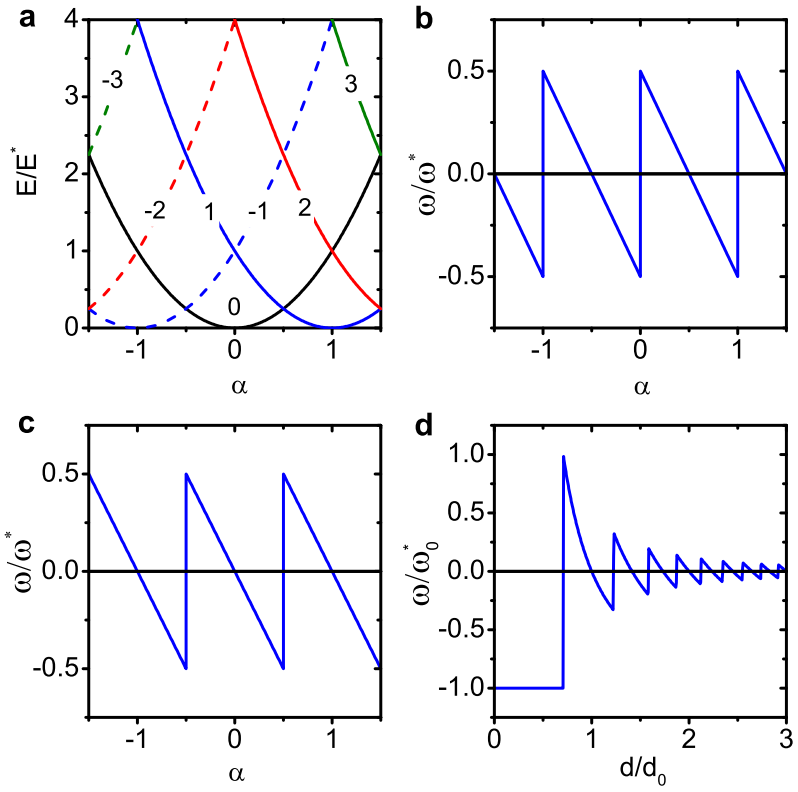

Figure 7.2.1: The rotational energy levels and frequencies of trapped ions in a ring. **a**, The energy levels of identical bosonic ions as a function of the magnetic flux α. The quantum number n_1 is labeled on each curve. The angular frequency of the persistent rotation as a function α is shown in **b** for an even number of fermionic ions, and **c** for bosonic ions. **a** and **c** are also applicable to an odd number of fermionic ions. **d**, The angular frequency of the persistent rotation of a bosonic ion ring in a constant magnetic field $B_0 > 0$ as a function of its normalized diameter d/d_0.

phenomenon and is robust for observation when N is large, which is important for a time crystal [48]. This is very different from the situation of a rigid body with mass NM and charge Nq in a ring, for which the maximum energy gap between the ground state and the first excited state is $\Delta E_{rigid} = 2\hbar^2/(NMd^2)$. $\Delta E_{rigid} \to 0$ when $N \to \infty$. When we consider a rigid body, we only minimize the energy of its center-of-mass (c.o.m.) motion. Here we minimize the total energy of the whole system, which depends on the internal interaction and the exchange symmetry of the system. If the relative vibration modes are not in their ground states, the symmetry requirement of the c.o.m motion of identical particles is relaxed and the energy gap between different c.o.m. motion states becomes smaller. The result becomes the same as that of a rigid body when all particles are different from each other.

Figure 7.2.1a shows the lowest energy levels of an ion ring consisting identical bosonic ions. When the magnetic flux satisfies $-0.5 < \alpha < 0.5$, the $n_1 = 0$ state is the ground state. As α increases above 0.5, $n_1 = 1$ state becomes the ground state. Similar things happen whenever α crosses half integer values. As a result, the angular frequency of the persistent rotation of the ground state is a periodic function of the magnetic flux (Fig. 7.2.1c). Figure 7.2.1d shows the rotation frequency of a bosonic ion ring in a constant positive magnetic field B_0 as a function of its normalized diameter d/d_0, where $d_0 = \sqrt{4h/(\pi q B_0)}$. The rotation frequency in Fig. 2d is normalized by $\omega_0^* = qB_0/2M$. The ground state is $n_1 = 0$ when $d/d_0 < 1/\sqrt{2}$. The rotation frequency is independent of the ring diameter and the number of ions in the ring for this state, and oscillates and decreases to 0 when d/d_0 increases above $1/\sqrt{2}$. If we confine many ions in a harmonic trap to form a 3D spatial crystal, ions in the crystal will rotate with the same angular frequency ω_0^* and form a 4D space-time crystal when the outer diameter of the ion crystal is smaller than $d_0/\sqrt{2}$. If we

confine ions in two concentric ring traps with diameters larger than $d_0/\sqrt{2}$, the rotation frequencies of the two rings can be different or the same, depending on the interaction between ions in different rings. When the ratio of the rotation frequencies of the two rings is an irrational number, the ions have an order in time but cannot reproduce their positions simultaneously in a finite period. Thus we have a time quasi-crystal, in analog of a conventional spatial quasi-crystal [164].

7.3 Experimental detection

The persistent rotation of trapped ions can be detected by measuring the current generated by the ions, or inferred by probing the energy levels of the ion ring. More importantly, we can observe the persistent rotation directly by measuring the ion positions twice when N is large. For example, if we have an ion ring consisting N identical $^9Be^+$ ions, we can first use a pulse of two co-propagating laser beams to change the hyperfine state of one (or a small fraction) of the ions by stimulated Raman transition and use this ion as a mark (qubit memory coherence time greater than 10 s has been demonstrated with $^9Be^+$ ions [165]). Both laser beams are parallel to the axis of the ion ring and have waists of w_0. We assume that w_0 is larger than the separation between neighboring ions and the pulse is very weak so that on average less than one ion is marked. This two-photon process localized the position of the mark ion with an uncertainty of about $\Delta x \sim w_0/\sqrt{2}$. The recoil momentum of the ion due to a stimulated Raman transition is $\vec{p}_1 - \vec{p}_2$, where $\vec{p}_1$ and $\vec{p}_2$ are the momenta of photons in the two laser beams. The amplitude of the transverse momentum of each photon in a Gaussian beam with waist of w_0 is about $\hbar/w_0$. Thus the momentum of the ion ring is changed by about $\Delta p \approx \sqrt{2}\hbar/w_0$. Δp should be smaller than the absolute value of

the initial momentum of the ion ring, which is $N\hbar/(2d)$ when α = 1/4. Thus the waists of lasers need to satisfy $2\sqrt{2}d/N < w_0 < \sqrt{2}d$ in order to localize the position of an ion without significantly alter the initial momentum of the ion ring. This condition can be fulfilled when N is large. Then we can use a global probe laser which is only scattered by the mark ion [51] (state-dependent fluorescence) to measure its angular displacement ($\Delta\theta_{mk}$) after a time separation Δt. The displacement of the mark is about $\Delta\theta_{mk} \approx \omega^*(n_1 - \alpha)\Delta t$ when N is large. The mark ion repeats its position when $\Delta t \approx 2\pi l/[\omega^*(n_1 - \alpha)]$, where l is an integer. After the measurement, we can cool the ions back to the ground state and repeat the experiment again.

To study the effects of finite temperatures on persistent rotation, we assume the trapped ions are at thermal equilibrium with temperature T. Then the average angular frequency of the ions is

$$\overline{\omega} = \sum_{n_1=-\infty}^{\infty} \frac{\omega_{n_1}}{Z} e^{-E_{n_1}/k_B T}, \tag{7.3.1}$$

where the partition function is $Z = \sum_{n_1} e^{-E_{n_1}/k_B T}$. It is convenient to define $T^* \equiv E^*/k_B = N\hbar\omega^*/2k_B$ as the characteristic temperature for the ring of ions. T^* increases when N increases.

Figure 7.3.1a shows the average rotation frequency of an ion ring consisting identical bosonic ions as a function of the temperature. At very low temperatures ($T \ll T^*$), the average rotation frequency is independent of the temperature. As the temperature increases, the probability of the ion ring occupying excited states increases. These states have positive and negative velocities alternately, which cancel each other. As a result, the amplitude of the average rotation frequency drops to zero at high temperatures ($T > T^*$). So T^* can be considered as the phase transition temperature of the space-time crystal. T^* and ω^* as a function of the diameter of an ion ring (or an electron ring) are displayed in Fig. 7.3.1b.

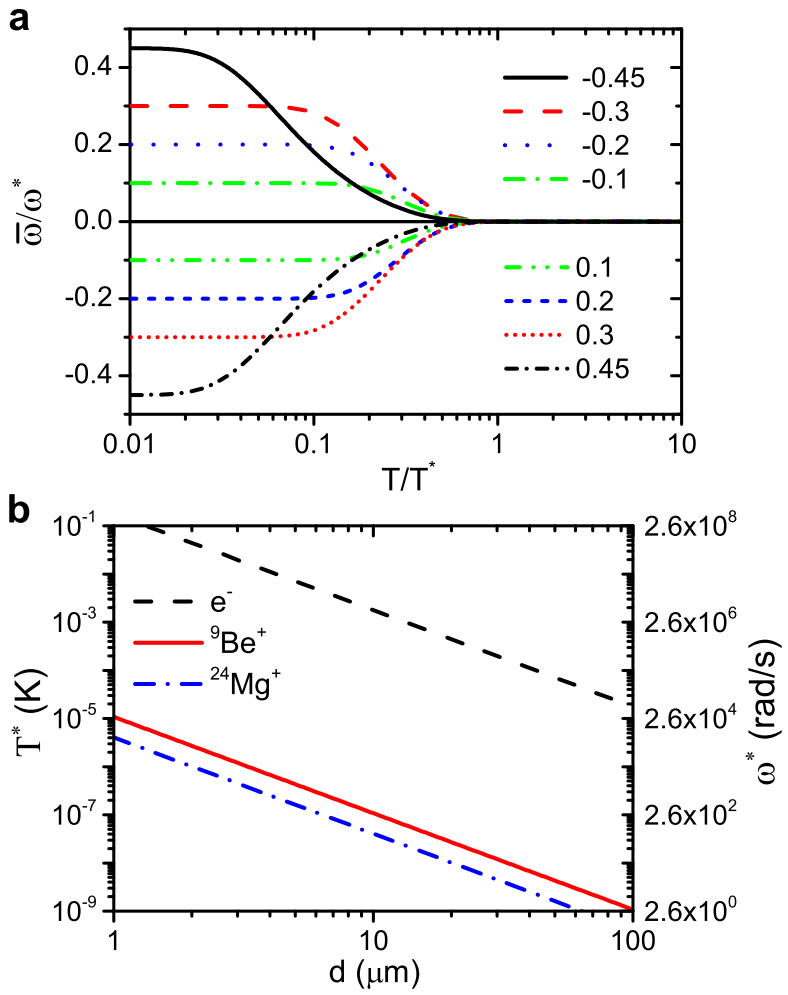

Figure 7.3.1: The temperature dependence of the persistent rotation of trapped ions. **a**, The average angular frequency of the persistent rotation of identical bosonic ions as a function of the temperature. From top down, the magnetic flux increases from -0.45 to 0.45. **b**, The characteristic temperature (left axis) and the characteristic frequency (right axis) of the persistent rotation of an ion (or electron) ring consisting 100 identical ions (or electrons) as a function of the diameter. From top down, the trapped particles are electrons, $^9Be^+$ ions, and $^{24}Mg^+$ ions.

For a $d = 100\,\mu$m ion ring consisting 100 $^9\mathrm{Be}^+$ ions, $T^* = 1.1$ nK and $\omega^* = 2.8$ rad/s. T^* is larger for smaller ion rings.

In order to experimentally realize such a space-time crystal with trapped ions, we need to confine ions tightly to have a small d, and cool the ions to a very low temperature. Recently, cylindrical ion traps with inner radius as small as 1 μm have been fabricated [166]. Simulations suggested that it is also possible to confine charged particles with a nanoscale rf trap [167]. The challenge is that ions must be cooled to below 1 μK for a microscale trap (Fig. 3b). We propose to first add a pinning potential to confine ions with MHz trapping frequencies in the circumference direction. A combination of Doppler cooling and resolved-sideband cooling can be used to cool the ions to the ground state of the MHz trap [15, 168]. The system is in the ground state of the ring-shaped trapping potential after ramping down the pinning potential adiabatically. For $T^* = 1.1$ nK, the ramping down time should be longer than 7 ms. The ultimate way of cooling ions to ultralow temperature, however, is perhaps to put the ions near a Bose-Einstein condensate of neutral atoms [169], which has been cooled to below 0.5 nK by adiabatic decompression [170].

Chapter 8

Simulation of exact spin liquid state with trapped ions

8.1 Introduction

Frustration is an important phenomenon in magnetic materials, where local spins carrying magnetic moments have competing interaction energies which cannot be minimized simultaneously. The ground state of a frustrated material usually has large degeneracy and massive entanglement, which can give rise to exotic properties of materials such as spin ice [171, 172], spin glasses [173, 174], and spin liquid [175, 176]. The properties of spin liquid have been of particular interest to researchers in recent years, due to the existence of nontrivial collective phenomena such as emergent gauge fields and fractional statistics of quasi-particle excitations [176]. In addition, it is long conjectured that spin liquid, which is microscopically a resonating-valence-bond (RVB) state, has close relationship with High-Tc superconductors [177].

Despite intense research interest, the understanding of spin liquid state is still poor due to both challenges in accurate theoretical description and lack of experimental probing methods in real frustrated materials. We're hence motivated by invoking Feynamn's

proposal on quantum simulation: if one can simulate a spin liquid model with atomic system, one will gain a much higher level of control and measurement than traditional condensed matter system. And in fact, quantum simulation of simple spin model such as Ising model has been experimentally demonstrated, both with trapped ions [51, 53, 178] and cold atoms in optical lattice [179], where magnetic frustration has already been observed due to long range spin-spin interactions in trapped-ion quantum simulator [27]. But the quantum simulation of spin liquid is currently still away from reality, due to the challenge of finding a well-understood theoretical model that at the same time, practical for experimental realization.

In this chapter, we propose a feasible approach to simulate a model with exact spin liquid ground state, known as "Haldane-Shastry" model. The model, which was proposed independently by F. Haldane and B. Shastry both in the year of 1988 [180, 181], has the exact RVB ground state as proposed by Anderson [175]. Moreover, the model is exactly solvable by analytics for full energy spectrum and wavefunctions [182], and is found to have interesting fractional statistics for quasi-particle excitations [183]. Regardless of a high level of remarkable theoretical properties, the "Haldane-Shastry" model has long been out of experimental interest, due to the peculiar inverse square range interaction in a 1D ring geometry, which does not exist in any known natural materials. Here we show that an extended version of the current trapped-ion quantum simulator can be used to simulate this model with a high level of accuracy, and meantime enabling site-to-site measurement capability in spin correlations.

This chapter is organized as follows: in section 8.2, we give a brief introduction of the "Haldane-Shastry" (HS) model and its properties. We show how to use available technology in trapped ions to simulate the model in section 8.3. Numerical calculations that

support our simulation approach is presented in section 8.4, together with discussions on future directions.

8.2 The Haldane-Shastry model

The HS model is described by the following Hamiltonian [180]

$$H_{HS} = \sum_{i<j}^{N} \frac{1}{d_{ij}^2}(S_i^x S_j^x + S_i^x S_j^x + S_i^z S_j^z) \quad d_{ij} = \frac{N}{\pi}|\sin[\pi(i-j)/N] \tag{8.2.1}$$

If one put N spins equally spaced on a ring, then distance d_{ij} represents "chord distance" between spin i and j on a ring (Fig. 8.2.1). For convenience, we can introduce complex coordinates $\{z_i\}$ for all spins with $|z_i| = 1$ (unit circle), then [184]

$$H_{HS} = (\frac{2\pi}{N})^2 \sum_{i<j}^{N} \frac{\mathbf{S_i} \cdot \mathbf{S_j}}{|z_i - z_j|^2}$$

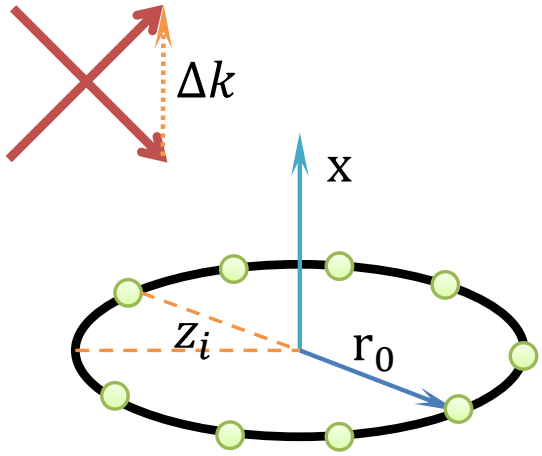

Figure 8.2.1: Haldane-Shastry model on a ring. N spin-1/2 particles form a equally-spaced lattice on a ring. To simulate the HS Hamiltonian, we add several Raman beam pairs with wave vector difference pointing in x direction (perpendicular to the ring plane)

Now we introduce the spin basis $|z_1, \cdots z_M\rangle$ to be the state vector with spins at coordinates $\{z_1, \cdots z_M\}$ pointing up (and the rest down). It is found that the ground state $|\psi_{GS}\rangle$ of H_{HS} has $M = N/2$ (total spin singlet) for any component, with the coefficient given by

$$\langle z_1, \ldots z_M|\psi_{GS}\rangle = \prod_{j<k}^{M}(z_j - z_k)^2 \prod_{j=1}^{M} z_j \tag{8.2.2}$$

The ground state wavefunction is reminiscent of the Laughlin wavefunction for $\nu = 1/2$ fractional quantum hall state [183, 185]. It is also proven to be identical to the Gutzwiller variational wave function [186] and Anderson's resonating valence bond state [177], hence it is an exact spin liquid state by definition.

Although it is hard to verify a spin liquid state by probing the wavefunction (Eq. 8.2.2), the spin correlations of $|\psi_{GS}\rangle$ has a signature decay law of $(-1)^j/j$, according to "Haldane's

conjecture" and analytic calculation in Ref. [187] for large N limit

$$\langle S_i^z S_{i+j}^z \rangle = \frac{(-1)^j}{4\pi j} \mathrm{Si}(j) \quad \mathrm{Si}(x) = \int_0^x \frac{\sin(\pi y)}{\pi y} dy \tag{8.2.3}$$

The fall-off of spin correlations shows that the ground state is disordered, which is one of the key features of spin liquid available for experimental test.

8.3 Trapped-ion Simulation

We now discuss about how to simulate H_{HS} with trapped ions. Since H_{HS} is translationally invariant on a ring, it is natural to consider ions trapped on a ring, which has been experimentally achieved [166, 188, 189]. The reader can find detailed description on how a ring trap can be constructed in Appendix B. Here we assume the ions are already trapped in a ring with translational invariance in azimuthal direction. By applying laser beams that couples ion's spin qubit transition (usually Raman beams as ion spin qubit is made of hyperfine levels) in beatnote with frequency μ and wave vector (wave vector difference for Raman beams) k in transverse direction x to all ions (see Fig. 8.2.1), we have the spin part of ion Hamiltonian (σ is the Pauli operator, and $\hbar = 1$):

$$H = \sum_i [\frac{\nu_0}{2}\sigma_z^i + (e^{i(kx_i - \nu_0 t)} + c.c.)\Omega \cos(\mu t)\sigma_x^i] \tag{8.3.1}$$

where we assume the (Raman) Rabi frequency Ω to be real and uniform on all ions. Going to interaction picture of $H_0 = \frac{\nu_{HF}}{2}\sigma_z$, and applying rotating wave approximation, we obtain

$$H_I = \sum_i \Omega \cos(\mu t)[\cos(kx_i)\sigma_x^i - \sin(kx_i)\sigma_y^i]$$

In Lamb-Dicke limit, $kx_i = \sum_m \eta_{i,m}(a_m e^{-i\omega_m t} + h.c.) \ll 1$ ($\eta_{i,m}$ is the Lamb-Dicke parameter that measures the coupling between ion i and phonon mode m, and $\{\omega_m\}$ are transverse phonon mode frequencies), then

$$\begin{aligned} H_I &\approx \Omega \cos(\mu t) \sum_i [\sigma_x^i - \sum_m \eta_{i,m}(a_m e^{-i\omega_m t} + a_m^\dagger e^{i\omega_m t})\sigma_y^x] = H_{I0} + H_{II} \\ H_{I0} &= \Omega \cos(\mu t) \sum_i \sigma_x^i \\ H_{II} &= -\Omega \cos(\mu t) \sum_i \sum_m \eta_{i,m}(a_m e^{-i\omega_m t} + a_m^\dagger e^{i\omega_m t})\sigma_y^i \end{aligned}$$

We can further go into the interaction picture of H_{I0}. Using

$$U_{I0} = \mathcal{T} \int e^{-iH_{I0}(t)/\hbar} dt = e^{i\int \Omega \cos(\mu t) \sum_i \sigma_x^i dt} = \prod_i (\cos\theta - i\sigma_x^i \sin\theta)$$

with $\theta = \frac{\Omega}{\mu}\sin(\mu t)$, we obtain

$$\begin{aligned} H_{II} &= U_{I0}^\dagger H_{II} U_{I0} \\ &= -\Omega \cos(\mu t) \sum_i \sum_m \eta_{i,m}(a_m e^{-i\omega_m t} + a_m^\dagger e^{i\omega_m t})[\cos(2\theta)\sigma_y^i - \sin(2\theta)\sigma_z^i] \\ &= -\Omega \cos(\mu t) \sum_i \sum_m \eta_{i,m}(a_m e^{-i\omega_m t} + a_m^\dagger e^{i\omega_m t})[\frac{\sigma_y^i + i\sigma_z^i}{2} e^{i2\theta} + \frac{\sigma_y^i - i\sigma_z^i}{2} e^{-i2\theta}] \end{aligned}$$

Note that

$$e^{i2\theta} = e^{i\frac{2\Omega}{\mu}\sin(\mu t)} = \sum_{n=-\infty}^{\infty} J_n(\frac{2\Omega}{\mu})e^{in\mu t}$$

In the case $\mu \gg \Omega$, the Bessel function $J_n(x) \approx (\frac{x}{2})^n/n!$ ($n \geq 0$, $J_{-n}(x) = (-1)^n J_n(x)$) decays exponentially with large n. Thus up to first order in Ω/μ:

$$e^{\pm i2\theta} \approx 1 \pm \frac{\Omega}{\mu}(e^{i\mu t} - e^{-i\mu t})$$

$$H_{II} \approx -\Omega \sum_i \sum_m \eta_{i,m} \frac{e^{i\mu t} + e^{-i\mu t}}{2}(a_m e^{-i\omega_m t} + a_m^\dagger e^{i\omega_m t})[\sigma_y^i + \sigma_z^i \frac{\Omega}{\mu}(e^{i\mu t} - e^{-i\mu t})] \quad (8.3.2)$$

In Ref. [27, 190], one chooses $\mu \approx \omega_m$, so only σ_y terms are near-resonant, and other terms will be fast oscillating ($\mu \gg \Omega$) and average out to zero. We end up with

$$H_{II} \approx -\Omega \cos(\mu t) \sum_i \sum_m \eta_{i,m}(a_m e^{-i\omega_m t} + a_m^\dagger e^{i\omega_m t})\sigma_y^i$$

The evolution operator $U = \mathcal{T}\int_0^t e^{-iH_{II}(t')dt'}$ can be expanded again using Magnus formula

$$U(t) = e^{-i\int_0^t H(t')dt' - \frac{1}{2!}\int_0^t dt' \int_0^{t'} dt''[H(t''),H(t')] - \frac{i}{3!}\int_0^t dt' \int_0^{t'} dt'' \int_0^{t''} dt'''\{[H(t'''),[H(t''),H(t')]]+[H(t'''),H(t'')],H(t')]\}+\cdots}$$

H_I itself has only linear terms like $a^\dagger\sigma_i^y$ / $a\sigma_i^y$, the first order commutator $[H(t''), H(t')]$ only has term proportional to $\sigma_i^y\sigma_j^y$, coming from the only non commuting term $[a_m, a_m^\dagger] = 1$, all higher order commutators will be zero and hence truncated. As a result, we can write

$$U(t) = \exp[i\sum_i\sum_m(\alpha_{i,m}a_m^\dagger - h.c.)\sigma_i^y + i\sum_{i,j}\beta_{i,j}\sigma_i^y\sigma_j^y]$$

Plug into Schrodinger's equation $i\frac{\partial U}{\partial \tau} = HU$ and compare coefficients, we obtain:

$$\begin{aligned}
\alpha_{i,m}(t) &= \frac{\eta_{i,m}\Omega}{\mu^2-\omega_m^2}[e^{i\omega_m t}(\mu\cos\mu t - i\omega_m\sin\mu t) - \mu] \\
\beta_{i,j}(t) &= \sum_m \frac{\eta_{i,m}\eta_{j,m}\Omega^2}{\mu^2-\omega_m^2}[\frac{\mu\sin(\mu-\omega_m)t}{\mu-\omega_m} \\
&\quad -\frac{\mu\sin(\mu+\omega_m)t}{\mu+\omega_m} + \frac{\omega_m\sin(2\mu t)}{2\mu} - \omega_m t]
\end{aligned}$$

In the off-resonant phonon excitation case, $\mu - \omega_m \gg \eta_{i,m}\Omega_i$, we have $\alpha_{i,m}(t) \approx 0$ and $\beta_{i,j}(t) \approx J_{ij}^y t$, where

$$J_{ij}^y = \sum_m \frac{\eta_{i,m}\eta_{j,m}\Omega^2\omega_m}{\mu^2-\omega_m^2} \approx \sum_m \frac{\eta_{i,m}\eta_{j,m}\Omega^2}{2(\mu-\omega_m)}$$

As $U(t) = \exp[i\sum_{i,j}J_{ij}\sigma_i^y\sigma_j^y t]$, we're simulating the effective Ising-type Hamiltonian $\sum_{i,j}J_{ij}^y\sigma_i^y\sigma_j^y$

Now if we add another beatnote with frequency $\mu_z = \mu/2$ and Rabi Ω_z, then the non-fast-oscillating terms come from σ_z terms in Eq. 8.3.2, which gives three-wave mixing $\mu_z - 2\mu_z + \mu_z$ and $-\mu_z + 2\mu_z - \mu_z$. As a result, one can show after similar calculations that there will be effective $\sigma_z^i\sigma_z^j$ interaction at

$$J_{ij}^z \approx \sum_m \frac{\eta_{i,m}\eta_{j,m}\Omega_z^2}{2(2\mu_z-\omega_m)}(\frac{\Omega_z}{\mu_z})^2$$

By choosing $\Omega_z^4 = \Omega^2\mu^2/4$, we can achieve $J_{ij}^y = J_{ij}^z$. In addition, the $\sigma_x^i\sigma_x^j$ can be

achieved by simply adding a $\pi/2$ phase to the beatnote with same Ω and μ, but along orthogonal transverse direction (assume phonon modes to be the same as $\{\omega_m\}$ so $J^x_{ij} = J^y_{ij} = J^z_{ij}$). Doing this simply swap σ_x and σ_y in all equations starting from Eq. 8.3.1. thus one ends up with the effective Hamiltonian

$$H_{eff} = J_{ij}(S^x_i S^x_j + S^x_i S^x_j + S^z_i S^z_j) \tag{8.3.3}$$

$$J_{ij} \approx \sum_m \frac{\eta_{i,m}\eta_{j,m}\Omega^2}{2(\mu - \omega_m)} \tag{8.3.4}$$

8.4 Numerical simulation and Discussion

Eq. 8.3.3 is a long-range Heisenberg model, with the coupling pattern J_{ij} determined by transverse phonon mode structure and beatnote frequency μ. Now we show that by properly tuning μ and transverse phonon mode structure (through changing trap frequency aspect ratio), J_{ij} will match the inverse-range interaction in HS model very well.

As an example, we perform a numerical simulation with $N = 20$ Yb^+ ions trapped in a ring with diameter $r_0 = 125\mu m$. The transverse confining potential is set to $\omega_x = 5$MHz, and beatnote frequency $\mu = \omega_x + 319$KHz. In Fig. 8.4.1, we show that the simulated J_{ij} (Eq. 8.3.4) matches reasonably well with that in the exact Haldane-Shastry model (Eq. 8.2.1). More importantly, we find that the spin correlations $\langle \sigma^x_i \sigma^x_{i+j} \rangle$ agrees extremely well with the numerical calculation from exact ground state of HS Hamiltonian, and consistent with the power law decay in analytical expression (Eq.8.2.3)

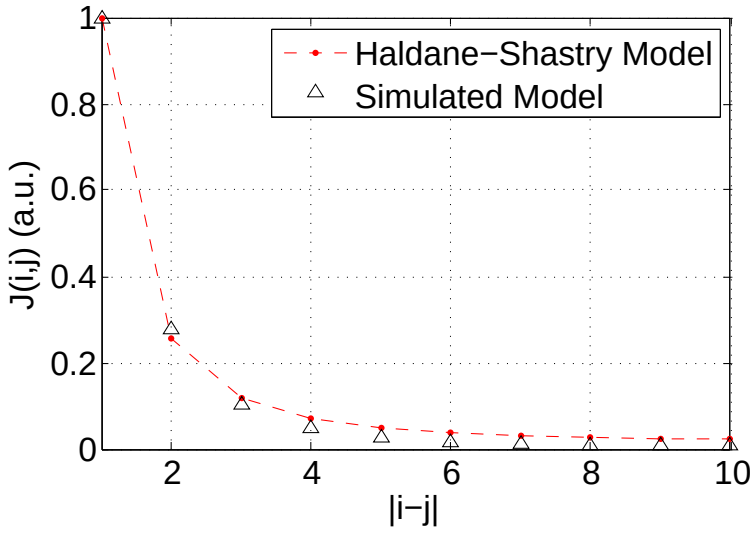

Figure 8.4.1: Comparison of J_{ij} between HS and simulated model. The simulated J_{ij} using trapped ions (black triangle) matches reasonably well with the Haldane-Shastry model $J_{ij} \propto 1/\sin^2[\pi(i-j)/N]$ (dash line and red dot).

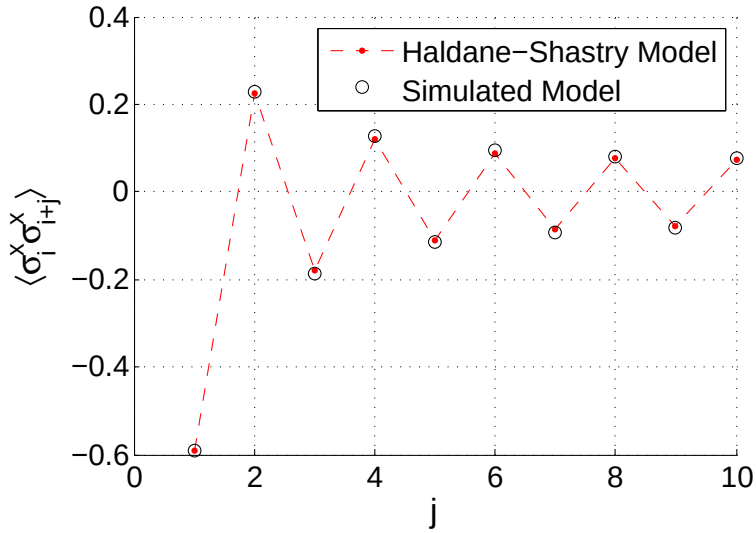

Figure 8.4.2: Comparison of spin correlation between HS and simulated model. The simulated Hamiltonian with trapped ions (black circle) gives almost the same spin correlation power law decay (see Eq. 8.2.3) as the exact Haldane-Shastry model (dash line and red dot).

The ground state of the simulated HS Hamiltonian can be prepared using adiabatic passage [27]: we first add a magnetic field in x direction (by using carrier transition beams) that is much larger than any J_{ij}, then we initialize all ions to $\sigma_x^i = -1$ state, so the system is approximately in the ground state of current spin Hamiltonian. Afterward, we adiabatically ramp down the transverse magnetic field to zero, and the system will stay in ground state of the simulated HS model. Note that the ramping speed depends on the energy gap of the HS Hamiltonian, which is proportional to $1/N$ [182], requiring only a linear increase of simulation time or laser power, so a relatively large size of the HS model can be simulated in the future.

The spin correlations $\langle \sigma_i^x \sigma_{i+j}^x \rangle$ (or $\langle \sigma_i^y \sigma_{i+j}^y \rangle$ and $\langle \sigma_i^z \sigma_{i+j}^z \rangle$) can be readily measured in experiment using state-dependent fluorescence, as already carried out in Ref. [52]. The signature decay pattern (Fig.8.4.2) will serve as a key evidence of the existence of spin liquid state. But we'd like to point out that the HS model has many more interesting features than the power-law decay of spin correlations. An incomplete list of these features are fractional spinon statistics [183], high degeneracy in energy spectrum due to Yangian symmetry [191], and non-trivial properties in entanglement entropy [192]. We're currently on the way of searching methods to experimentally study these features based on the proposed trapped-ion simulator.

Chapter 9

Prethermalization in isolated trapped ion chain

9.1 Introduction

The dynamical properties of isolated quantum many-body systems have been under intense interest in recent years [193, 194]. On the theory side, the research has been centered on whether and how isolated quantum system approaches thermal equilibrium. While certain observables are found to relax to equilibrium in some large systems [195–199], it remains unclear on what time scale equilibration occurs in generic systems [200–203]. On the experimental side, recent progress with cold atoms [204–206] and trapped ions [27, 51–53] has made it possible to simulate well controllable simple models, such as 1D Bose gas and transverse field Ising model. These quantum systems can be well isolated from environmental bath and have long coherence time, while their physical properties can be measured at individual atomic level, providing an unprecedented opportunity for studying non-equilibrium dynamics in closed interacting systems.

A particular intriguing phenomenon in this context is called *prethermalization* [207], which has been shown to emerge in various theoretical setups [208–210], and experi-

mentally observed in cold atomic gas [206, 211]. The emergence of prethermalization is characterized by an establishment of quasi-stationary state at intermediate time scale, and followed by relaxation to stationary state at long time scale. Physical origin of prethermalization, however, is still elusive, and is primarily speculated to be related to integrability of model, where the prethermal state can sometimes be characterized by a Generalized Gibbs Ensemble (GGE) coming from the integrable approximation of a non-integrable model [206, 209]. However, it was shown recently that even for exact integrable system, prethermalization can still occur, and the prethermal state can not be described accurately by GGE [210].

In this chapter, we propose an experimental method to observe and study a new type of prethermalization in a XY spin model, using currently available trapped-ion quantum simulator [52]. Here the emergence of prethermalization is due to the combination of inhomogeneous lattice spacing and long range spin-spin interaction. Unlike many other systems, the prethermalization can occur for as few as $N = 16$ spins, and survive for N as large as a few thousand (limited only by numerical computation power), allowing for easy experimental realization. In particular, the prethermal state in our system cannot be described by GGE, but can be well described by a *partial diagonal ensemble* (PDE). By examining the energy spectrum of our system in a small dimension subspace, we find a non-trivial structure of near-degenerate eigenstate pairs in the lower half energy spectrum, which is confirmed to be responsible for the occurrence of prethermalization. In addition, by tuning the range of interaction in an experimentally straightforward way, we find the dynamical behavior of system to exhibit three different phases: thermalization only, prethermalization followed by thermalization, and prethermalization only. The transition between different phases becomes sharper and sharper with increased number of

spins, hinting the existence of dynamical phase transition [212]. Our method provides a new way of investigating prethermalization and related dynamical properties in models irrelevant of integrability.

9.2 Model of system

Our model comes from the quantum simulator made of a 1D chain of ions trapped in a linear Paul trap (9.2.1), which has been described in details in section 8.3 of the previous chapter. Through proper configuration of laser beams, the optical dipole force can generate an effective transverse field Ising model [27, 51, 52]:

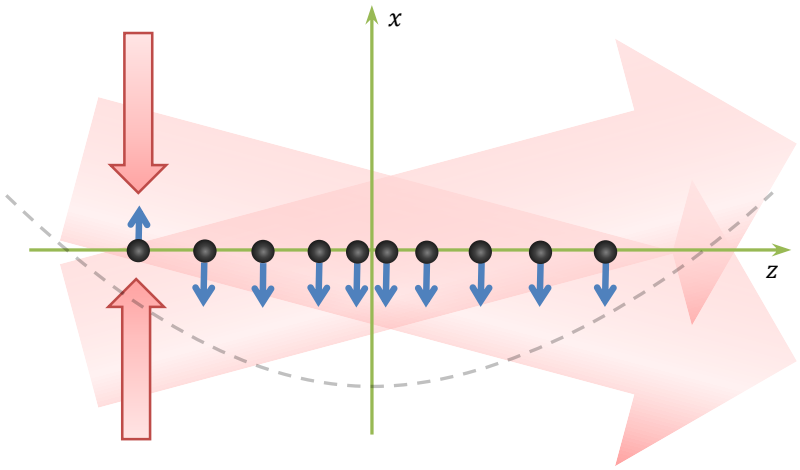

Figure 9.2.1: Schematic of the proposed experimental setup: A chain of N ions are trapped along the z direction in a 1D harmonic linear Paul trap, with inhomogeneous lattice spacing. The global (Raman) laser beams generate spin-dependent force along x direction, resulting in effective Ising-type interaction. A focused laser beam is applied on one end of the ion chain to selected flip only the first spin on demand.

$$H = \sum_{i<j}^{N} J_{i,j}\sigma_i^x\sigma_j^x + B\sum_{i=1}^{N}\sigma_i^z \tag{9.2.1}$$

here σ_i is the spin-1/2 Pauli matrix for the i^{th} ion qubit, and the interaction pattern J_{ij} is given by

$$J_{i,j} = \Omega^2 \sum_{m=1}^{N} \frac{\eta_{i,m}\eta_{j,m}\omega_m}{\mu^2 - \omega_m^2}$$

where μ is the Raman beatnote frequency, and Ω is the effective Raman Rabi frequency, which is assumed uniform on all ions. $\{\omega_m\}$ are the phonon mode frequencies of ions in x direction ($\omega_1 < \omega_2 < \ldots \omega_N = \omega_x$), and $\eta_{i,m}$ is the Lamb-Dicke parameters measuring the coupling between ion i and phonon mode m.

It is experimentally possible to make the effective transverse magnetic field B much larger than J_{ij} [51]. In this limit, the $\sigma_i^+\sigma_j^+$ and $\sigma_i^-\sigma_j^-$ terms in Eq. 9.2.1 will be energetically forbidden, and one ends up with the XY Hamiltonian:

$$H \approx H_{XY} = \sum_{i<j} 2J_{i,j}(\sigma_i^+\sigma_j^- + h.c.) + B\sum_i \sigma_i^z \tag{9.2.2}$$

The key feature of the simulated Hamiltonian (9.2.1 & 9.2.2) is that J_{ij} is long-ranged. Moreover, the range of interaction can be tuned easily by changing the beatnote frequency μ. The two extreme cases are (1) $\mu - \omega_x \to 0$, where $J_{ij} \to$constant and (2) $\mu - \omega_x \to \infty$, where $J_{ij} \sim 1/|i-j|^3$. For generic μ, J_{ij} can be approximated with an inverse power-law decay interaction:

$$J_{ij} \sim \frac{1}{|i-j|^\alpha} \tag{9.2.3}$$

where $\alpha \in (0, 3)$, but its realistic value should be determined by trap frequencies, maximum laser power and spin decoherence time.

The $1/r^\alpha$ Ising model (Eq. 9.2.1) with zero transverse field (essentially classical) can be analytically solved [213, 214], and its dynamical property has also been recently studied [210, 215], where it is found that if α is smaller than the dimensionality of the system, the total interaction energy per site will diverge, drastically changing the dynamics after a quantum quench. However, there is no known analytic solution for $1/r^\alpha$ XY model (Eq. 9.2.2), and numerical calculation of its dynamics would require a full diagonalization of the $2^N \times 2^N$ matrix, which is intractable even for an experimentally achievable small number of ions (e.g. $N = 16$ as in [52])

For large α, it may be possible to approximate H_{XY} by only keeping the nearest-neighbor interaction $J_{i,i+1}$. In this case, a Jordan-Wigner transformation yields the integrable fermionic Hamiltonian

$$H_{int} = 2\sum_i (J_{i,i+1} c_i^\dagger c_{i+1} + B c_i^\dagger c_i) \tag{9.2.4}$$

We note that both the Hamiltonian 9.2.2 and 9.2.4 conserves the total spin excitation $n = \sum_i c_i^\dagger c_i = \sum_i \frac{\sigma_i^z + 1}{2}$, thus the Hamiltonian is block-diagonal in different n subspaces. If our initial state lies in one of the subspace, then the subsequent dynamics is also constrained in the same subspace, which can significantly speeds up numerical calculation of system dynamics when the subspace dimension is significantly smaller than the total Hilbert space.

We'll first initialize all the spin qubits carried by ions to spin down state ($\sigma_i^z = -1$) [1]. This initial state is the eigenstate of H_{XY} and thus stationary. We then start the non-equilibrium dynamics by using focused laser beam that only flips the first spin (left end

[1] For ion qubit with hyperfine clock state, this can be done by first prepare prepare all hyperfine spin qubits to $\sigma_i^y = -1$ (where y is the quantization axis), then followed by a coherent $\pi/2$ rotation around x axis to prepare an initial state with $\sigma_i^z = -1$.

ion) to $\sigma_i^z = 1$, the resulting state

$$|\psi(0)\rangle = |\uparrow\downarrow\downarrow\cdots\downarrow\rangle$$

is no longer the eigenstate of the original H_{XY} and is subject to unitary dynamics in $n = 1$ (single spin excitation) subspace. This subspace has dimension $N \times N$, allowing for efficient numerical calculation up to $N \sim 10^3$ ions on classical computer.

For experimental interest, we consider the time evolution of local observables $\langle\sigma_i^z(t)\}$, and their correlations $\langle\sigma_i^z(t)\sigma_j^z(t)\rangle$, both of which can be easily measured at different time [52] for all ions. In addition, we define the operator

$$C = \sum_{i=1}^{N} f_i \frac{\sigma_i^z + 1}{2}$$

where the coefficient $f_i \equiv (i - \frac{N+1}{2})/(N-1)$ is equally distributed between $[-1, 1]$ from $i = 1$ to $i = N$. The expectation value of C takes value between $[-1, 1]$ and physically measures the relative position of the "spin excitation center". It's easy to check that $\langle\psi(0)|C|\psi(0)\rangle = 0$, and for any state that has spatial inversion symmetry around the center of the chain, $\langle C\rangle = 0$. We'll show that the $\langle C\rangle$ acts as an "order parameter" that characterizes the dynamics of the system from the above non-equilibrium initial state.

9.3 Numerical results

We start our numerical calculation by first investigating an experimentally testable $N = 16$ ion chain, and especially, we're interested in comparing dynamics between short range and long range interaction pattern. The practical values of α for both cases, together with

corresponding other experimental parameters are listed in Table 9.1. The generated J_{ij} pattern are plotted in Fig. 9.3.1

$N = 16$	α	ω_z	ω_x	$\mu - \omega_x$	$\eta_x\Omega$	$\overline{J}$
Short-range	2.6	100KHz	5MHz	200KHz	40KHz	20Hz
Long-range	0.52	600KHz	5MHz	20KHz	3.9KHz	20Hz

Table 9.1: Experimental parameters used for simulations in Fig. 9.2.1-9.3.4, which can be achieved with current trapped-ion quantum simulation technology (Ref. [51, 52]). $\eta_x = \sqrt{\frac{\hbar(\delta k)^2}{2M\omega_x}}$, $\overline{J} = \sum_{i\neq j} J_{ij}/N^2$

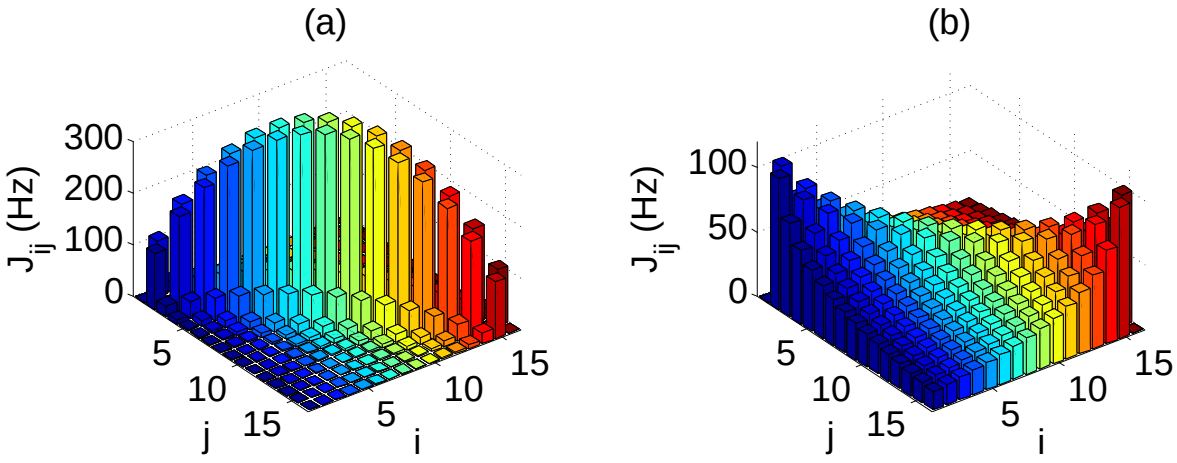

Figure 9.3.1: J_{ij} in Hamiltonian 9.2.1 & 9.2.2 using parameters in Table 9.1. (a) Short range interaction (b) Long range interaction.

The short time dynamics (a few $1/\overline{J}$) of all $\langle\sigma_i^z\rangle$ and $\langle C\rangle$ are shown in Fig. 9.3.2. In the short-range interaction case, one sees that the spin excitation ,initially located at left end of the chain, somewhat coherently travels to the other end and oscillates back and forth with small dispersion. In contrast, the spin excitation diffuses to the rest of the chain slowly in the long interaction case and somehow get locked before it reaches the middle of the chain. ($\langle C\rangle \approx -0.4$).

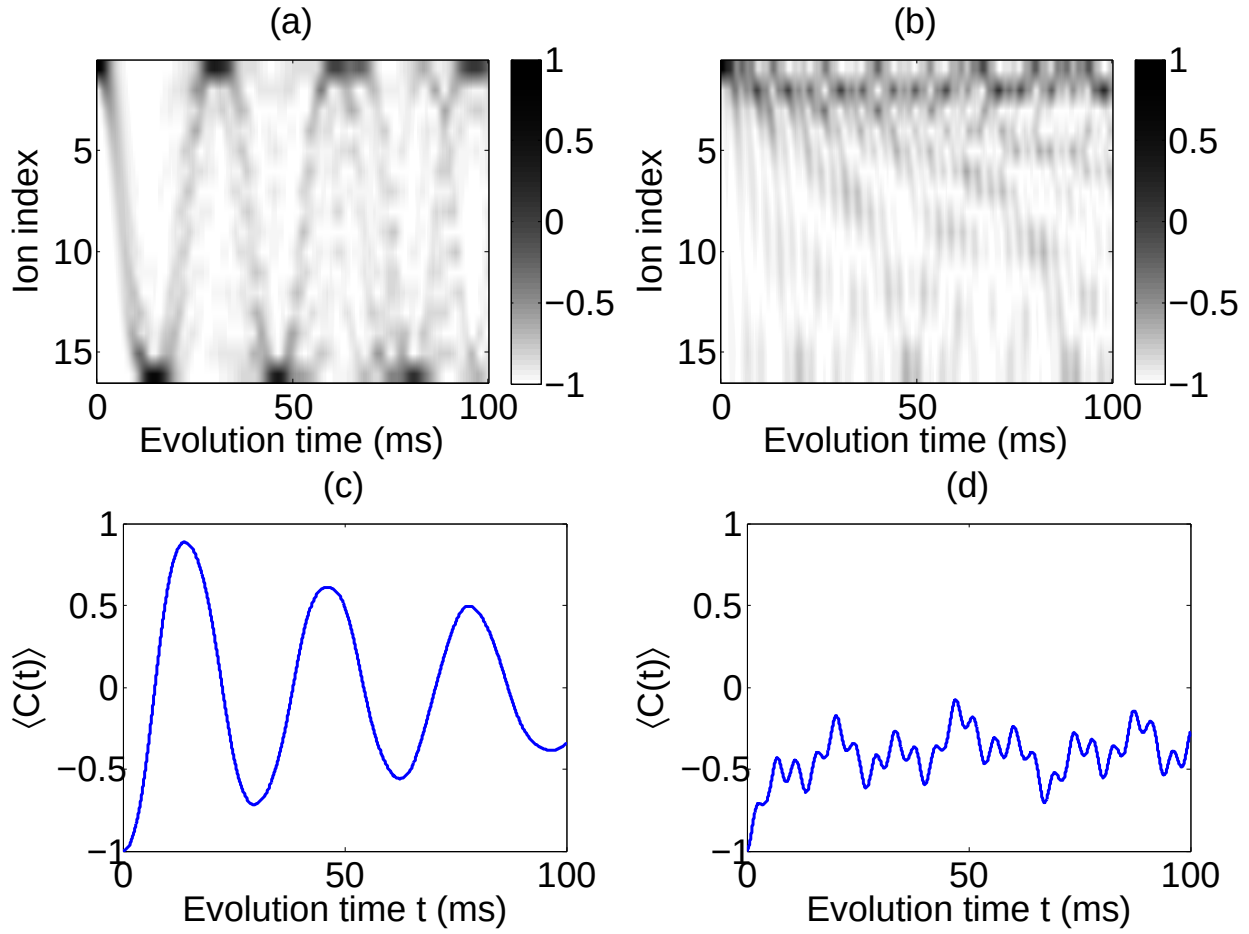

Figure 9.3.2: Short time dynamics of $\langle \sigma_i^z(t) \rangle / \langle C(t) \rangle$ for short range (a)/(c) and long range (b)/(d) interaction.

To better present the long time dynamics, we performed a finite time average on all observables

$$\overline{A(t)} \equiv \frac{1}{t} \int_0^t \langle A(\tau) \rangle d\tau$$

to remove fast temporal fluctuations on shorter time scale [2]. From Fig. 9.3.3a, we find that in short-range interaction case, $\overline{\sigma_i^z}$ and $\overline{C}$, as well spin correlations $\overline{\sigma_i^z \sigma_j^z}$, will quickly relax

[2] In certain system with large N, this time averaging procedure is not necessary, as $\langle A(t) \rangle$ converges to $\overline{A(t)}$ after long enough time [197, 198]. In the example considered here, the number of particles is rather small and the operators in interest do not converge well.

to the stationary values at around $T \sim 10/\overline{J}$, and these values coincide (Fig. 9.3.3c) with the "thermal" values [3] predicted by diagonal ensemble (DE). In the long-range interaction case (Fig. 9.3.3b), all these operators first reach "prethermal" quasi-stationary values at time scale T, and further relax to the stationary thermal values at much longer time scale ($10^4 T$).

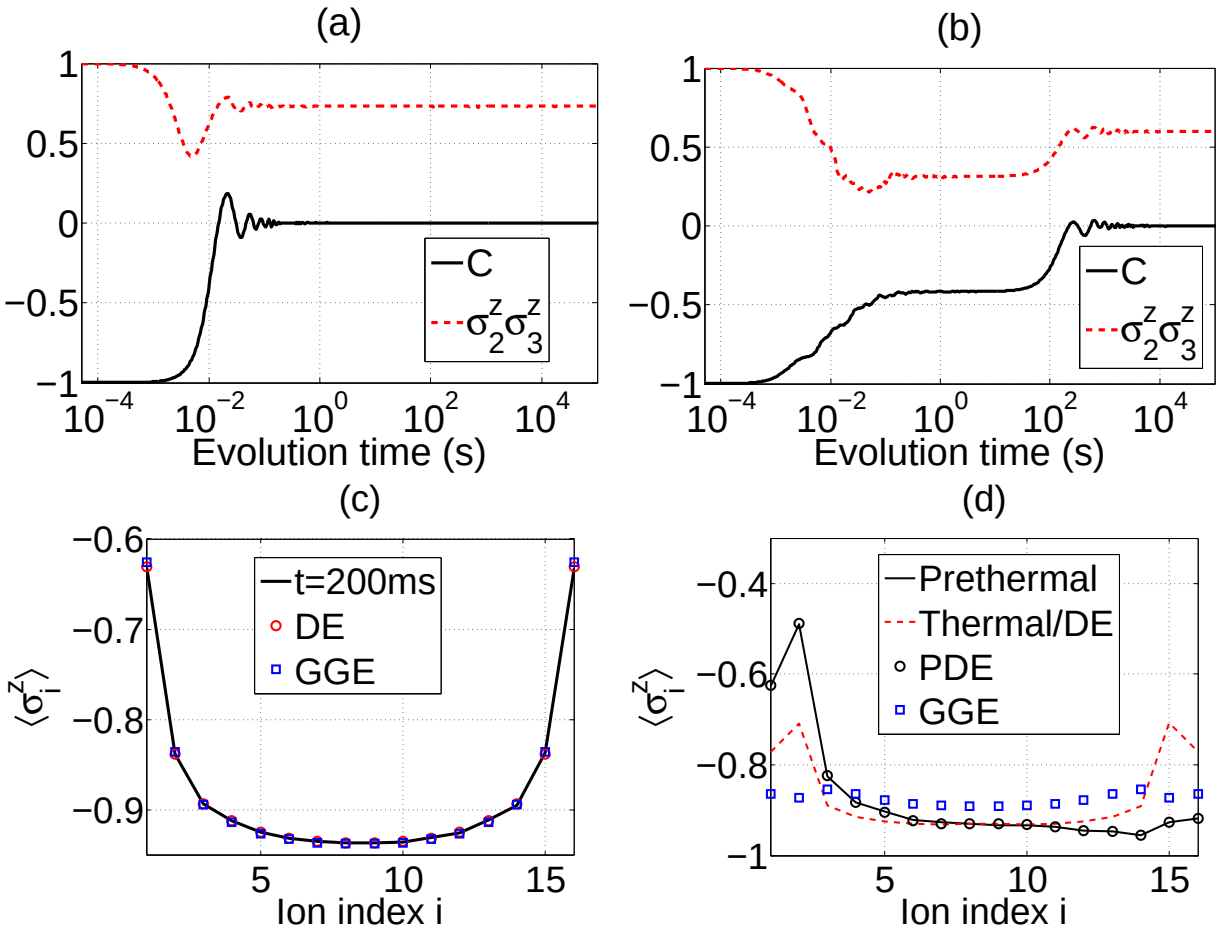

Figure 9.3.3: (a)-(b): Full time dynamics of $\overline{C}$, $\overline{\sigma_i^z}$ and $\overline{\sigma_i^z\sigma_j^z}$ for (a) short range and (b) long range interaction. (c) The stationary value of $\overline{\sigma_i^z}$ at $t \approx 10/\overline{J} = 200$ms matches well with both DE and GGE prediction for short range interaction. (d) The prethermal value of $\overline{\sigma_i^z}$ does not match with either GGE or DE, but agrees with PDE (see main text).

[3] "Thermal" value here means exclusively the value predicted by diagonal ensemble. This should not be confused with the thermal values predicted by Gibbs (canonical) ensemble in non-integrable system.

Fig. 9.3.3d shows that the "prethermal" state features an interesting asymmetric spin configuration, which suggests the use of our "order parameter" C, since the emergence of prethermalization is manifested in a nonzero value of $\overline{C}$ at intermediate time scale T. We find that the prethermalization only happens when the index α is smaller than a critical value ($\alpha_C \approx 1.3$ for $N = 16$). For larger system size (up to $N = 1024$), the prethermalization-thermalization transition still occurs, but α_C becomes smaller and the transition becomes sharper, indicating the existence of a dynamical phase transition [212, 216–218]

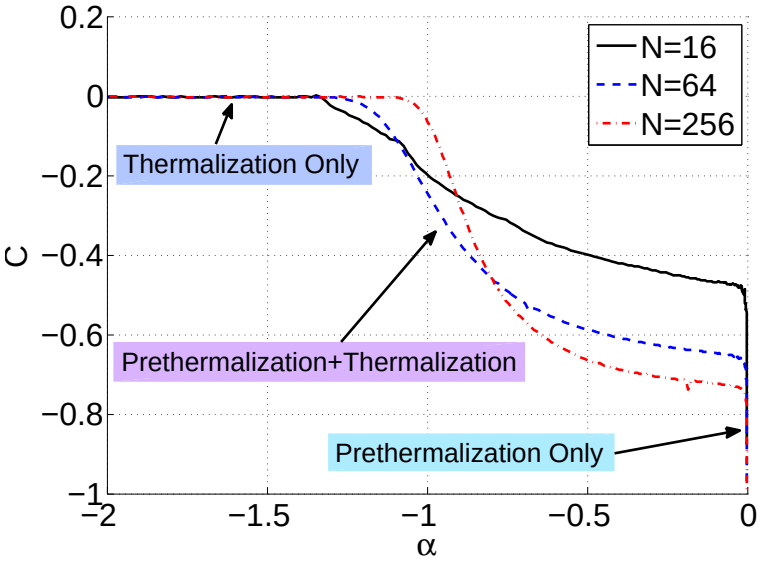

Figure 9.3.4: A dynamical "phase diagram" with regard to index α. The $N = 16$ case uses the parameters in Table 9.1 (long range row) and $N = 64, 256$ cases use a scaled down $\omega_z \propto \sqrt{\ln N}/N$ to maintain chain stability.

9.4 Discussion

We'll now give physical explanations to the above numerical results: The distinctive dynamics of $\langle \sigma_i^z(t) \rangle$ in Fig. 9.3.2 can be explained by examining the energy spectrum of H_{XY} in $n = 1$ subspace (shown in Fig. 9.4.1a). In the short-range interaction case, the energy spectrum is close to linear. This is because H_{XY} can be approximated by H_{int} (Eq. 9.2.4), whee only nearest-neighbor J_{ij} terms are kept. H_{int} is close to a "quantum mirror" Hamiltonian [44, 219], resulting in a near dispersion-less spin wave propagation until non-linearity sets in. The stationary values of $\overline{\sigma_i^z}$ can also be well predicted by GGE (based on conserved fermionic quasi-momentum in H_{int}), as shown in Fig. 9.3.3c. On the other hand, the energy spectrum of long range interaction case is highly non-linear, so the dynamics of spin excitation is highly dispersive.

The existence of prethermal stage in the time evolution, however, is much more non-trivial. Naively, the spin flip-flop matrix J_{ij} varies smoothly among sites for any $\alpha \in (0, 3)$, so the spin excitation should continuously diffuse from one end of the chain to the whole chain, and is not expected to get trapped somewhere in the middle for a long time. The two stage dynamics indicates that there are two different time scales weaved in the Hamiltonian, which is not at all obvious by looking at J_{ij}. Instead, since the time dynamics of any physical observable is simply given by

$$\langle A(t) \rangle = \sum_{m,n} \rho_{mn}(0) A_{nm} e^{i(E_m - E_n)t/\hbar}$$

, different time scales of dynamics can be unraveled through mapping of eigenenergy differences $\{E_m - E_n\}$, as done in Fig. 9.4.1. In the short-range interaction case (Fig. 9.4.1b), all $\{E_m - E_n\}$ are continuously distributed from $\overline{J}$ to $100\overline{J}$, so a single-stage

relaxation is expected after $T \sim 10/\overline{J}$. In the long-range interaction case (Fig. 9.4.1c), although most $\{E_m - E_n\}$ still fall into the range of $1 - 100\overline{J}$, there is strikingly a separate branch gapped at much lower rate ($\sim 10^{-6}\overline{J}$). This branch actually corresponds to near-degenerate pairs ($\{E_{2k} - E_{2k-1}\}$) of eigenenergy (Fig. 9.4.1a) that make up the first half energy spectrum, and the number of these pairs scale up with system size N.

This key feature in energy spectrum, is not merely caused by long range interaction. If we put the ions into a ring trap to make the ions equally spaced, then even with same long range interaction, there is no separate branch in $\{E_m - E_n\}$ (Fig. 9.4.1d), hence we also find no prethermalization behavior in such case. As a result, we contribute the cause of prethermalization here to be a *combined effect* of long range interaction and inhomogeneous lattice spacing (due to harmonic axial trapping potential).

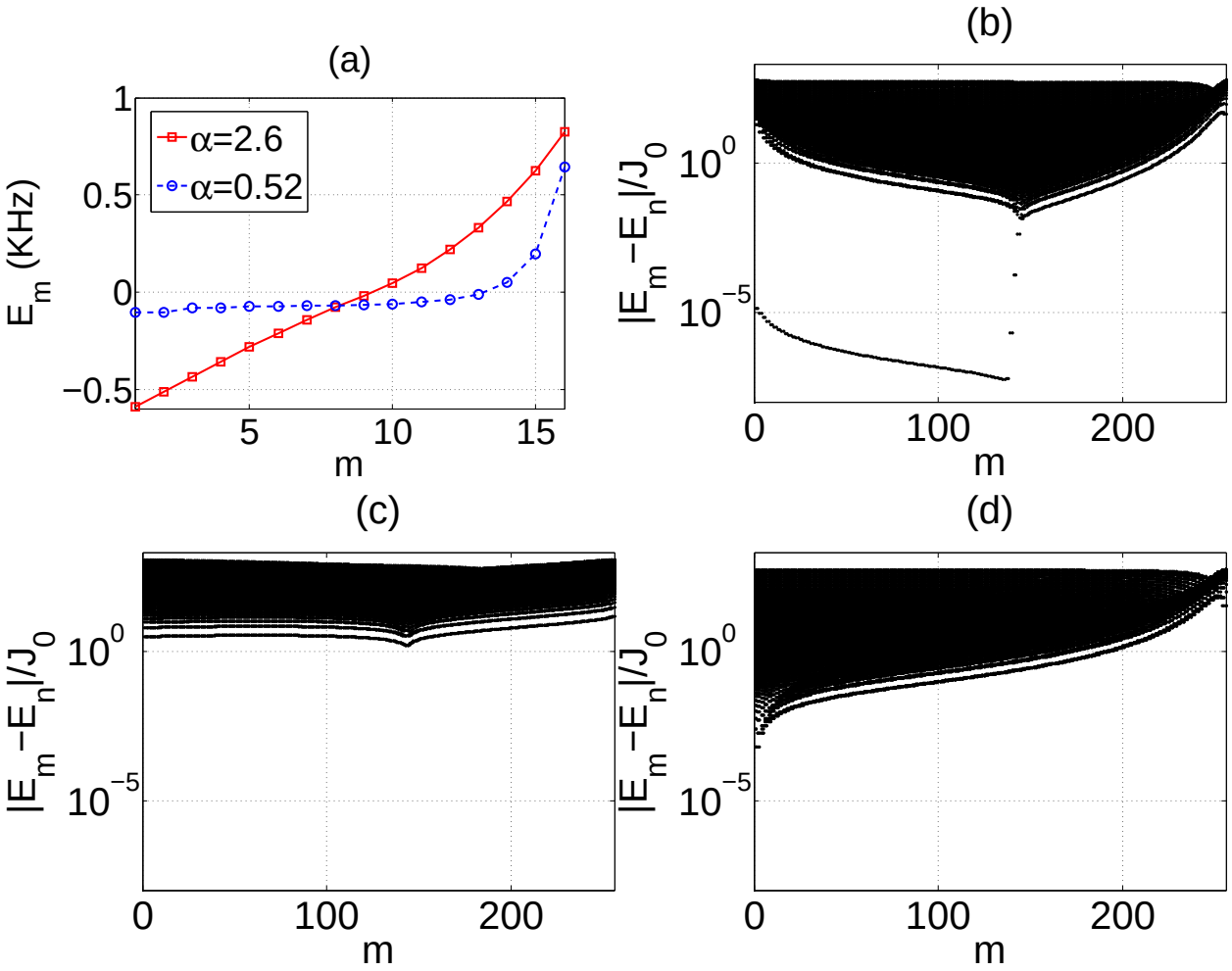

Figure 9.4.1: (a) Energy spectrum in the $n = 1$ subspace for $N = 16$ spins (b-d) Map of eigenenergy differences $\{E_m - E_n\}$ for $N = 256$ spins with (b) $\alpha = 2.4$, (c) $\alpha = 0.74$ and (d) $\alpha = 0.74$ but with homogenous ion chain on a ring.

From Fig. 9.3.3d, we see that the prethermal values cannot be described by GGE. This is simply because H_{XY} in long range interaction case cannot be well approximated by the integrable Hamiltonian H_{int}. The prethermal values also differ from DE predictions (thermal values), but we find that the system can be described by a *partial diagonal ensemble*

(PDE), defined mathematically as

$$\rho_{PDE} = \begin{cases} \rho_{mn}(0)\delta_{mn} & |\nu_m - \nu_n| \gtrsim 1/T \\ \rho_{mn}(0) & |\nu_m - \nu_n| \ll 1/T \end{cases}$$

where T denotes the prethermalization time scale. The PDE correctly predicts prethermal values of local observables, as shown in Fig. 9.3.3d.

We note that the thermal state described by either DE or GGE always has spatial inversion (parity) symmetry, because the interaction pattern J_{ij} shares such symmetry. The reason why prethermal state can break this symmetry is because at intermediate time scale T, one cannot distinguish the near-degenerate pairs of eigenstates in energy, so linear combinations within each pair are allowed. Since each pair consists an even and an odd parity eigenstate, their linear combination can break the spatial inversion symmetry, leading to a symmetry-breaking dynamical phase transition when α is tuned across the critical value.

Another interesting feature worth mentioning is that when $\alpha = 0$, the uniform coupled H_{XY} can be analytically solved, with $N-1$ exact degenerate eigenenergy. In this case, the GGE/DE completely breaks down and only prethermalization stage exists. By calculating the PDE, one finds the prethermal value of $\overline{C}$ to be $\frac{2}{N} - 1$.

The "phase diagram" (Fig. 9.3.4b) has the hint of two non-analytic points serving as critical values of two speculated dynamical phase transitions, one is where $\overline{C}$ becomes non-zero, representing the emergence of prethermalization, and the other is where $\overline{C}$ approaches $\frac{2}{N} - 1$ ($\alpha \to 0$), representing the disappearance of thermalization. We are however, not clear, on how the phase diagram will look like in the thermodynamic limit. Apart from the absence of analytic solution, one also does not have a well-defined ther-

modynamic limit for an inhomogeneous system, as if part of the ion chain has infinitely small density, the phonon modes will have infinitely large density near ω_x, making the simulation of H_{XY} essentially impossible [190].

Finally, we briefly discuss the case where the initial non-equilibrium state has more than one spin excitations: the energy levels in other subspaces are likely to connect the slow time scale branch in Fig. 9.4.1c to fast time scale bulk. Closing the gap between these two energy scales will smear out the prethermalization stage and one will only see a single relaxation stage to thermal state, possibly over a longer time scale (confirmed by additional numerical simulations). But once moved out of the single spin excitation subspace, it would be more interesting to consider quantum quenches on the transverse magnetic field, or even the interaction pattern. Recently, researchers have found evidence of dynamical phase transition in both nearest neighbor [212] and uniform [220] coupled Ising model. We believe that the research on dynamical properties of system with continuously tunable range of interaction, together with its intimate experimental relevance, is far from an end.

Chapter 10

Outlook

In this thesis, we have discussed a wide range of topics on the implementation of quantum computation and quantum simulation, based on either atomic or solid state systems. There are many future directions related to these topics, and we'll mention a few of them in this Chapter below:

Scalable quantum computation with atomic and solid state system

Over the years researchers have achieved single-qubit and two-qubit quantum gates in a variety of physical systems [2], and the real challenge now is how to scale these systems up to perform powerful quantum algorithms. Architectures of scalable quantum processors based on the characteristics of specific system have also been proposed [221–223]. In most of these architectures, optimal quantum control technique and hybrid quantum system are involved, thus we anticipate a lot of future research along these two directions.

Optimal quantum control technique aims to address limited degrees of freedom or limited precision in experimental control of quantum systems. The basic idea is to design time-dependent or space-dependent optical/electrical control pulses and optimize the tar-

get goal, such as decoherence rate of physical qubit, fidelity of quantum gate, speed of quantum state transfer, or required total laser power. In the past, optimal control techniques are mainly focused on single or two qubit operations, such as spin echo protocols [61] and ultrafast gate [42]. The generalization to multi-qubit is thus essential for a large scale quantum computer, but may involve a much more complicated study that is still lacking.

Hybrid quantum system, on the other hand, allows one to combine benefits of different systems and interconnect them to make the quantum processor scalable. For example, one successful hybrid system, known as circuit QED, involves the combination of cavity and superconducting qubits, and has been already used widely in various quantum technologies [224, 225]. Generally speaking, photons (or microwave photons) can serve as an efficient bus for interconnecting same type of physical qubits. But if one moves one step further, photons can also be used to mediate interactions between different types of matter qubits, allowing one to truly take advantage of a variety of quantum systems [122]. Such more complex hybrid system is still in an early developing stage and worth exploring in both theory and experiment.

Quantum simulation of exotic many-body system

Impressively high level of control, engineering and measurement has been achieved on atomic and optical system, including trapped ions, cold atoms in optical lattice, and photons in high-finesse cavity [15, 23, 29]. These well-controlled quantum many-body system have become powerful simulators of condensed matter and high energy models recently [52, 226]. Two particularly interesting systems, related to the topics in this thesis, and can be possibly simulated and explored using atomic systems are:

Spin liquid and topological state of matter: Caused by high level of magnetic frustration, spin liquid is one of the most puzzling states of matter. It is also found that certain kinds of spin liquid have topological excitations that may be used to achieve fault-tolerant quantum computation. Some of these spin liquid states and topological excitations may be easier to find in atomic systems than in condensed matter materials, due to the flexibility of engineering the many-body interactions with AMO techniques. One example is the experimental realization of tunable spin-orbital coupling with cold atoms [227]. Synthesizing artificial quantum materials using atomic systems to bring interesting applications tends to be a very promising direction in the future.

High dimensional system: Spatially periodic structure is ubiquitous in both nature and lab. In condensed matter system, they're known as crystals. To simulate their properties with atomic physics, researchers have created artificial crystals either by optical or electrical lattice potential. However, a time periodic structure is much less explored, especially when studied together with spatial degrees of freedom. Examples such as "Space-time crystal" [47] and "Floquet topological insulator" [228] are recently proposed. These high dimensional systems may open up brand new applications as well as enhancing our understanding of space-time analogy.

Non-equilibrium dynamics of open and isolated quantum system

Our knowledge of condensed matter system is largely at low energy and equilibrium. AMO systems, on the other hand, are often driven far out of equilibrium and even in a dissipative way. The non-equilibrium dynamics of a quantum many-body system is usually intractable due to exponential number of states involved. Nevertheless, AMO systems can be used to probe them with amazingly high spatial and time accuracy. Important future

directions include:

Dynamical phase transition in isolated system: The unitary quantum dynamics seem to eliminate any thermalization behavior of isolated system. However, local observables can have distinctive dynamics based on many factors, including typicality of initial state, integrability of Hamiltonian, etc. A dynamical phase transition will appear if the system shows distinctive dynamical behaviors at different time or under different control parameters. A better theoretical understanding, including a complete definition and characterization, of dynamical phase transition, is highly desired [212]. It is also very likely to probe dynamical phase transition in experiments by exploiting the strength in controlling and measuring atomic systems.

Dissipation in open many-body system: Dissipative dynamics are well studied in single or non-interacting systems. Under strong interaction, however, little is known due to lack of efficient theoretical tools. Furthermore, understanding dissipation is vital for building a quantum computer with large number of interacting qubits, where dissipative process through environment is almost inevitable. Proper engineering of dissipative dynamics, on the other hand, may even offer us novel approaches to generate entanglement and prevent decoherence for many-body system [217, 229].

Appendix A

Analytical Channel Fidelity

We now derive the analytical channel fidelity associated with the paired FFST protocol described in chapter 4. To set up the analytic framework, we begin by calculating the fidelity of a simplified protocol, termed the "double-swap". In this double-swap, we consider the left register (indexed 0) undergoing two successive eigenmode-mediated swap gates. Ideally, this simplified protocol swaps the quantum information twice, thereby disentangling it from the intermediate chain and also returning it to its initial position at the left register. We then consider a second protocol, termed the "single-swap", in which the quantum information undergoes only one eigenmode-mediated swap-gate. Analyzing this protocol will illustrate the effect of the residual entanglement on the channel fidelity. Finally, we turn to the paired-protocol and demonstrate that the proposed two-qubit encoding can eliminate this entanglement, thereby enabling quantum state transfer.

Double-swap

The average channel fidelity for a quantum dynamical operation is given by

$$F = \frac{1}{2} + \frac{1}{12} \sum_{i=x,y,z} \text{Tr}\left[\sigma^i \mathcal{E}(\sigma^i)\right],$$

where $\mathcal{E}$ characterizes the quantum channel [111]. We focus on the Hamiltonian introduced in chapter 4.2 (Eq. 4.3.1):

$$H = g(\sigma_0^+ \sigma_1^- + \sigma_N^+ \sigma_{N+1}^- + \text{h.c.}) + \sum_{i=1}^{N-1} \kappa(\sigma_i^+ \sigma_{i+1}^- + \text{h.c.})$$

For the double-swap (DS), we let U represent evolution under H for a time, $t = 2\tau$, equivalent to twice the state-transfer time. Let us suppose that the left register is initially disentangled from the remainder of the chain, which is in a thermal mixed state ρ_{ch}^{DS}; the average double-swap channel fidelity is then given by,

$$\begin{aligned} F_{DS} &= \frac{1}{2} + \frac{1}{12} \sum_{i=x,y,z} \text{Tr}\left[\sigma_0^i U(\sigma_0^i \otimes \rho_{ch}^{DS})U^\dagger\right] \\ &= \frac{1}{2} + \frac{1}{12} \sum_{i=x,y,z} \text{Tr}\left[U^\dagger \sigma_0^i U(\sigma_0^i \otimes \rho_{ch}^{DS})\right] \\ &= \frac{1}{2} + \frac{1}{12} \sum_{i=x,y,z} \text{Tr}\left[\sigma_0^i(t)(\sigma_0^i \otimes \rho_{ch}^{DS})\right], \end{aligned}$$

where $\sigma_0^i(t)$ is the Heisenberg evolution of the left register. By fermionization, this evolution can be re-expressed with respect to elements of the matrix $M = e^{-iKt}$ where K is the $(N+2) \times (N+2)$ coupling matrix of the full Hamiltonian (including registers), $H = \sum_{i,j=0}^{N+1} K_{ij} c_i^\dagger c_j$. Evolution of the Fermi operators is governed by $\dot{c_m} = -i \sum_n K_{mn} c_n$,

implying that $c_m(t) = \sum_n M_{mn} c_n$ and further, that

$$\begin{aligned}
\sigma_0^+(t) &= U^\dagger \sigma_0^+ U = U^\dagger c_0^\dagger U \\
&= \sum_i M_{0i}^* c_i^\dagger = \sum_i M_{0i}^* \sigma_i^+ \prod_{l<i} e^{i\pi \sigma_l^+ \sigma_l^-},
\end{aligned}$$

$$\begin{aligned}
\sigma_0^z(t) &= 2c_0^\dagger(t) c_0(t) - 1 = -1 + 2\sum_{ij} M_{0i}^* M_{0j} c_i^\dagger c_j \\
&= -1 + 2\sum_{ij} M_{0i}^* M_{0j} \sigma_i^+ \sigma_j^- \prod_{i<l<j} e^{i\pi \sigma_l^+ \sigma_l^-},
\end{aligned}$$

where we have used the fact that $c_0^\dagger$ carries no Wigner string. To evaluate F_{DS}, we note that $\sigma^\pm = (\sigma^x \pm i\sigma^y)/2$, and hence, $\text{Tr}\left[\sigma_0^x(t)(\sigma_0^x \otimes \rho_{ch})\right] = \text{Tr}\left[(\sigma_0^+(t) + \sigma_0^-(t))((\sigma_0^+ + \sigma_0^-) \otimes \rho_{ch})\right]$. Contributions are only obtained from the cross-terms, $\sigma_0^+(t)(\sigma_0^- \otimes \rho_{ch})$ and $\sigma_0^-(t)(\sigma_0^+ \otimes \rho_{ch})$, since the number of excitations in $i = 0$ must be preserved to generate a non-zero trace. For example,

$$\begin{aligned}
&\text{Tr} \quad \left[\sigma_0^+(t)(\sigma_0^- \otimes \rho_{ch})\right] \\
&= \quad \text{Tr}\left[(\sum_i M_{0i}^* \sigma_i^+ \prod_{l<i} e^{i\pi \sigma_l^+ \sigma_l^-})(\sigma_0^- \otimes \rho_{ch})\right] \\
&= \quad \text{Tr}\left[M_{00}^* \sigma_0^+ \sigma_0^- \otimes \rho_{ch}\right] = M_{00}^*.
\end{aligned}$$

An analogous calculation yields Tr $\left[\sigma_0^-(t)(\sigma_0^+ \otimes \rho_{ch})\right] = M_{00}$. Finally, for the σ^z terms, one finds,

$$\begin{aligned} \text{Tr} \quad & [\sigma_0^z(t)(\sigma_0^z \otimes \rho_{ch})] = \text{Tr}\left[-\sigma_0^z \otimes \rho_{ch}\right] \\ + \quad & \text{Tr}\left[(2\sum_{ij} M_{0i}^* M_{0j} \sigma_i^+ \sigma_j^- \prod_{i<l<j} e^{i\pi\sigma_l^+\sigma_l^-})(\sigma_0^z \otimes \rho_{ch})\right] \\ = \quad & \text{Tr}\left[2M_{00}^* M_{00} \sigma_0^+ \sigma_0^- \sigma_0^z \otimes \rho_{ch}\right] = 2|M_{00}|^2, \end{aligned}$$

where we've noted that $i = j$ to ensure that the number of excitations in each mode is conserved. Moreover, we must also have that $i = j = 0$, since Tr$[\sigma_0^z] = 0$. Combining the above terms yields the double-swap channel fidelity as,

$$F_{DS} = \frac{1}{2} + \frac{1}{6}(M_{00} + M_{00}^* + |M_{00}|^2).$$

Interestingly, we need to compute only a single matrix element to obtain the relevant channel fidelity.

Single-swap

We now consider the single-swap (SS) channel fidelity associated with the transfer of quantum information from the right register (indexed $N+1$) to the left register (indexed 0),

$$F_{SS} = \frac{1}{2} + \frac{1}{12} \sum_{i=x,y,z} \text{Tr}\left[\sigma_0^i(t)(\rho_{ch}^{SS} \otimes \sigma_{N+1}^i)\right],$$

where ρ_{ch}^{SS} now characterizes the initial state for spins $\{0, \cdots, N\}$. Note that F_{SS} will be independent of the direction of state transfer, and we have chosen right to left for

notational simplicity. One finds,

$$\begin{aligned}\sigma_0^x(t) &= c_0^\dagger(t) + c_0(t) = \sum_i M_{0i}^* c_i^\dagger + M_{0i} c_i \\ &= \sum_i [\{\text{Re}(M_{0i})\sigma_i^x + \text{Im}(M_{0i})\sigma_i^y\} \prod_{l=0}^{i-1}(-\sigma_l^z)].\end{aligned}$$

In analogy to the DS case, $i \neq N+1$ terms do not contribute to the trace,

$$\text{Tr}[\sigma_0^x(t)(\rho_{ch} \otimes \sigma_{N+1}^x)] = 2\text{Re}(M_{0,N+1})\text{Tr}[\rho_{ch}^{SS} \prod_{l=0}^{N}(-\sigma_l^z)].$$

The σ^y term yields an identical contribution while the σ^z term yields, $\text{Tr}[\sigma_0^z(t)(\rho_{ch}^{SS} \otimes \sigma_{N+1}^z)] = 2|M_{0,N+1}|^2$. Therefore,

$$F_{SS} = \frac{1}{2} + \frac{1}{6}[2\text{Re}(M_{0,N+1})\text{Tr}[\rho_{ch}^{SS} \prod_{l=0}^{N}(-\sigma_l^z)] + |M_{0,N+1}|^2).$$

For perfect transfer with $F_{SS} = 1$, we would require both $|M_{0,N+1}| = 1$ and $|\text{Tr}[\rho_{ch}^{SS} \prod_{l=0}^{N}(-\sigma_l^z)]| = 1$. In the case of an unpolarized chain, the second condition is unsatisfied since the expectation value of the chain parity operator $P = \prod_{l=0}^{N}(-\sigma_l^z)$ is zero. The dependence of the single-swap fidelity on the intermediate chain's parity presents an obvious problem for QST.

Paired-Protocol

To overcome this problem, we now turn to the two-qubit encoding proposed in chapter 4, i.e. $|\downarrow\rangle = |\downarrow\rangle_a|\downarrow\rangle_b$, $|\uparrow\rangle = |\uparrow\rangle_a|\uparrow\rangle_b$. Let us index the full chain as $\{0_a, 0_b, 1, \cdots, N, (N+$

$1)_b, (N+1)_a\}$ and define U_b as the transfer process through the sub-chain $\{0_b, 1, \cdots, N, (N+1)_b\}$, while U_a represents the transfer process through the sub-chain $\{0_a, 1, \cdots, N, (N+1)_a\}$. To model a realistic experimental situation, we will assume that the quantum information is originally encoded in qubit 0_a, while qubit 0_b is prepared in state $|\uparrow\rangle$. A $\mathsf{C}_{0_a}\mathsf{NOT}_{0_b}$ gate is then applied to encode the information in the logical 0-register. After the state transfer, we apply $\mathsf{C}_{(N+1)_b}\mathsf{NOT}_{(N+1)_a}$ to decode our quantum information into qubit $(N+1)_b$. The unitary characterizing the encoding, state transfer, and decoding is then $U = \mathsf{C}_{(N+1)_b}\mathsf{NOT}_{(N+1)_a} U_b U_a \mathsf{C}_{0_a}\mathsf{NOT}_{0_b}$, and the average channel fidelity is given by

$$F_{enc} = \frac{1}{2} + \frac{1}{12} \sum_{i=x,y,z} \mathrm{Tr}\Big[\sigma^i_{N+1}(t)(\sigma^i_0 \otimes \rho^{PP}_{ch} \otimes \rho_{N+1})\Big].$$

Here, ρ^{PP}_{ch} is the mixed initial state of the intermediate chain ($\{1, \cdots, N\}$), while ρ_{N+1} is the mixed state of the encoded $(N+1)$ register within the logical subspace. Working within this logical subspace is crucial to ensure that $\mathsf{CP}_{0_a,N+1_a}\mathsf{CP}_{0_b,N+1_b} = \mathbb{I}$. Inspection reveals that the paired-protocol includes two contributions from the chain parity operator, and since $P^2 = \mathbb{I}$, we have effectively disentangled from the intermediate chain. Since a consistent ordering of the spin-chain is required to implement the Jordan-Wigner transformation, the Hamiltonian, H_{U_a} governing the U_a transfer evolution will contain uncanceled Wigner strings. For example, the piece of H_{U_a} containing the coupling between the registers and the ends of the spin-chain takes the form, $H_{U_a} = g(c^\dagger_{0_a} e^{i\pi n_{0_b}} c_1 + c^\dagger_N e^{i\pi n_{(N+1)_b}} c_{(N+1)_a} + \text{h.c.})$. While one must take care to correctly evaluate such strings, an otherwise straightforward

computation yields,

$$\begin{aligned} F_{enc} &= \frac{1}{6}(2|M_{0,N+1}|^2 \mathrm{Re}\left[M_{0,N+1}^2 - M_{0,0}M_{N+1,N+1}\right] \\ &+ |M_{0,N+1}|^2 + |\sum_{i=1}^{N} M_{N+1,i}M_{i,0}|^2) + \frac{1}{2}. \end{aligned}$$

Again, one only needs to compute certain matrix elements of M.

Before concluding this appendix, we point out that one can alternatively decode the quantum information into qubit $(N+1)_a$ via $\mathrm{C}_{(N+1)_a}\mathrm{NOT}_{(N+1)_b}$. In this case, the expression for F_{enc} above is identical, except the term $|\sum_{i=1}^{N} M_{N+1,i}M_{i,0}|^2$ is not present. Thus, the decoding into qubit $(N+1)_b$ described above gives a slightly higher average fidelity, which is used in the numerical simulations in chapter 4.

Appendix B

Hamiltonian in ring ion trap

We provide some details about the ring ion trap used in chapter 7 and 8 in this appendix. The ring-shaped trapping potential can be created by a quadrupole storage ring trap [230, 231], a linear rf multipole trap [188, 232] or other methods.

Quadrupole ring trap. A rf quadrupole ring trap can be formed by many segments of quadrupole electrodes [230] or four ring electrodes [231]. The harmonic pseudo-potential for a single ion is $V_{ext}(r,z) = \frac{1}{2}M\omega_r^2(r-r_{min})^2 + \frac{1}{2}M\omega_z^2 z^2$, where $r = \sqrt{x^2+y^2}$ is the radial position of the ion, r_{min} is the radius of the ring trap, ω_r and ω_z are trapping frequencies in the radial and axial (z) directions, respectively. If the inner radius of the trap (r_0, which is half of the separation between opposite electrodes [230]) is much smaller than r_{min}, the trapping frequencies are approximately $\omega_r = \omega_z = qV_{rf}/(\sqrt{2}M\Omega r_0^2)$. Here V_{rf} is the amplitude of the rf voltage applied to adjacent electrodes, $\Omega/2\pi$ is frequency of the rf voltage. In Fig. 1c, $\omega_r = 2\pi \times 5$ MHz and $r_{min} = 20\,\mu$m for the quadrupole ring trap.

Linear rf multiple trap. The pseudo-potential for a single ion in a linear rf multipole trap is cylindrically symmetric [188, 232]:

$$V_{ext}(r,z) = \frac{k^2q^2V_{rf}^2}{16M\Omega^2r_0^2}(\frac{r}{r_0})^{2k-2} + \frac{\beta qV_{dc}}{z_0^2}(z^2 - \frac{r^2}{2}),$$

where $2k$ is the number of poles of the trap, β is the geometrical factor of the trap, V_{dc} is the static voltage applied to the outside sets of segmented electrodes, and $2z_0$ is the length of the center part of the segmented trap. The trapping frequency in the axial direction is $\omega_z = \sqrt{2\beta q V_{dc}/(M z_0^2)}$. The trapping potential has its minimum value in the radial direction at

$$r_{min} = r_0 \left(\frac{2M\Omega\omega_z r_0^2}{qV_{rf}k\sqrt{k-1}} \right)^{1/(k-2)}.$$

The trapping frequency in the radial direction is $\omega_r = \sqrt{k-2}\,\omega_z$ near r_{min}. Fig. 1c shows an example of the effective trapping potential for a $^9Be^+$ ion in the radial plane of an octupole trap ($2k$ = 8). The parameters used for the calculation of Fig. 7.1.1c are $r_0 = 200\,\mu$m, V_{rf} = 200 V, $\omega_z/2\pi = 0.5$ MHz, and $\Omega/2\pi$ = 94 MHz.

Many-body Hamiltonian. As we are interested in the rotation of ions in a ring at very low temperatures, our Hamiltonian only involves the angular coordinate θ_j ($j = 1, \cdots, N$) of trapped ions:

$$H = \sum_{j=1}^{N} \frac{(p_j - qA_\theta)^2}{2M} + \sum_{j<l} \frac{q^2}{4\pi\epsilon_0 d|\sin(\frac{\theta_j-\theta_l}{2})|},$$

where $p_j = -i\frac{2\hbar}{d}\frac{\partial}{\partial\theta_j}$ is the canonical momentum operator, $A_\theta = Bd/4 = \phi/(\pi d)$ is the vector potential, and ϵ_0 is the electric constant of vacuum. $\phi = \pi d^2 B/4$ is the magnetic flux inside the ion ring. This Hamiltonian can be further expanded around equilibrium positions of ions to give phonon mode frequencies.

Bibliography

[1] M. Nielsen, *Quantum computation and quantum information*. Cambridge: Cambridge University Press, 10th anniversary ed., 2010.

[2] T. D. Ladd, F. Jelezko, R. Laflamme, Y. Nakamura, C. Monroe, and J. L. O'Brien, "Quantum computers," *Nature*, vol. 464, pp. 45–53, Mar. 2010.

[3] A. Y. Kitaev, A. Shen, and M. N. Vyalyi, *Classical and quantum computation*. Providence, R.I.: American Mathematical Society, 2002.

[4] D. Bouwmeester, A. K. Ekert, and A. Zeilinger, *The physics of quantum information: quantum cryptography, quantum teleportation, quantum computation*. Berlin ; New York: Springer, 1st ed., 2000.

[5] A. Steane, "Quantum computing," *Reports on Progress in Physics*, vol. 61, p. 117, Feb. 1998.

[6] A. Ekert and R. Jozsa, "Quantum computation and shor's factoring algorithm," *Reviews of Modern Physics*, vol. 68, pp. 733–753, July 1996.

[7] R. P. Feynman, "Simulating physics with computers," *International Journal of Theoretical Physics*, vol. 21, pp. 467–488, June 1982.

[8] D. Deutsch, "Quantum theory, the church-turing principle and the universal quantum computer," *Proceedings of the Royal Society of London. A. Mathematical and Physical Sciences*, vol. 400, pp. 97–117, July 1985.

[9] D. Deutsch and R. Jozsa, "Rapid solution of problems by quantum computation," *Proceedings of the Royal Society of London. Series A: Mathematical and Physical Sciences*, vol. 439, pp. 553–558, Dec. 1992.

[10] P. W. Shor, "Polynomial-time algorithms for prime factorization and discrete logarithms on a quantum computer," *arXiv:quant-ph/9508027*, Aug. 1995. SIAM J.Sci.Statist.Comput. 26 (1997) 1484.

[11] L. K. Grover, "Quantum mechanics helps in searching for a needle in a haystack," *Physical Review Letters*, vol. 79, pp. 325–328, July 1997.

[12] D. S. Abrams and S. Lloyd, "Quantum algorithm providing exponential speed increase for finding eigenvalues and eigenvectors," *Physical Review Letters*, vol. 83, no. 24, pp. 5162–5165, 1999.

[13] Gurvits and Samorodnitsky, "A deterministic algorithm for approximating the mixed discriminant and mixed volume, and a combinatorial corollary," *Discrete & Computational Geometry*, vol. 27, pp. 531–550, Jan. 2002.

[14] D. P. DiVincenzo, "The physical implementation of quantum computation," *Fortschritte der Physik*, vol. 48, pp. 771–783, Sept. 2000.

[15] D. Leibfried, R. Blatt, C. Monroe, and D. Wineland, "Quantum dynamics of single trapped ions," *Reviews of Modern Physics*, vol. 75, no. 1, p. 281, 2003.

[16] D. J. Wineland and D. Leibfried, "Quantum information processing and metrology with trapped ions," *Laser Physics Letters*, vol. 8, pp. 175–188, Mar. 2011.

[17] L.-M. Duan, "Colloquium: Quantum networks with trapped ions," *Reviews of Modern Physics*, vol. 82, pp. 1209–1224, Apr. 2010.

[18] M. Saffman, T. G. Walker, and K. Mølmer, "Quantum information with rydberg atoms," *Reviews of Modern Physics*, vol. 82, pp. 2313–2363, Aug. 2010.

[19] D. Jaksch and P. Zoller, "The cold atom hubbard toolbox," *Annals of Physics*, vol. 315, pp. 52–79, Jan. 2005.

[20] M. Hofheinz, H. Wang, M. Ansmann, R. C. Bialczak, E. Lucero, M. Neeley, A. D. O'Connell, D. Sank, J. Wenner, J. M. Martinis, and A. N. Cleland, "Synthesizing arbitrary quantum states in a superconducting resonator," *Nature*, vol. 459, pp. 546–549, May 2009.

[21] L. DiCarlo, J. M. Chow, J. M. Gambetta, L. S. Bishop, B. R. Johnson, D. I. Schuster, J. Majer, A. Blais, L. Frunzio, S. M. Girvin, and R. J. Schoelkopf, "Demonstration of two-qubit algorithms with a superconducting quantum processor," *Nature*, vol. 460, pp. 240–244, July 2009.

[22] R. Hanson, L. P. Kouwenhoven, J. R. Petta, S. Tarucha, and L. M. K. Vandersypen, "Spins in few-electron quantum dots," *Reviews of Modern Physics*, vol. 79, pp. 1217–1265, Oct. 2007.

[23] J. L. O'Brien, A. Furusawa, and J. Vučković, "Photonic quantum technologies," *Nature Photonics*, vol. 3, p. 687, Dec. 2009.

[24] J. Wrachtrup and F. Jelezko, "Processing quantum information in diamond," *Journal of Physics: Condensed Matter*, vol. 18, p. S807, May 2006.

[25] S. Lloyd, "A potentially realizable quantum computer," *Science*, vol. 261, pp. 1569–1571, Sept. 1993.

[26] A. Trabesinger, "Quantum simulation," *Nature Physics*, vol. 8, pp. 263–263, Apr. 2012.

[27] K. Kim, M.-S. Chang, S. Korenblit, R. Islam, E. E. Edwards, J. K. Freericks, G.-D. Lin, L.-M. Duan, and C. Monroe, "Quantum simulation of frustrated ising spins with trapped ions," *Nature*, vol. 465, pp. 590–593, June 2010.

[28] B. P. Lanyon, C. Hempel, D. Nigg, M. Muller, R. Gerritsma, F. Zahringer, P. Schindler, J. T. Barreiro, M. Rambach, G. Kirchmair, M. Hennrich, P. Zoller, R. Blatt, and C. F. Roos, "Universal digital quantum simulation with trapped ions," *Science*, vol. 334, pp. 57–61, Sept. 2011.

[29] I. Bloch, J. Dalibard, and W. Zwerger, "Many-body physics with ultracold gases," *Reviews of Modern Physics*, vol. 80, no. 3, p. 885, 2008.

[30] I. Bloch, J. Dalibard, and S. Nascimbène, "Quantum simulations with ultracold quantum gases," *Nature Physics*, vol. 8, pp. 267–276, Apr. 2012.

[31] X.-s. Ma, B. Dakic, W. Naylor, A. Zeilinger, and P. Walther, "Quantum simulation of the wavefunction to probe frustrated heisenberg spin systems," *Nature Physics*, vol. 7, pp. 399–405, Feb. 2011.

[32] A. Aspuru-Guzik and P. Walther, "Photonic quantum simulators," *Nature Physics*, vol. 8, pp. 285–291, Apr. 2012.

[33] Z.-X. Gong, Z.-q. Yin, and L.-M. Duan, "Dynamics of the overhauser field under nuclear spin diffusion in a quantum dot," *New Journal of Physics*, vol. 13, p. 033036, Mar. 2011.

[34] X. Xu, W. Yao, B. Sun, D. G. Steel, A. S. Bracker, D. Gammon, and L. J. Sham, "Optically controlled locking of the nuclear field via coherent dark-state spectroscopy," *Nature*, vol. 459, pp. 1105–1109, June 2009.

[35] B. Sun, W. Yao, X. Xu, A. S. Bracker, D. Gammon, L. J. Sham, and D. Steel, "Persistent optical nuclear spin narrowing in a singly charged InAs quantum dot," *Journal of the Optical Society of America B*, vol. 29, pp. A119–A126, Feb. 2012.

[36] D. J. Reilly, J. M. Taylor, J. R. Petta, C. M. Marcus, M. P. Hanson, and A. C. Gossard, "Suppressing spin qubit dephasing by nuclear state preparation," *Science*, vol. 321, pp. 817–821, Aug. 2008.

[37] C. Latta, A. Högele, Y. Zhao, A. N. Vamivakas, P. Maletinsky, M. Kroner, J. Dreiser, I. Carusotto, A. Badolato, D. Schuh, W. Wegscheider, M. Atature, and A. Imamoglu, "Confluence of resonant laser excitation and bidirectional quantum-dot nuclear-spin polarization," *Nature Physics*, vol. 5, pp. 758–763, Oct. 2009.

[38] I. T. Vink, K. C. Nowack, F. H. L. Koppens, J. Danon, Y. V. Nazarov, and L. M. K. Vandersypen, "Locking electron spins into magnetic resonance by electron–nuclear feedback," *Nature Physics*, vol. 5, pp. 764–768, Oct. 2009.

[39] D. Kim, S. G. Carter, A. Greilich, A. S. Bracker, and D. Gammon, "Ultrafast optical control of entanglement between two quantum-dot spins," *Nature Physics*, vol. 7, pp. 223–229, Dec. 2010.

[40] M. F. Doty, M. Scheibner, A. S. Bracker, I. V. Ponomarev, T. L. Reinecke, and D. Gammon, "Optical spectra of doubly charged quantum dot molecules in electric and magnetic fields," *Physical Review B*, vol. 78, p. 115316, Sept. 2008.

[41] G.-D. Lin, S.-L. Zhu, R. Islam, K. Kim, M.-S. Chang, S. Korenblit, C. Monroe, and L.-M. Duan, "Large-scale quantum computation in an anharmonic linear ion trap," *EPL (Europhysics Letters)*, vol. 86, p. 60004, June 2009.

[42] S.-L. Zhu, C. Monroe, and L.-M. Duan, "Arbitrary-speed quantum gates within large ion crystals through minimum control of laser beams," *Europhysics Letters (EPL)*, vol. 73, pp. 485–491, Feb. 2006.

[43] N. Y. Yao, L. Jiang, A. V. Gorshkov, Z.-X. Gong, A. Zhai, L.-M. Duan, and M. D. Lukin, "Robust quantum state transfer in random unpolarized spin chains," *Physical Review Letters*, vol. 106, no. 4, p. 040505, 2011.

[44] N. Y. Yao, Z.-X. Gong, C. R. Laumann, S. D. Bennett, L.-M. Duan, M. D. Lukin, L. Jiang, and A. V. Gorshkov, "Quantum logic between remote quantum registers," *Physical Review A*, vol. 87, p. 022306, Feb. 2013.

[45] E. Waks and C. Monroe, "Protocol for hybrid entanglement between a trapped atom and a quantum dot," *Physical Review A*, vol. 80, p. 062330, Dec. 2009.

[46] Z.-X. Gong, G.-D. Lin, and L.-M. Duan, "Temperature-driven structural phase transition for trapped ions and a proposal for its experimental detection," *Physical Review Letters*, vol. 105, no. 26, p. 265703, 2010.

[47] T. Li, Z.-X. Gong, Z.-Q. Yin, H. T. Quan, X. Yin, P. Zhang, L.-M. Duan, and X. Zhang, "Space-time crystals of trapped ions," *Physical Review Letters*, vol. 109, p. 163001, Oct. 2012.

[48] F. Wilczek, "Quantum time crystals," *Physical Review Letters*, vol. 109, p. 160401, Oct. 2012.

[49] J. Zakrzewski, "Crystals of time," *Physics*, vol. 5, 2012.

[50] P. Coleman, "Quantum physics: Time crystals," *Nature*, vol. 493, pp. 166–167, Jan. 2013.

[51] R. Islam, E. Edwards, K. Kim, S. Korenblit, C. Noh, H. Carmichael, G.-D. Lin, L.-M. Duan, C.-C. Joseph Wang, J. Freericks, and C. Monroe, "Onset of a quantum phase transition with a trapped ion quantum simulator," *Nat Commun*, vol. 2, p. 377, 2011.

[52] R. Islam, C. Senko, W. C. Campbell, S. Korenblit, J. Smith, A. Lee, E. E. Edwards, C.-C. J. Wang, J. K. Freericks, and C. Monroe, "Emergence and frustration of magnetic order with variable-range interactions in a trapped ion quantum simulator," *arXiv:1210.0142*, Sept. 2012.

[53] J. W. Britton, B. C. Sawyer, A. C. Keith, C.-C. J. Wang, J. K. Freericks, H. Uys, M. J. Biercuk, and J. J. Bollinger, "Engineered two-dimensional ising interactions in a trapped-ion quantum simulator with hundreds of spins," *Nature*, vol. 484, pp. 489–492, Apr. 2012.

[54] D. Loss and D. P. DiVincenzo, "Quantum computation with quantum dots," *Physical Review A*, vol. 57, pp. 120–126, Jan. 1998.

[55] J. M. Taylor, H.-A. Engel, W. Dür, A. Yacoby, C. M. Marcus, P. Zoller, and M. D. Lukin, "Fault-tolerant architecture for quantum computation using electrically controlled semiconductor spins," *Nature Physics*, vol. 1, pp. 177–183, Dec. 2005.

[56] J. R. Petta, A. C. Johnson, J. M. Taylor, E. A. Laird, A. Yacoby, M. D. Lukin, C. M. Marcus, M. P. Hanson, and A. C. Gossard, "Coherent manipulation of coupled electron spins in semiconductor quantum dots," *Science*, vol. 309, pp. 2180–2184, Sept. 2005.

[57] X. Xu, Y. Wu, B. Sun, Q. Huang, J. Cheng, D. G. Steel, A. S. Bracker, D. Gammon, C. Emary, and L. J. Sham, "Fast spin state initialization in a singly charged InAs-GaAs quantum dot by optical cooling," *Physical Review Letters*, vol. 99, p. 097401, Aug. 2007.

[58] A. V. Khaetskii, D. Loss, and L. Glazman, "Electron spin decoherence in quantum dots due to interaction with nuclei," *Physical Review Letters*, vol. 88, p. 186802, Apr. 2002.

[59] F. H. L. Koppens, K. C. Nowack, and L. M. K. Vandersypen, "Spin echo of a single electron spin in a quantum dot," *Physical Review Letters*, vol. 100, p. 236802, June 2008.

[60] L. Viola, E. Knill, and S. Lloyd, "Dynamical decoupling of open quantum systems," *Physical Review Letters*, vol. 82, pp. 2417–2421, Mar. 1999.

[61] L.-M. Duan and G.-C. Guo, "Suppressing environmental noise in quantum computation through pulse control," *Physics Letters A*, vol. 261, pp. 139–144, Oct. 1999.

[62] P. Zanardi, "Symmetrizing evolutions," *Physics Letters A*, vol. 258, pp. 77–82, July 1999.

[63] H. K. Ng, D. A. Lidar, and J. Preskill, "Combining dynamical decoupling with fault-tolerant quantum computation," *arXiv:0911.3202*, Nov. 2009. Phys. Rev. A 84, 012305 (2011).

[64] A. Imamolu, E. Knill, L. Tian, and P. Zoller, "Optical pumping of quantum-dot nuclear spins," *Physical Review Letters*, vol. 91, p. 017402, July 2003.

[65] A. Greilich, A. Shabaev, D. R. Yakovlev, A. L. Efros, I. A. Yugova, D. Reuter, A. D. Wieck, and M. Bayer, "Nuclei-induced frequency focusing of electron spin coherence," *Science*, vol. 317, pp. 1896–1899, Sept. 2007.

[66] J. R. Petta, J. M. Taylor, A. C. Johnson, A. Yacoby, M. D. Lukin, C. M. Marcus, M. P. Hanson, and A. C. Gossard, "Dynamic nuclear polarization with single electron spins," *Physical Review Letters*, vol. 100, p. 067601, Feb. 2008.

[67] D. J. Reilly, J. M. Taylor, J. R. Petta, C. M. Marcus, M. P. Hanson, and A. C. Gossard, "Exchange control of nuclear spin diffusion in a double quantum dot," *Physical Review Letters*, vol. 104, p. 236802, June 2010.

[68] P. Maletinsky, A. Badolato, and A. Imamoglu, "Dynamics of quantum dot nuclear spin polarization controlled by a single electron," *Physical Review Letters*, vol. 99, p. 056804, Aug. 2007.

[69] A. E. Nikolaenko, E. A. Chekhovich, M. N. Makhonin, I. W. Drouzas, A. B. Van'kov, J. Skiba-Szymanska, M. S. Skolnick, P. Senellart, D. Martrou, A. Lemaître, and A. I. Tartakovskii, "Suppression of nuclear spin diffusion at a GaAs/Al_{x}Ga_{1x}As interface measured with a single quantum-dot nanoprobe," *Physical Review B*, vol. 79, p. 081303, Feb. 2009.

[70] M. N. Makhonin, A. I. Tartakovskii, A. B. Van'kov, I. Drouzas, T. Wright, J. Skiba-Szymanska, A. Russell, V. I. Fal'ko, M. S. Skolnick, H.-Y. Liu, and M. Hopkinson, "Long nuclear spin polarization decay times controlled by optical pumping in individual quantum dots," *Physical Review B*, vol. 77, p. 125307, Mar. 2008.

[71] W. M. Witzel and S. Das Sarma, "Wavefunction considerations for the central spin decoherence problem in a nuclear spin bath," *Physical Review B*, vol. 77, p. 165319, Apr. 2008.

[72] P. Maletinsky, M. Kroner, and A. Imamoglu, "Breakdown of the nuclear-spin-temperature approach in quantum-dot demagnetization experiments," *Nature Physics*, vol. 5, pp. 407–411, June 2009.

[73] I. J. Lowe and S. Gade, "Density-matrix derivation of the spin-diffusion equation," *Physical Review*, vol. 156, pp. 817–825, Apr. 1967.

[74] C. Deng and X. Hu, "Nuclear spin diffusion in quantum dots: Effects of inhomogeneous hyperfine interaction," *Physical Review B*, vol. 72, p. 165333, Oct. 2005.

[75] D. Klauser, W. A. Coish, and D. Loss, "Nuclear spin dynamics and zeno effect in quantum dots and defect centers," *Physical Review B*, vol. 78, p. 205301, Nov. 2008.

[76] J. Schliemann, A. V. Khaetskii, and D. Loss, "Spin decay and quantum parallelism," *Physical Review B*, vol. 66, p. 245303, Dec. 2002.

[77] R. I. Dzhioev and V. L. Korenev, "Stabilization of the electron-nuclear spin orientation in quantum dots by the nuclear quadrupole interaction," *Physical Review Letters*, vol. 99, p. 037401, July 2007.

[78] H. O. H. Churchill, A. J. Bestwick, J. W. Harlow, F. Kuemmeth, D. Marcos, C. H. Stwertka, S. K. Watson, and C. M. Marcus, "Electron–nuclear interaction in 13C nanotube double quantum dots," *Nature Physics*, vol. 5, pp. 321–326, May 2009.

[79] T. Belhadj, T. Kuroda, C.-M. Simon, T. Amand, T. Mano, K. Sakoda, N. Koguchi, X. Marie, and B. Urbaszek, "Optically monitored nuclear spin dynamics in individual GaAs quantum dots grown by droplet epitaxy," *Physical Review B*, vol. 78, p. 205325, Nov. 2008.

[80] C.-W. Huang and X. Hu, "Theoretical study of nuclear spin polarization and depolarization in self-assembled quantum dots," *Physical Review B*, vol. 81, p. 205304, May 2010.

[81] R. Brunner, Y.-S. Shin, T. Obata, M. Pioro-Ladrière, T. Kubo, K. Yoshida, T. Taniyama, Y. Tokura, and S. Tarucha, "Two-qubit gate of combined single-spin rotation and interdot spin exchange in a double quantum dot," *Physical Review Letters*, vol. 107, p. 146801, Sept. 2011.

[82] D. Press, T. D. Ladd, B. Zhang, and Y. Yamamoto, "Complete quantum control of a single quantum dot spin using ultrafast optical pulses," *Nature*, vol. 456, pp. 218–221, Nov. 2008.

[83] P. Berman, *Principles of laser spectroscopy and quantum optics*. Princeton N.J.: Princeton University Press, 2011.

[84] A. D. Greentree, J. H. Cole, A. R. Hamilton, and L. C. L. Hollenberg, "Coherent electronic transfer in quantum dot systems using adiabatic passage," *Physical Review B*, vol. 70, p. 235317, Dec. 2004.

[85] B. B. Blinov, D. L. Moehring, L.-M. Duan, and C. Monroe, "Observation of entanglement between a single trapped atom and a single photon," *Nature*, vol. 428, pp. 153–157, Mar. 2004.

[86] P. Maunz, D. L. Moehring, S. Olmschenk, K. C. Younge, D. N. Matsukevich, and C. Monroe, "Quantum interference of photon pairs from two remote trapped atomic ions," *Nature Physics*, vol. 3, pp. 538–541, June 2007.

[87] E. Togan, Y. Chu, A. S. Trifonov, L. Jiang, J. Maze, L. Childress, M. V. G. Dutt, A. S. Sørensen, P. R. Hemmer, A. S. Zibrov, and M. D. Lukin, "Quantum entanglement between an optical photon and a solid-state spin qubit," *Nature*, vol. 466, no. 7307, pp. 730–734, 2010.

[88] D. Kielpinski, C. Monroe, and D. J. Wineland, "Architecture for a large-scale ion-trap quantum computer," *Nature*, vol. 417, pp. 709–711, June 2002.

[89] S. Bose, "Quantum communication through an unmodulated spin chain," *Physical Review Letters*, vol. 91, no. 20, p. 207901, 2003.

[90] D. Petrosyan, G. M. Nikolopoulos, and P. Lambropoulos, "State transfer in static and dynamic spin chains with disorder," *Physical Review A*, vol. 81, p. 042307, Apr. 2010.

[91] M. Christandl, N. Datta, A. Ekert, and A. J. Landahl, "Perfect state transfer in quantum spin networks," *Physical Review Letters*, vol. 92, no. 18, p. 187902, 2004.

[92] D. Burgarth, V. Giovannetti, and S. Bose, "Optimal quantum-chain communication by end gates," *Physical Review A*, vol. 75, p. 062327, June 2007.

[93] M.-H. Yung and S. Bose, "Perfect state transfer, effective gates, and entanglement generation in engineered bosonic and fermionic networks," *Physical Review A*, vol. 71, p. 032310, Mar. 2005.

[94] A. Kay, "Unifying quantum state transfer and state amplification," *Physical Review Letters*, vol. 98, p. 010501, Jan. 2007.

[95] S. R. Clark, C. M. Alves, and D. Jaksch, "Efficient generation of graph states for quantum computation," *New Journal of Physics*, vol. 7, p. 124, May 2005.

[96] L. Campos Venuti, S. M. Giampaolo, F. Illuminati, and P. Zanardi, "Long-distance entanglement and quantum teleportation in XX spin chains," *Physical Review A*, vol. 76, no. 5, p. 052328, 2007.

[97] G. Gualdi, V. Kostak, I. Marzoli, and P. Tombesi, "Perfect state transfer in long-range interacting spin chains," *Physical Review A*, vol. 78, p. 022325, Aug. 2008.

[98] M. Paternostro, G. M. Palma, M. S. Kim, and G. Falci, "Quantum-state transfer in imperfect artificial spin networks," *Physical Review A*, vol. 71, p. 042311, Apr. 2005.

[99] D. I. Tsomokos, M. J. Hartmann, S. F. Huelga, and M. B. Plenio, "Entanglement dynamics in chains of qubits with noise and disorder," *New Journal of Physics*, vol. 9, p. 79, Mar. 2007.

[100] W. Zurek, U. Dorner, and P. Zoller, "Dynamics of a quantum phase transition," *Physical Review Letters*, vol. 95, Sept. 2005.

[101] L. Banchi, T. Apollaro, A. Cuccoli, R. Vaia, and P. Verrucchi, "Optimal dynamics for quantum-state and entanglement transfer through homogeneous quantum systems," *Physical Review A*, vol. 82, Nov. 2010.

[102] J. Gong and P. Brumer, "Controlled quantum-state transfer in a spin chain," *Physical Review A*, vol. 75, p. 032331, Mar. 2007.

[103] N. Yao, L. Jiang, A. Gorshkov, P. Maurer, G. Giedke, J. Cirac, and M. Lukin, "Scalable architecture for a room temperature solid-state quantum information processor," *Nature Communications*, vol. 3, p. 800, Apr. 2012.

[104] P. Cappellaro, C. Ramanathan, and D. G. Cory, "Simulations of information transport in spin chains," *Physical Review Letters*, vol. 99, p. 250506, Dec. 2007.

[105] J. Zhang, M. Ditty, D. Burgarth, C. A. Ryan, C. M. Chandrashekar, M. Laforest, O. Moussa, J. Baugh, and R. Laflamme, "Quantum data bus in dipolar coupled nuclear spin qubits," *Physical Review A*, vol. 80, p. 012316, July 2009.

[106] J. Fitzsimons and J. Twamley, "Globally controlled quantum wires for perfect qubit transport, mirroring, and computing," *Physical Review Letters*, vol. 97, p. 090502, Sept. 2006.

[107] M. Stoneham, "Is a room-temperature, solid-state quantum computer mere fantasy?," *Physics*, vol. 2, p. 34, Apr. 2009.

[108] E. Lieb, T. Schultz, and D. Mattis, "Two soluble models of an antiferromagnetic chain," *Annals of Physics*, vol. 16, no. 3, pp. 407–466, 1961.

[109] A. V. Gorshkov, J. Otterbach, E. Demler, M. Fleischhauer, and M. D. Lukin, "Photonic phase gate via an exchange of fermionic spin waves in a spin chain," *Physical Review Letters*, vol. 105, p. 060502, Aug. 2010.

[110] M. Markiewicz and M. Wieśniak, "Perfect state transfer without state initialization and remote collaboration," *Physical Review A*, vol. 79, no. 5, p. 054304, 2009.

[111] Michael A Nielsen, "A simple formula for the average gate fidelity of a quantum dynamical operation," *Physics Letters A*, vol. 303, no. 4, pp. 249–252, 2002.

[112] E. H. Lieb and D. W. Robinson, "The finite group velocity of quantum spin systems," *Communications in Mathematical Physics*, vol. 28, pp. 251–257, Sept. 1972.

[113] L. Banchi, T. J. G. Apollaro, A. Cuccoli, R. Vaia, and P. Verrucchi, "Long quantum channels for high-quality entanglement transfer," *New Journal of Physics*, vol. 13, p. 123006, Dec. 2011.

[114] A. Bayat, L. Banchi, S. Bose, and P. Verrucchi, "Initializing an unmodulated spin chain to operate as a high-quality quantum data bus," *Physical Review A*, vol. 83, no. 6, p. 062328, 2011.

[115] A. Zwick, G. A. Álvarez, J. Stolze, and O. Osenda, "Spin chains for robust state transfer: Modified boundary couplings versus completely engineered chains," *Physical Review A*, vol. 85, no. 1, p. 012318, 2012.

[116] L. Childress, J. M. Taylor, A. S. Sørensen, and M. D. Lukin, "Fault-tolerant quantum communication based on solid-state photon emitters," *Physical Review Letters*, vol. 96, p. 070504, Feb. 2006.

[117] G. Balasubramanian, P. Neumann, D. Twitchen, M. Markham, R. Kolesov, N. Mizuochi, J. Isoya, J. Achard, J. Beck, J. Tissler, V. Jacques, P. R. Hemmer, F. Jelezko, and J. Wrachtrup, "Ultralong spin coherence time in isotopically engineered diamond," *Nature Materials*, vol. 8, pp. 383–387, May 2009.

[118] P. C. Maurer, J. R. Maze, P. L. Stanwix, L. Jiang, A. V. Gorshkov, A. A. Zibrov, B. Harke, J. S. Hodges, A. S. Zibrov, A. Yacoby, D. Twitchen, S. W. Hell, R. L. Walsworth, and M. D. Lukin, "Far-field optical imaging and manipulation of individual spins with nanoscale resolution," *Nat Phys*, vol. 6, no. 11, pp. 912–918, 2010.

[119] F. Evers and A. D. Mirlin, "Anderson transitions," *Reviews of Modern Physics*, vol. 80, pp. 1355–1417, Oct. 2008.

[120] Y. Zou, R. Barnett, and G. Refael, "Particle-hole symmetric localization in optical lattices using time modulated random on-site potentials," *Physical Review B*, vol. 82, p. 224205, Dec. 2010.

[121] D. Burgarth, K. Maruyama, and F. Nori, "Coupling strength estimation for spin chains despite restricted access," *Physical Review A*, vol. 79, p. 020305, Feb. 2009.

[122] Z.-L. Xiang, S. Ashhab, J. Q. You, and F. Nori, "Hybrid quantum circuits: Superconducting circuits interacting with other quantum systems," *arXiv:1204.2137*, Apr. 2012.

[123] I. Buluta, S. Ashhab, and F. Nori, "Natural and artificial atoms for quantum computation," *Reports on Progress in Physics*, vol. 74, p. 104401, Oct. 2011.

[124] T. Duty, "Towards superconductor-spin ensemble hybrid quantum systems," *Physics*, vol. 3, p. 80, Sept. 2010.

[125] M. Blencowe, "Quantum computing: Quantum RAM," *Nature*, vol. 468, pp. 44–45, Nov. 2010.

[126] K. D. Petersson, L. W. McFaul, M. D. Schroer, M. Jung, J. M. Taylor, A. A. Houck, and J. R. Petta, "Circuit quantum electrodynamics with a spin qubit," *Nature*, vol. 490, pp. 380–383, Oct. 2012.

[127] D. L. Moehring, P. Maunz, S. Olmschenk, K. C. Younge, D. N. Matsukevich, L.-M. Duan, and C. Monroe, "Entanglement of single-atom quantum bits at a distance," *Nature*, vol. 449, pp. 68–71, Sept. 2007.

[128] K. C. Lee, M. R. Sprague, B. J. Sussman, J. Nunn, N. K. Langford, X. M. Jin, T. Champion, P. Michelberger, K. F. Reim, D. England, D. Jaksch, and I. A. Walmsley, "Entangling macroscopic diamonds at room temperature," *Science*, vol. 334, pp. 1253–1256, Dec. 2011.

[129] H. Bernien, B. Hensen, W. Pfaff, G. Koolstra, M. S. Blok, L. Robledo, T. H. Taminiau, M. Markham, D. J. Twitchen, L. Childress, and R. Hanson, "Heralded entanglement between solid-state qubits separated by 3 meters," *arXiv:1212.6136*, Dec. 2012.

[130] J. R. Schaibley, A. P. Burgers, G. A. McCracken, L.-M. Duan, P. R. Berman, D. G. Steel, A. S. Bracker, D. Gammon, and L. J. Sham, "Demonstration of quantum entanglement between a single electron spin confined to an InAs quantum dot and a photon," *arXiv:1210.5555*, Oct. 2012.

[131] M. Wallquist, K. Hammerer, P. Rabl, M. Lukin, and P. Zoller, "Hybrid quantum devices and quantum engineering," *Physica Scripta*, vol. 2009, p. 014001, Dec. 2009.

[132] S. Ramelow, A. Fedrizzi, A. Poppe, N. K. Langford, and A. Zeilinger, "Polarization-entanglement-conserving frequency conversion of photons," *Physical Review A*, vol. 85, p. 013845, Jan. 2012.

[133] P. Tamarat, T. Gaebel, J. R. Rabeau, M. Khan, A. D. Greentree, H. Wilson, L. C. L. Hollenberg, S. Prawer, P. Hemmer, F. Jelezko, and J. Wrachtrup, "Stark shift control of single optical centers in diamond," *Physical Review Letters*, vol. 97, no. 8, p. 083002, 2006.

[134] C. Cabrillo, J. I. Cirac, P. García-Fernández, and P. Zoller, "Creation of entangled states of distant atoms by interference," *Physical Review A*, vol. 59, pp. 1025–1033, Feb. 1999.

[135] S. Olmschenk, D. N. Matsukevich, P. Maunz, D. Hayes, L.-M. Duan, and C. Monroe, "Quantum teleportation between distant matter qubits," *Science*, vol. 323, pp. 486–489, Jan. 2009.

[136] L.-M. Duan and H. Kimble, "Efficient engineering of multiatom entanglement through single-photon detections," *Physical Review Letters*, vol. 90, June 2003.

[137] X. Xu, B. Sun, P. R. Berman, D. G. Steel, A. S. Bracker, D. Gammon, and L. J. Sham, "Coherent population trapping of an electron spin in a single negatively charged quantum dot," *Nature Physics*, vol. 4, pp. 692–695, Aug. 2008.

[138] C. E. Wieman, D. E. Pritchard, and D. J. Wineland, "Atom cooling, trapping, and quantum manipulation," *Reviews of Modern Physics*, vol. 71, pp. S253–S262, Mar. 1999.

[139] J. I. Cirac and P. Zoller, "Quantum computations with cold trapped ions," *Physical Review Letters*, vol. 74, pp. 4091–4094, May 1995.

[140] H. Häffner, C. Roos, and R. Blatt, "Quantum computing with trapped ions," *Physics Reports*, vol. 469, pp. 155–203, Dec. 2008.

[141] R. Blatt and D. Wineland, "Entangled states of trapped atomic ions," *Nature*, vol. 453, pp. 1008–1015, June 2008.

[142] D. J. Berkeland, J. D. Miller, J. C. Bergquist, W. M. Itano, and D. J. Wineland, "Laser-cooled mercury ion frequency standard," *Physical Review Letters*, vol. 80, pp. 2089–2092, Mar. 1998.

[143] D. Porras and J. I. Cirac, "Effective quantum spin systems with trapped ions," *Physical Review Letters*, vol. 92, no. 20, p. 207901, 2004.

[144] A. Friedenauer, H. Schmitz, J. T. Glueckert, D. Porras, and T. Schaetz, "Simulating a quantum magnet with trapped ions," *Nat Phys*, vol. 4, no. 10, pp. 757–761, 2008.

[145] A. Mortensen, E. Nielsen, T. Matthey, and M. Drewsen, "Observation of three-dimensional long-range order in small ion coulomb crystals in an rf trap," *Physical Review Letters*, vol. 96, p. 103001, Mar. 2006.

[146] N. Kjærgaard and M. Drewsen, "Observation of a structural transition for coulomb crystals in a linear paul trap," *Physical Review Letters*, vol. 91, p. 095002, Aug. 2003.

[147] G. Birkl, S. Kassner, and H. Walther, "Multiple-shell structures of laser-cooled 24Mg+ ions in a quadrupole storage ring," *Nature*, vol. 357, pp. 310–313, May 1992.

[148] I. Waki, S. Kassner, G. Birkl, and H. Walther, "Observation of ordered structures of laser-cooled ions in a quadrupole storage ring," *Physical Review Letters*, vol. 68, pp. 2007–2010, Mar. 1992.

[149] D. G. Enzer, M. M. Schauer, J. J. Gomez, M. S. Gulley, M. H. Holzscheiter, P. G. Kwiat, S. K. Lamoreaux, C. G. Peterson, V. D. Sandberg, D. Tupa, A. G. White, R. J. Hughes, and D. F. V. James, "Observation of power-law scaling for phase transitions in linear trapped ion crystals," *Physical Review Letters*, vol. 85, pp. 2466–2469, Sept. 2000.

[150] D. H. E. Dubin, "Theory of structural phase transitions in a trapped coulomb crystal," *Physical Review Letters*, vol. 71, pp. 2753–2756, Oct. 1993.

[151] J. P. Schiffer, "Phase transitions in anisotropically confined ionic crystals," *Physical Review Letters*, vol. 70, pp. 818–821, Feb. 1993.

[152] G. Morigi and S. Fishman, "Dynamics of an ion chain in a harmonic potential," *Physical Review E*, vol. 70, Dec. 2004.

[153] S. Fishman, G. De Chiara, T. Calarco, and G. Morigi, "Structural phase transitions in low-dimensional ion crystals," *Physical Review B*, vol. 77, p. 064111, Feb. 2008.

[154] A. Retzker, R. Thompson, D. Segal, and M. Plenio, "Double well potentials and quantum phase transitions in ion traps," *Physical Review Letters*, vol. 101, Dec. 2008.

[155] G. Piacente, I. V. Schweigert, J. J. Betouras, and F. M. Peeters, "Generic properties of a quasi-one-dimensional classical wigner crystal," *Physical Review B*, vol. 69, p. 045324, Jan. 2004.

[156] C. F. Roos, T. Monz, K. Kim, M. Riebe, H. Häffner, D. F. V. James, and R. Blatt, "Nonlinear coupling of continuous variables at the single quantum level," *Physical Review A*, vol. 77, p. 040302, Apr. 2008.

[157] H. Kleinert, *Path integrals in quantum mechanics, statistics, polymer physics, and financial markets*. New Jersey: World Scientific, 4th ed., 2006.

[158] F. Strocchi, *Symmetry breaking*. Berlin; New York: Springer, 2008.

[159] A. Shapere and F. Wilczek, "Classical time crystals," *Physical Review Letters*, vol. 109, p. 160402, Oct. 2012.

[160] N. Byers and C. N. Yang, "Theoretical considerations concerning quantized magnetic flux in superconducting cylinders," *Physical Review Letters*, vol. 7, pp. 46–49, July 1961.

[161] J.-X. Zhu and H. T. Quan, "Magnetic flux periodicity in a hollow d-wave superconducting cylinder," *Physical Review B*, vol. 81, p. 054521, Feb. 2010.

[162] A. C. Bleszynski-Jayich, W. E. Shanks, B. Peaudecerf, E. Ginossar, F. Von Oppen, L. Glazman, and J. G. E. Harris, "Persistent currents in normal metal rings," *Science*, vol. 326, pp. 272–275, Oct. 2009.

[163] G. Burmeister and K. Maschke, "Influence of the electron-electron interaction on electronic spectra and persistent currents in one-dimensional loops," *Physical Review B*, vol. 65, Apr. 2002.

[164] D. Levine and P. J. Steinhardt, "Quasicrystals. i. definition and structure," *Physical Review B*, vol. 34, pp. 596–616, July 1986.

[165] C. Langer, R. Ozeri, J. D. Jost, J. Chiaverini, B. DeMarco, A. Ben-Kish, R. B. Blakestad, J. Britton, D. B. Hume, W. M. Itano, D. Leibfried, R. Reichle, T. Rosenband, T. Schaetz, P. O. Schmidt, and D. J. Wineland, "Long-lived qubit memory using atomic ions," *Physical Review Letters*, vol. 95, p. 060502, Aug. 2005.

[166] D. Cruz, J. P. Chang, M. Fico, A. J. Guymon, D. E. Austin, and M. G. Blain, "Design, microfabrication, and analysis of micrometer-sized cylindrical ion trap arrays," *Review of Scientific Instruments*, vol. 78, no. 1, p. 015107, 2007.

[167] D. Segal and M. Shapiro, "Nanoscale paul trapping of a single electron," *Nano Letters*, vol. 6, pp. 1622–1626, Aug. 2006.

[168] C. Monroe, D. M. Meekhof, B. E. King, S. R. Jefferts, W. M. Itano, D. J. Wineland, and P. Gould, "Resolved-sideband raman cooling of a bound atom to the 3D zero-point energy," *Physical Review Letters*, vol. 75, pp. 4011–4014, Nov. 1995.

[169] C. Zipkes, S. Palzer, C. Sias, and M. K|[ouml]|hl, "A trapped single ion inside a bose-einstein condensate," *Nature*, vol. 464, p. 388, Mar. 2010.

[170] A. E. Leanhardt, T. A. Pasquini, M. Saba, A. Schirotzek, Y. Shin, D. Kielpinski, D. E. Pritchard, and W. Ketterle, "Cooling bose-einstein condensates below 500 picokelvin," *Science*, vol. 301, pp. 1513–1515, Sept. 2003.

[171] S. T. Bramwell and M. J. P. Gingras, "Spin ice state in frustrated magnetic pyrochlore materials," *Science*, vol. 294, pp. 1495–1501, Nov. 2001.

[172] R. Singh, "Spinning on ice," *Physics*, vol. 4, p. 77, Oct. 2011.

[173] K. Binder and A. P. Young, "Spin glasses: Experimental facts, theoretical concepts, and open questions," *Reviews of Modern Physics*, vol. 58, no. 4, pp. 801–976, 1986.

[174] S. Sachdev, *Quantum phase transitions*. Cambridge ;;New York: Cambridge University Press, 2nd ed., 2011.

[175] Anderson P.W., "Resonating valence bonds: A new kind of insulator?," *Materials Research Bulletin*, vol. 8, no. 2, pp. 153–160, 1973.

[176] L. Balents, "Spin liquids in frustrated magnets," *Nature*, vol. 464, no. 7286, pp. 199–208, 2010.

[177] P. W. Anderson, G. Baskaran, Z. Zou, and T. Hsu, "Resonating–valence-bond theory of phase transitions and superconductivity in la_{2}CuO_{4}-based compounds," *Physical Review Letters*, vol. 58, no. 26, pp. 2790–2793, 1987.

[178] K. Kim, S. Korenblit, R. Islam, E. E. Edwards, M.-S. Chang, C. Noh, H. Carmichael, G.-D. Lin, L.-M. Duan, C. C. Joseph Wang, J. K. Freericks, and C. Monroe, "Quantum simulation of the transverse ising model with trapped ions," *New Journal of Physics*, vol. 13, p. 105003, Oct. 2011.

[179] J. Simon, W. S. Bakr, R. Ma, M. E. Tai, P. M. Preiss, and M. Greiner, "Quantum simulation of antiferromagnetic spin chains in an optical lattice," *Nature*, vol. 472, no. 7343, pp. 307–312, 2011.

[180] F. D. M. Haldane, "Exact jastrow-gutzwiller resonating-valence-bond ground state of the spin-(1/2 antiferromagnetic heisenberg chain with 1/r^{2} exchange," *Physical Review Letters*, vol. 60, pp. 635–638, Feb. 1988.

[181] B. S. Shastry, "Exact solution of an s=1/2 heisenberg antiferromagnetic chain with long-ranged interactions," *Physical Review Letters*, vol. 60, pp. 639–642, Feb. 1988.

[182] F. D. M. Haldane, ""Spinon gas" description of the s=1/2 heisenberg chain with inverse-square exchange: Exact spectrum and thermodynamics," *Physical Review Letters*, vol. 66, no. 11, pp. 1529–1532, 1991.

[183] F. D. M. Haldane, ""Fractional statistics" in arbitrary dimensions: A generalization of the pauli principle," *Physical Review Letters*, vol. 67, no. 8, pp. 937–940, 1991.

[184] B. A. Bernevig, D. Giuliano, and R. B. Laughlin, "Coordinate representation of the two-spinon wave function and spinon interaction in the haldane-shastry model," *Physical Review B*, vol. 64, no. 2, p. 024425, 2001.

[185] F. D. M. Haldane, "Fractional quantization of the hall effect: A hierarchy of incompressible quantum fluid states," *Physical Review Letters*, vol. 51, no. 7, p. 605, 1983.

[186] M. C. Gutzwiller, "Effect of correlation on the ferromagnetism of transition metals," *Physical Review Letters*, vol. 10, no. 5, pp. 159–162, 1963.

[187] F. Gebhard and D. Vollhardt, "Correlation functions for hubbard-type models: The exact results for the gutzwiller wave function in one dimension," *Physical Review Letters*, vol. 59, no. 13, pp. 1472–1475, 1987.

[188] K. Okada, K. Yasuda, T. Takayanagi, M. Wada, H. A. Schuessler, and S. Ohtani, "Crystallization of ca^{+} ions in a linear rf octupole ion trap," *Physical Review A*, vol. 75, no. 3, p. 033409, 2007.

[189] K. Okada, T. Takayanagi, M. Wada, S. Ohtani, and H. A. Schuessler, "Observation of ion coulomb crystals in a cryogenic linear octupole rf ion trap," *Physical Review A*, vol. 80, p. 043405, Oct. 2009.

[190] K. Kim, M.-S. Chang, R. Islam, S. Korenblit, L.-M. Duan, and C. Monroe, "Entanglement and tunable spin-spin couplings between trapped ions using multiple transverse modes," *Physical Review Letters*, vol. 103, no. 12, p. 120502, 2009.

[191] F. D. M. Haldane, "Model for a quantum hall effect without landau levels: Condensed-matter realization of the "Parity anomaly"," *Physical Review Letters*, vol. 61, no. 18, p. 2015, 1988.

[192] J. I. Cirac and G. Sierra, "Infinite matrix product states, conformal field theory, and the haldane-shastry model," *Physical Review B*, vol. 81, no. 10, p. 104431, 2010.

[193] A. Polkovnikov, K. Sengupta, A. Silva, and M. Vengalattore, "Colloquium: Nonequilibrium dynamics of closed interacting quantum systems," *Reviews of Modern Physics*, vol. 83, no. 3, p. 863, 2011.

[194] M. A. Cazalilla and M. Rigol, "Focus on dynamics and thermalization in isolated quantum many-body systems," *New Journal of Physics*, vol. 12, p. 055006, May 2010.

[195] J. M. Deutsch, "Quantum statistical mechanics in a closed system," *Physical Review A*, vol. 43, p. 2046, Feb. 1991.

[196] M. Srednicki, "Chaos and quantum thermalization," *Physical Review E*, vol. 50, no. 2, p. 888, 1994.

[197] M. Rigol, V. Dunjko, and M. Olshanii, "Thermalization and its mechanism for generic isolated quantum systems," *Nature*, vol. 452, no. 7189, pp. 854–858, 2008.

[198] M. Rigol, V. Dunjko, V. Yurovsky, and M. Olshanii, "Relaxation in a completely integrable many-body quantum system: An ab initio study of the dynamics of the highly excited states of 1D lattice hard-core bosons," *Physical Review Letters*, vol. 98, no. 5, p. 050405, 2007.

[199] P. Reimann, "Foundation of statistical mechanics under experimentally realistic conditions," *Physical Review Letters*, vol. 101, no. 19, p. 190403, 2008.

[200] L. Masanes, A. J. Roncaglia, and A. Acín, "Complexity of energy eigenstates as a mechanism for equilibration," *Physical Review E*, vol. 87, p. 032137, Mar. 2013.

[201] F. G. S. L. Brandão, P. Ćwikliński, M. Horodecki, P. Horodecki, J. K. Korbicz, and M. Mozrzymas, "Convergence to equilibrium under a random hamiltonian," *Physical Review E*, vol. 86, no. 3, p. 031101, 2012.

[202] P. Reimann and M. Kastner, "Equilibration of isolated macroscopic quantum systems," *New Journal of Physics*, vol. 14, p. 043020, Apr. 2012.

[203] Z.-X. Gong and L.-M. Duan, "Comment on "Foundation of statistical mechanics under experimentally realistic conditions"," *arXiv:1109.4696*, Sept. 2011.

[204] T. Kinoshita, T. Wenger, and D. S. Weiss, "A quantum newton's cradle," *Nature*, vol. 440, pp. 900–903, Apr. 2006.

[205] S. Trotzky, Y.-A. Chen, A. Flesch, I. P. McCulloch, U. Schollwöck, J. Eisert, and I. Bloch, "Probing the relaxation towards equilibrium in an isolated strongly correlated one-dimensional bosegas," *Nature Physics*, vol. 8, pp. 325–330, Feb. 2012.

[206] M. Gring, M. Kuhnert, T. Langen, T. Kitagawa, B. Rauer, M. Schreitl, I. Mazets, D. A. Smith, E. Demler, and J. Schmiedmayer, "Relaxation and prethermalization in an isolated quantum system," *Science*, vol. 337, pp. 1318–1322, Sept. 2012.

[207] J. Berges, S. Borsányi, and C. Wetterich, "Prethermalization," *Physical Review Letters*, vol. 93, no. 14, p. 142002, 2004.

[208] M. Kollar, F. A. Wolf, and M. Eckstein, "Generalized gibbs ensemble prediction of prethermalization plateaus and their relation to nonthermal steady states in integrable systems," *Physical Review B*, vol. 84, no. 5, p. 054304, 2011.

[209] R. Barnett, A. Polkovnikov, and M. Vengalattore, "Prethermalization in quenched spinor condensates," *Physical Review A*, vol. 84, no. 2, p. 023606, 2011.

[210] M. v. d. Worm, B. C. Sawyer, J. J. Bollinger, and Michael Kastner, "Relaxation timescales and decay of correlations in a long-range interacting quantum simulator," *arXiv:1209.3697*, Sept. 2012.

[211] T. Kitagawa, A. Imambekov, J. Schmiedmayer, and E. Demler, "The dynamics and prethermalization of one-dimensional quantum systems probed through the full distributions of quantum noise," *New Journal of Physics*, vol. 13, p. 073018, July 2011.

[212] M. Heyl, A. Polkovnikov, and S. Kehrein, "Dynamical quantum phase transitions in the transverse field ising model," *arXiv:1206.2505*, June 2012.

[213] G. G. Emch, "NonMarkovian model for the approach to equilibrium," *Journal of Mathematical Physics*, vol. 7, pp. 1198–1206, July 1966.

[214] C. Radin, "Approach to equilibrium in a simple model," *Journal of Mathematical Physics*, vol. 11, pp. 2945–2955, Oct. 1970.

[215] M. Kastner, "Diverging equilibration times in long-range quantum spin models," *Physical Review Letters*, vol. 106, p. 130601, Mar. 2011.

[216] A. Mitra, "Time evolution and dynamical phase transitions at a critical time in a system of one-dimensional bosons after a quantum quench," *Physical Review Letters*, vol. 109, Dec. 2012.

[217] M. Foss-Feig, K. R. A. Hazzard, J. J. Bollinger, and A. M. Rey, "Non-equilibrium dynamics of ising models with decoherence: an exact solution," *arXiv:1209.5795*, Sept. 2012.

[218] M. Eckstein, M. Kollar, and P. Werner, "Thermalization after an interaction quench in the hubbard model," *Physical Review Letters*, vol. 103, no. 5, p. 056403, 2009.

[219] C. Albanese, M. Christandl, N. Datta, and A. Ekert, "Mirror inversion of quantum states in linear registers," *Physical Review Letters*, vol. 93, no. 23, p. 230502, 2004.

[220] G. Mazza and M. Fabrizio, "Dynamical quantum phase transitions and broken-symmetry edges in the many-body eigenvalue spectrum," *Physical Review B*, vol. 86, Nov. 2012.

[221] C. Monroe and J. Kim, "Scaling the ion trap quantum processor," *Science*, vol. 339, pp. 1164–1169, Mar. 2013.

[222] D. D. Awschalom, L. C. Bassett, A. S. Dzurak, E. L. Hu, and J. R. Petta, "Quantum spintronics: Engineering and manipulating atom-like spins in semiconductors," *Science*, vol. 339, pp. 1174–1179, Mar. 2013.

[223] M. H. Devoret and R. J. Schoelkopf, "Superconducting circuits for quantum information: An outlook," *Science*, vol. 339, pp. 1169–1174, Mar. 2013.

[224] R. J. Schoelkopf and S. M. Girvin, "Wiring up quantum systems," *Nature*, vol. 451, pp. 664–669, Feb. 2008.

[225] J. Q. You and F. Nori, "Superconducting circuits and quantum information," *Physics Today*, vol. 58, no. 11, pp. 42–47, 2005.

[226] R. Gerritsma, G. Kirchmair, F. Zahringer, E. Solano, R. Blatt, and C. F. Roos, "Quantum simulation of the dirac equation," *Nature*, vol. 463, no. 7277, pp. 68–71, 2010.

[227] Y.-J. Lin, K. Jimenez-Garcia, and I. B. Spielman, "Spin-orbit-coupled bose-einstein condensates," *Nature*, vol. 471, pp. 83–86, Mar. 2011.

[228] N. H. Lindner, G. Refael, and V. Galitski, "Floquet topological insulator in semiconductor quantum wells," *Nature Physics*, vol. 7, no. 6, pp. 490–495, 2011.

[229] J. T. Barreiro, M. Muller, P. Schindler, D. Nigg, T. Monz, M. Chwalla, M. Hennrich, C. F. Roos, P. Zoller, and R. Blatt, "An open-system quantum simulator with trapped ions," *Nature*, vol. 470, no. 7335, pp. 486–491, 2011.

[230] T. Schätz, U. Schramm, and D. Habs, "Crystalline ion beams," *Nature*, vol. 412, pp. 717–720, Aug. 2001.

[231] M. Madsen and C. Gorman, "Compact toroidal ion-trap design and optimization," *Physical Review A*, vol. 82, Oct. 2010.

[232] C. Champenois, M. Marciante, J. Pedregosa-Gutierrez, M. Houssin, M. Knoop, and M. Kajita, "Ion ring in a linear multipole trap for optical frequency metrology," *Physical Review A*, vol. 81, p. 043410, Apr. 2010.